

The Avatar Paradigm in Granular Materials

Thesis by
Reid Y. Kawamoto

In Partial Fulfillment of the Requirements for the
Degree of Doctor of Philosophy in
Applied Mechanics

The logo for the California Institute of Technology (Caltech), featuring the word "Caltech" in a bold, orange, sans-serif font.

CALIFORNIA INSTITUTE OF TECHNOLOGY
Pasadena, California

2018
Defended June 2, 2017

© 2018

Reid Y. Kawamoto

ORCID: 0000-0002-4936-5321

All rights reserved

ACKNOWLEDGEMENTS

Thank you to my advisor, Prof. José E. Andrade, for accepting me into the Computational Geomechanics group and providing me with the support I needed to be able to complete this PhD. You have guided me to become a better researcher, presenter, writer, graphic designer, and independent thinker. To the Computational Geomechanics group, thank you for always entertaining my thoughts and ideas and giving me help and advice. In particular, thank you to the (former) groupmates with whom I have collaborated, Dr. Ivan Vlahinic, Dr. Keng-Wit Lim, Dr. Utkarsh Mital, and Prof. Alex Jerves; with your support I have been able to do far more than I would have been able to by myself.

Thank you to the rest of my committee members, Prof. Domniki Asimaki, Prof. Kaushik Bhattacharya, and Prof. Nadia Lapusta.

To our collaborators at Université Grenoble Alpes, Dr. Edward Andò and Prof. Cino Viggiani, thank you for conducting and imaging all of the experiments featured in this thesis; without your work everything in this thesis would simply not have been possible.

Thank you to Prof. Takashi Matsushima and the Geotech Lab at the University of Tsukuba for hosting me during the summer of 2016; while my stay was short, I gained important knowledge and perspectives that helped me move forward with my research.

Thank you to those at Caltech who have helped make the last five years far less stressful than it could have been: staff, professors, classmates, teammates, and friends.

Finally, thank you to my parents for your unconditional support.

ABSTRACT

Granular materials are ubiquitous in both everyday life and various engineering and industrial applications, ranging from breakfast cereal to sand to rice to medical pills. However, despite the familiarity of granular materials, their behavior is complex and efforts to characterize them are currently broad research areas in physics and engineering. Research of granular materials, as is the case with the research of other engineering materials such as rocks and metals, is beset with two gaps: the gap between reconciling macroscopic behavior with microscale (particle-scale, in the case of granular materials) behavior, and the gap between reconciling experimental and computational results. In this dissertation, we bridge these gaps through the “avatar paradigm.” The avatar paradigm is a two-step process that numerically characterizes (from experimental images) and simulates the shapes and behavior of individual particles, which we call avatars. First, we validate that our avatars are indeed capable of faithfully capturing particle kinematics and interparticle contact, then apply the characterization process, level set imaging (LS-imaging), to two experimental specimens to compute particle kinematics and contact statistics. We then detail a computational method, the level set discrete element method (LS-DEM), that is able to simulate the behavior of avatars, and apply it (and LS-imaging) to two other experimental specimens, calibrating the model to one specimen and using the results to predict the behavior of the other, thus providing some reconciliation between experimental and computational results. Finally, we use the avatar process to characterize and simulate yet another experimental specimen, this time analyzing the results at length scales ranging from particle behavior to local behavior to macroscopic behavior, further validating the ability of the avatar paradigm to bridge experiments and computations and showing its power to reconcile different length scales.

PUBLISHED CONTENT AND CONTRIBUTIONS

The following published papers were adapted to form the content in chapters 2, 3, and 4 of this thesis, respectively.

1. Vlahinić, Ivan, Reid Kawamoto, Edward Andò, Gioacchino Viggiani, and José Andrade (2017). “From computed tomography to mechanics of granular materials via level set bridge”. In: *Acta Geotechnica* 12.1, pp. 85–95. doi: <https://doi.org/10.1007/s10035-013-0460-6>

The author gathered and processed the data for the content in the synthetic and ballotini subsections in Section 2.3 and participated in the writing of the manuscript.

2. Kawamoto, Reid, Edward Andò, Gioacchino Viggiani, and José E. Andrade. “Level set discrete element method for three-dimensional computations with triaxial case study”. In: *Journal of the Mechanics and Physics of Solids* 91, pp. 1–13. doi: <http://doi.org/10.1016/j.jmps.2016.02.021>

The author participated in the conception of the project, helped to develop LS-DEM and implemented it, carried out LS-imaging and the LS-DEM simulations, processed the data, and participated in the writing of the manuscript.

3. Kawamoto, Reid, Edward Andò, Gioacchino Viggiani, and José E. Andrade. “All you need is shape: predicting shear banding in sand with LS-DEM”. In: *Journal of the Mechanics and Physics of Solids* 111 (Supplement C), pp. 375–392. doi: <https://doi.org/10.1016/j.jmps.2017.10.003>

The author participated in the conception of the project, implemented the boundary condition improvements in LS-DEM, carried out LS-imaging and the LS-DEM simulations, processed the data, and participated in the writing of the manuscript.

TABLE OF CONTENTS

Acknowledgements	iii
Abstract	iv
Published Content and Contributions	v
Table of Contents	vi
List of Illustrations	vii
List of Tables	xii
Chapter I: Introduction	1
1.1 Objective	1
1.2 Background and overview	1
1.3 Thesis contents	9
Chapter II: From computed tomography to mechanics of granular materials via level set bridge	11
2.1 Review of previous studies	13
2.2 Algorithms for grain fabric and kinematics	15
2.3 Results	20
2.4 Conclusions	29
Chapter III: Level set discrete element method for three-dimensional compu- tations with triaxial case study	31
3.1 Level set discrete element method	32
3.2 Case study: Triaxial compression test	42
3.3 Discussion	46
3.4 Conclusion	49
Chapter IV: Analysis of shear banding of granular materials in triaxial com- pression using LS-DEM	51
4.1 The experiment: triaxial compression test and imaging of specimen	54
4.2 Bridging the experiment and computation: The avatar specimen with LS-Imaging	57
4.3 Computations: Modeling and simulation of avatar specimen	57
4.4 Validation of simulation	63
4.5 Shear band investigation	67
4.6 Conclusions and future outlook	76
4.7 Acknowledgements	77
Chapter V: Conclusions and future outlook	78
Bibliography	80

LIST OF ILLUSTRATIONS

<i>Number</i>	<i>Page</i>
1.1 Schematic and imposed stress states of the triaxial compression test and typical test results. The platens are grey and the granular specimen, enclosed by a membrane, is brown.	2
1.2 Left, a triaxial compression test apparatus with X-ray generator and detector. Right, a 2-D image slice of a 3-D XRCT image of a specimen of Hostun sand. The specimen is 2.5cm tall and 1.2cm in diameter.	5
1.3 Left, contact detection in DEM. Right, a small DEM assembly of 25 discs.	6
1.4 The level set imaging process. Note that this illustration is a 2-D slice of a 3-D operation. All LS-imaging in this thesis is performed in 3-D.	8
2.1 Overview of proposed method versus current methods. The bridge is a total solution for characterization, while current methods require separate algorithms. See (Vlahinic et al. 2013) for more on extracting shape from 3-D XRCT images.	15
2.2 An image of a convex-convex synthetic contact with random noise ($\sigma = 0.01$) of two synthetic grains of diameter 30 voxels, typical of images of synthetic contacts in this section. Note that the image shown is a 2-D slice of a 3-D image.	21
2.3 2-D schematic of the three different contact types, with magnified insets. Below, histograms of contact orientation errors for 1000 trials each of two contacting grains in random orientations, for varying levels of white noise σ (signal to noise ratio) and grain resolution D (voxels per grain diameter). Note that while the schematic above is 2-D, all tests and reported results are based on 3-D geometries.	22
2.4 An image of a synthetic, randomly oriented grain with random noise ($\sigma = 0.01$) and a diameter of 30 voxels used in the test of kinematic accuracy, typical of images of synthetic grains used to track kinematics in this section. Note that the image shown is a 2-D slice of a 3-D image.	23

- 2.5 Histograms of rotation and translation errors for 1000 trials each of a single grain translating and rotating from an initial position and rotation to a random position and rotation, for varying levels of noise σ and grain diameter D . Note that while the schematic above is in 2-D, all tests performed are 3-D. 24
- 2.6 3-D XRCT images of ballotini specimen at the onset of loading and post-localization (top), along with the macroscopic stress-strain. Contact statistics are reported for a region inside and two regions outside of the shear band. Individual grains belonging to these regions are shown as level set contours in top middle of the figure. The overlay over 3-D XRCT images is colored by displacement magnitude of individual grains, an indicator of the shear band location. Contact statistics (bottom histograms) show the relative frequency of contacts occurring in a given direction, indicated by the distance of a given triangle from the origin. We see a significant loss of contacts in the horizontal directions (minimum principal stress; compression positive) and significant gain in the contacts in the maximum principal stress direction, as reported in multiples of mean contacts per grain in each region (e.g., 1.3 corresponds to 130% of the mean contact frequency in a given direction). 25
- 2.7 3-D XRCT images of Caicos ooid specimen at the onset of loading (left) and post-localization (right), with the analyzed subvolume encompassed by a blue square. In the middle, statistical histogram of contacts is shown for loads steps 1 and 16. Description of the axis and scale is the same as for glass ballotini. At the bottom, incremental translations (in voxel units) and rotations (axis and magnitude) are shown for the 15 grains that remained inside the subregion during all 16 loading stages. Note the grain rotations appear entirely random, seemingly unaffected by shear band orientation or loading direction. The kinematics of one of the grains during all loading stages (shown in blue) exemplifies typical temporal resolution available in a 3-D XRCT experiment. 28

3.1	Illustration of this chapter’s contents, LS-DEM and its validation (bold-italicized), which are the links that allow us to fully connect the four areas between experiments and computations. Note that the experimental images are 2D slices of a 3D XRCT image, and the virtual specimen is 3D.	32
3.2	Illustration of a level set function. (a) Grain particle surface. (b) Contour lines representing signed distance from surface. (c) Superimposition on grid. (d) Discretized level set function. (e) Level set function with interpolation between grid points. (f) Reconstruction of original grain surface via interpolation. Note that the level set functions shown here are 2D for illustrative purposes only.	34
3.3	Schematic of point \mathbf{p} with surrounding grid points \mathbf{p}_{abc}	35
3.4	Example of boundary node discretization with nodes in white seeded on the grain surface. This is shown in 2D for illustrative purposes only.	38
3.5	Illustration of two contacting grains.	39
3.6	Stress-strain and volume-strain results of experiments. Note: experimental volume-strain data for the looser specimen was stopped at 18%.	43
3.7	Left: 3D rendering of XRCT image of uncompressed looser specimen. Center: Virtual level set function representation of looser specimen. Right: Virtual specimen after triaxial compression.	44
3.8	Stress-strain and volume-strain relations for LS-DEM simulations on looser specimen. The values $k_n = 3 \times 10^6$ and $\mu = 0.65$ are chosen as best-fit parameters.	45
3.9	Left: 3D rendering of XRCT image of uncompressed denser specimen. Center: Virtual level set function representation of denser specimen. Right: Virtual specimen after triaxial compression.	47
3.10	Stress-strain and volume-strain relations for LS-DEM simulations on looser (left) and denser (right) specimens with $k_n = 3 \times 10^6$ and $\mu = 0.65$	48
4.1	3-D XRCT image slice of the experimental specimen prior to triaxial compression and the specimen’s particle size distribution.	55

4.2	Stress-strain responses from the experiment. Positive values of volumetric strain indicate dilation. The stress relaxation in the stress-strain response is because axial loading is stopped during the imaging process. It is observed that, during imaging, no granular rearrangement takes place, which implies that stopping axial loading for imaging has a negligible impact on experimental results.	56
4.3	Avatar conversion process for a single avatar. The filtered image is both segmented and used to find particle edges, which are then fed into the level set imaging algorithm, which outputs an avatar. Note that these operations are performed in three dimensions; a slice is shown here for clarity.	57
4.4	Contact between two particles in LS-DEM. Particles shown here are 2D for simplicity; however, 3D particles are used in this study. Penetration depths are exaggerated for clarity.	59
4.5	Behavior of the platen. The platen does not slip on the loading ram, so it is limited to movement in the vertical direction and rotation about the ram tip.	60
4.6	Triangulation of three membrane spheres. (a) Neighboring spheres are connected by normal and shear springs. (b) Pressure is applied in the direction of the inward normal to each face.	61
4.7	Membrane (a) under isotropic stress and (b) at the end of triaxial loading.	62
4.8	Avatar specimen (a) under isotropic stress and (b) at the end of triaxial loading.	63
4.9	Macroscopic stress-strain responses from the experiment and LS-DEM simulation.	64
4.10	Experimental and simulation incremental local deviatoric strain between (a) 0.0 and 0.6%, (b) 3.9 and 5.1%, (c) 8.6 and 10.0%, and (d) 13.3 and 14.8% axial strain.	66
4.11	Experimental and LS-DEM incremental particle rotations between (a) 0.0 and 0.6%, (b) 3.9 and 5.1%, (c) 8.6 and 10.0%, and (d) 13.3 and 14.8% axial strain.	67
4.12	(a) Shear band and its normal \hat{n} in three-dimensional space, where z is the direction of loading, normal to the x - y plane. (b) The shear band inclination angle θ is measured with respect to the x - y plane. (c) The shear band orientation angle ϕ is measured in the x - y plane.	68

4.13	Simulation results (increment between 14 and 15%). Particles in red are those with (a) incremental rotations or (b) incremental local deviatoric strains larger than two standard deviations more than the mean, and corresponding best-fit planes.	69
4.14	Shear band inclination computed from best-fit planes computed from particles with large incremental rotations and large incremental deviatoric strains, inclination predicted by Mohr-Coulomb and Roscoe theories, and the converged value of the inclination angle from experimental data.	70
4.15	Shear band orientation angle computed from best-fit plane of large incremental local strains and incremental platen displacements. . . .	71
4.16	(a-b) Plots of mean incremental local deviatoric strain and mean incremental rotation between 13.3 and 14.8% axial strain versus distance from the center planes of shear bands in the experiment and simulation (which do not necessarily have the same location). The gray stripes represent a distance of $10D_{50}$, or 3.4mm, the thickness of the shear band. (c-d) Histograms of incremental local deviatoric strain and incremental rotation in the shear band (the gray stripes in a-b) during the same axial strain increment.	72
4.17	Interparticle forces in a shear band-aligned slice 1.4mm thick through the center of the specimen at (a) 0%, (b) 5%, (c) 10%, and (d) 15% axial strain. Thicker, longer lines represent larger interparticle forces.	74
4.18	Spherical histograms of interparticle forces at (a) 0%, (b) 5%, (c) 10%, and (d) 15% axial strain, inside and outside the shear band. The distributions at 0% axial strain are computed using the shear band location at peak stress since the shear band does not yet exist at 0% axial strain.	74
4.19	Inclination of the direction of the largest principal stress σ_1 , both outside and inside the shear band. The grayed-out sections of the lines are computed using the shear band location at peak stress since the shear band does not exist prior to that. Inset: 3-D view of the direction of σ_1 outside and inside the shear band at the end of loading. The gray line is vertical (90°).	75

LIST OF TABLES

<i>Number</i>		<i>Page</i>
2.1	Summary of experiments and statistical inferences performed as part of this study.	20
4.1	Values of parameters used in simulation of platen.	60
4.2	Values of parameters used in simulation of membrane.	61
4.3	Values of parameters used in simulation of particles.	63

Chapter 1

INTRODUCTION

1.1 Objective

The objective of this thesis is to present a complete platform for the characterization and simulation of granular materials at the particle scale—the “avatar paradigm,” named for its ability to numerically model the shapes and behavior of individual particles, which are called avatars—and to apply it to laboratory-scale systems of real granular materials. The avatar paradigm addresses two themes of connection central to this thesis: 1) the connection between experimental and computational results, and 2) the connection between the discrete and continuum scales. Through making these connections, the avatar paradigm has the potential to elevate our understanding of granular materials to new levels.

1.2 Background and overview

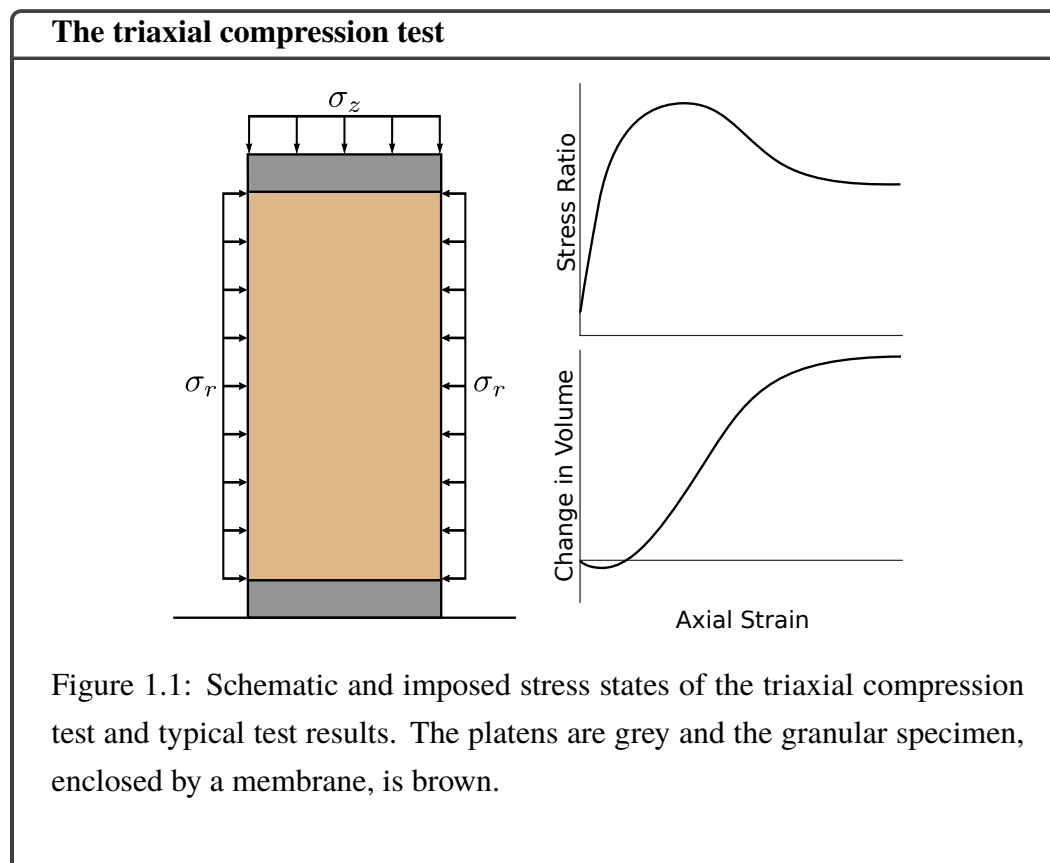
Granular materials are ubiquitous in both everyday life and various engineering and industrial applications, ranging from breakfast cereal to sand to rice to medical pills. However, despite the familiarity of granular materials, their behavior is complex and efforts to characterize them are currently broad research areas in physics and engineering. Granular materials research, as is the case with the research of other engineering materials such as rocks and metals, is beset with two gaps: the gap between reconciling macroscopic, or continuum-scale behavior with microscale (particle-scale, in the case of granular materials) behavior, and the gap between reconciling experimental and computational results. The gaps will be referred to as the multiscale and accuracy gaps, respectively.

The continuum and particle scales

Granular materials research has long existed at the continuum scale, where a granular material, despite consisting of discrete particles that interact with each other and voids between the particles, is viewed as an aggregate—a continuous chunk of material with no distinction between individual particles or between particles and void regions. Generally, research in the continuum realm falls into modeling using theory and computations, and performing experiments. Oftentimes, models are developed based on and calibrated to experimental considerations.

The oldest and most basic continuum model is the Mohr-Coulomb yield criterion, which predicts failure (or lack thereof) as a function of only the largest and smallest principal stresses (Labuz and Zang 2012). Since then, continuum models have become increasingly complex, incorporating more parameters such as all three stress invariants (Matsuoka and Nakai 1974) and physical phenomena such as the ability to model liquefaction (Wobbes et al. 2017), the compactive and dilative tendencies of sand (Borja and Andrade 2006), and anisotropy (Taiebat and Dafalias 2008). These models work acceptably; however, because continuum models do not take into account the properties and behavior of individual particles, they fail in the commonplace scenario where strain is localized in regions so small that granular structure cannot be ignored—landslides, hourglass orifice flow, and jamming, for example. Furthermore, even though continuum models can account for and capture many physical phenomena, they do not explain why they happen, and the answers may be found at the particle scale.

In the experimental realm, the triaxial compression test has long been the workhorse laboratory test to determine properties of granular materials (Bishop and Henkel 1957), as illustrated in Figure 1.1.



The triaxial compression test is a 3-D laboratory test that is used to measure properties of granular materials (Bishop and Henkel 1957). An assembly of a granular material is confined by a cylindrical rubber membrane, usually twice as tall as it is wide. The ends of the membrane are affixed to porous platens that allow interstitial fluids to move in or out of the specimen under so-called “drained loading” conditions, of which all triaxial experiments and simulations in this thesis are. The membrane is then pressurized to a typically constant cell pressure σ_r while one of the platens is compressed axially at a varying pressure σ_z . Figure 1.1 illustrates the triaxial compression test and typical test results, which include the stress ratio σ_z/σ_r and the change in volume as a function of axial strain. All of the triaxial specimens in this thesis were approximately 2.5cm in height and 1.2cm in diameter.

Since the triaxial compression test only measures the macroscopic stress, strain, and volume of the specimen, it cannot directly probe the effects of particle-scale properties. For example, it cannot probe the effects of interparticle friction and particle shape on how strain localizes into shear bands in the specimen, which can have considerable impacts on macroscopic behavior.

Thus, in order to characterize the entire gamut of granular behavior and to bridge the multiscale gap, it is important that both computational and experimental methods can model behavior at the particle scale. At this scale, familiar continuum concepts like stress and strain can only be thought of as average quantities of collections of particles and are the result of interparticle forces and the motion of particles relative to each other. For example, plasticity, the non-reversible deformation of a material under load, in granular materials is due in part to the rearrangement of particles¹ (Davis and Selvadurai 2005). But rather than attempting to inject particle-scale behavior into a continuum framework in order to capture its effects, we choose to begin at the particle scale, modeling particles, their kinematics and particle-to-particle interactions—and build up from there to extract continuum quantities from the particle scale. Fortunately, recent advances in experimental technology and computational power have made this possible.

¹The other part, the fracturing of particles, is outside the scope of this thesis.

Experiments and computations at the particle scale

Since the 1970s, particle-scale research of granular materials has become much more prevalent. Of the research that exists in investigating granular materials at the particle scale, there are broadly two camps: one which seeks to characterize granular assemblies, through experiments and often with X-ray computed tomographic (XRCT) scans (Andò 2013; Desrues et al. 1996; Rechenmacher and Finno 2004), and one which seeks to simulate granular behavior, typically through the discrete element method (DEM) (Cundall and Strack 1979). However, unlike the relationship between the experimental and modeling camps at the continuum scale, there has been little integration and validation between the two particle-scale camps; attempts at bridging the experimental-computational divide have focused on simple particle shapes such as spheres (Cil and Alshibli 2014a) or limiting the scope of comparison (Katagiri, Matsushima, and Yamada 2010; Lee 2014). This leaves a conundrum: experimental methods, though well-equipped to characterize granular materials, lack predictive power, while computational methods, though by their nature are predictive, have difficulty predicting anything that resembles reality.

Research on how granular materials evolve at the particle scale in response to loading was instrumental in spurring further particle-scale research. Through a series of classic triaxial compression tests (Oda 1972), researchers compressed sands and “froze” the microstructure in place by injecting polyester resin into the interstitial voids. Once the resin hardened and the arrangement of particles was preserved, the specimens were sliced open and quantities such as the orientations of particles and interparticle contacts were manually measured under a microscope. It was found that there indeed were strong trends between the continuum mechanical properties of granular materials, such as the results of the triaxial compression test, and the physical and spatial properties of their constituent particles, both in and of themselves and with respect to each other. However, this so-called “destructive” method were extremely labor-intensive and, because a specimen had to be destroyed to be analyzed, could not analyze a specimen at different stages of loading. Experimental particle-scale analysis did not gain much traction until faster, less destructive methods such as XRCT were developed and popularized.

The importation of XRCT technology, often used in the medical industry to image internal organs and bones, into granular materials research greatly decreased the labor cost and the destructiveness of particle-scale experimental methods and is now the most popular technology in this realm.

XRCT imaging of granular materials

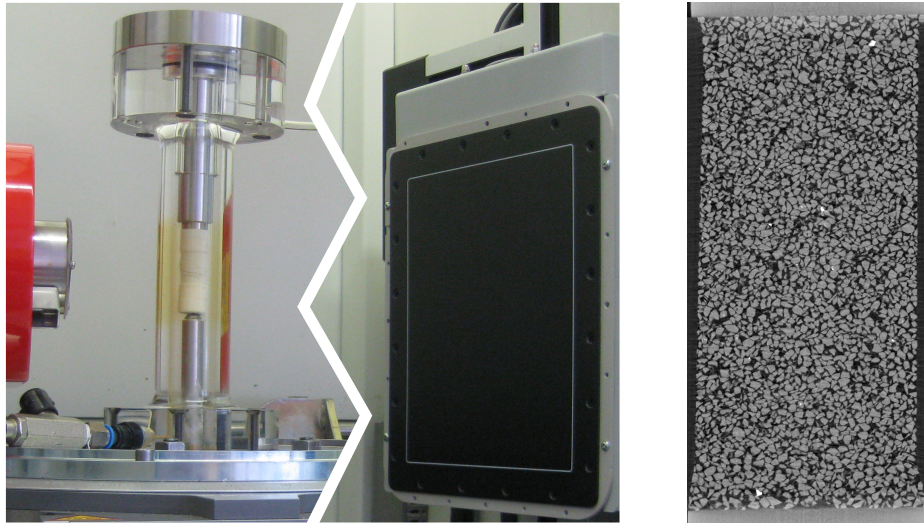


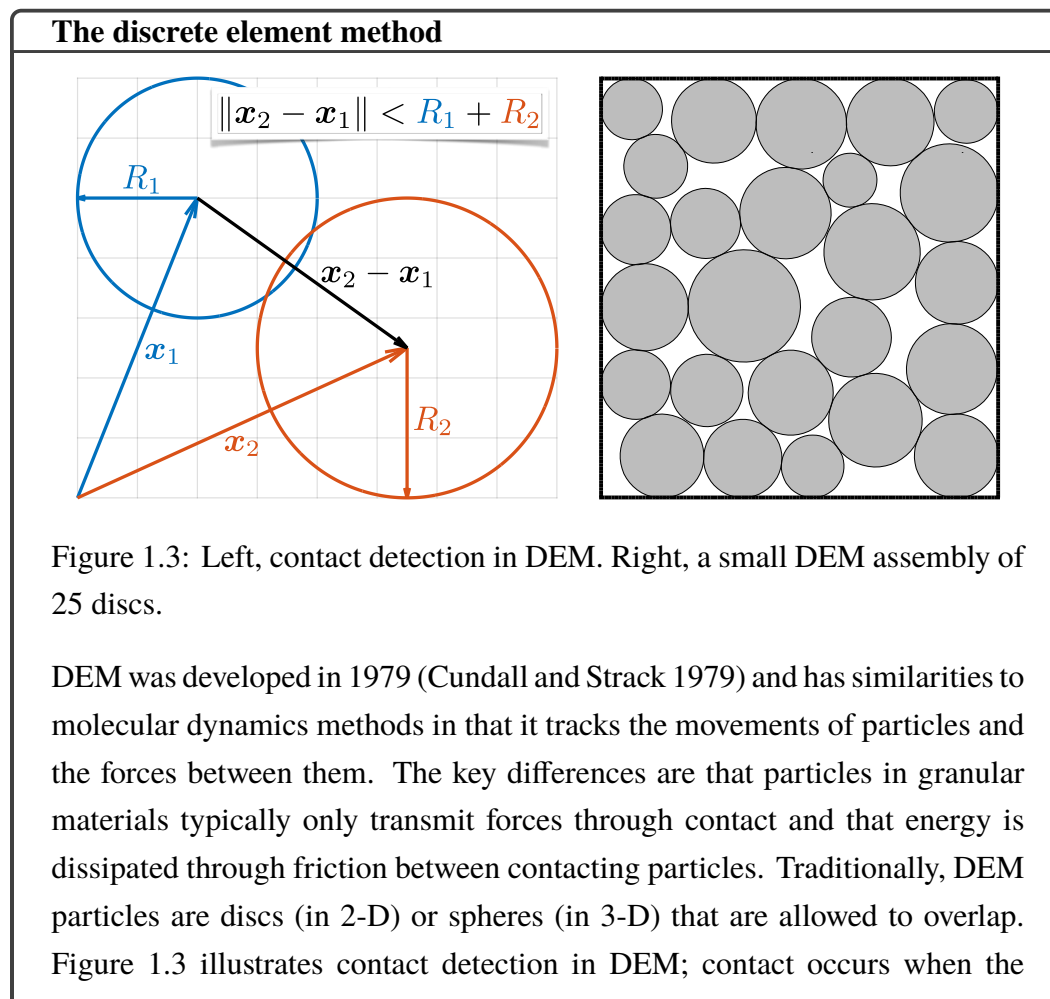
Figure 1.2: Left, a triaxial compression test apparatus with X-ray generator and detector. Right, a 2-D image slice of a 3-D XRCT image of a specimen of Hostun sand. The specimen is 2.5cm tall and 1.2cm in diameter.

XRCT is often used in the imaging of specimens of granular materials undergoing triaxial compression at various load stations throughout loading. At each imaging station, the specimen is rotated while X-ray projections are taken such that a large number, typically over a thousand, are obtained that equally span an entire rotation. The projections are then used to reconstruct a three-dimensional image via reconstruction techniques based on the Radon transform (Radon 1986) and backprojection (Hsieh 2003). The resulting three-dimensional image (“XRCT image”) must have a voxel resolution small enough to accurately characterize the geometry of each particle and the contacts between particles. A triaxial compression test setup augmented with X-ray capabilities and a 2-D slice of a 3-D XRCT image are shown in Figure 1.2.

Thanks to XRCT imaging, quantities such as particle kinematics and orientations, contact orientations, and porosity can be computed throughout the loading of an experimental specimen and have, for example, been used to probe the mechanics of shear localization (Andò et al. 2012b). However, interparticle forces—the origin of stress in granular materials—cannot be measured from XRCT images. And while developments have been made in inferring interparticle forces from photoelastic

discs (Majmudar and Behringer 2005) and strain in the particles themselves (Hurley et al. 2014), they have limitations. In the case of the former, particles are required to be made of photoelastic materials, while in the case of the latter, are still in infancy and are unable to characterize systems of a few hundred particles. Another drawback of research using XRCT imaging is that it is usually limited to the triaxial compression test, which, while certainly useful, can only probe a narrow range of stress paths and is not an entirely conclusive test for granular materials. Finally, as previously mentioned, experimental methods are not predictive. These three drawbacks, inability to measure forces, restriction to the triaxial compression test, and non-predictability, in part, have motivated particle-scale computational methods, which do not have such limitations.

The most popular particle-scale computational method is the discrete element method (DEM), which simulates the behavior of every individual particle in a granular system.

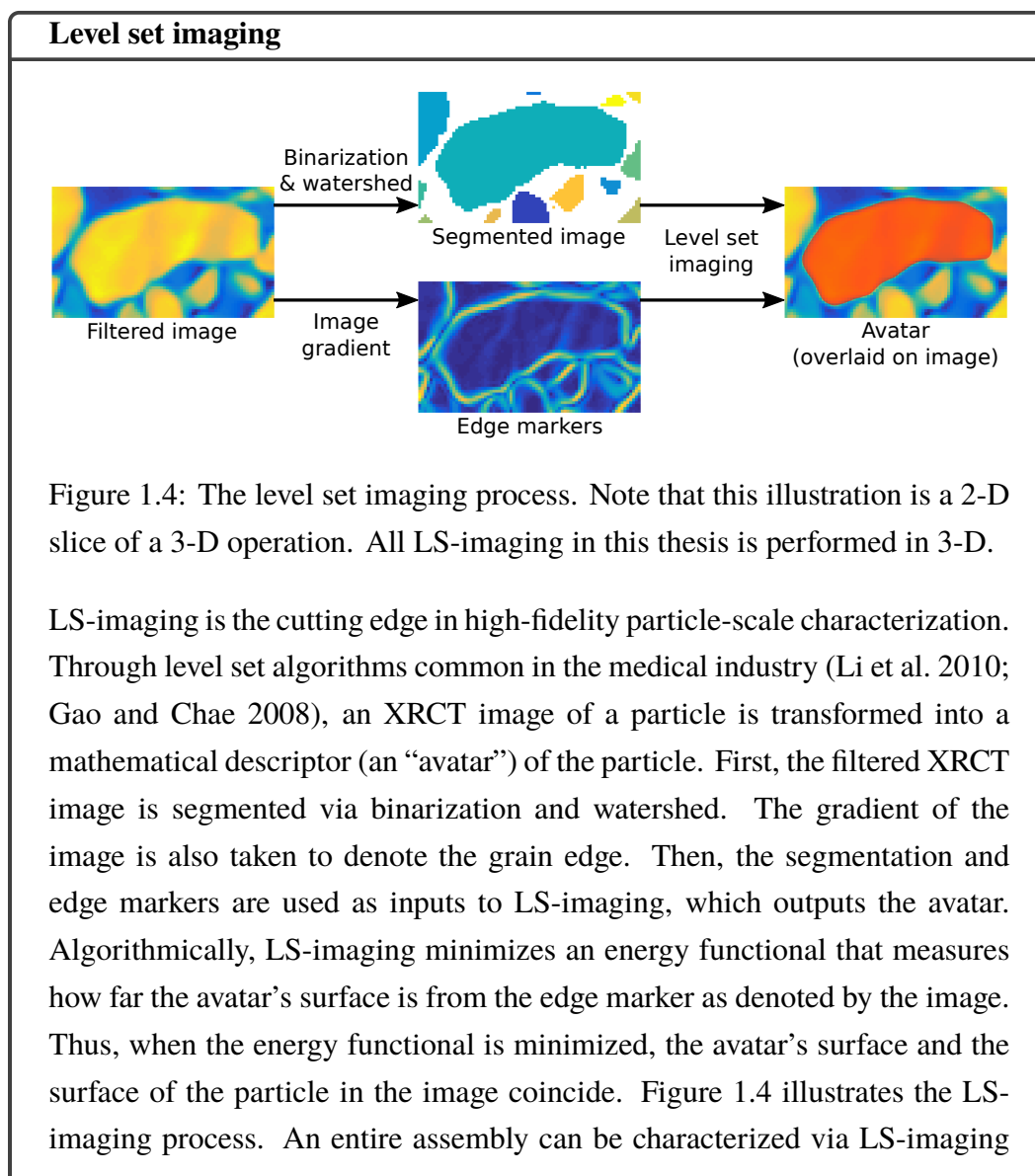


distance between two particles is less than the sum of their radii. Interparticle forces are computed between two contacting particles based on the amount of overlap, which produces a normal force, and the amount of relative shear motion, which produces a frictional force. After forces are computed for each contact and each particle, they are integrated in time to update kinematic quantities such as the positions and orientations of each particle, and the process is repeated for some number of timesteps.

Since the computation of interparticle forces is an inherent feature of DEM and the computational implementation of different boundary conditions and stress paths is relatively easy, DEM seems like an ideal tool to supplement and expand upon experiments. Unfortunately, because the particle shapes of DEM are limited to discs and spheres, DEM does a poor job of modeling reality, where particles come in many different shapes. This drawback is primarily responsible for the lack of integration and validation between the experimental and computational camps and has kept DEM from achieving prominence and respect in some research communities and industry, as particle shape plays an enormous role in determining the properties of granular assemblies (Cho, Dodds, and Santamarina 2006). Particle shape has typically been quantified in two parameters, sphericity and roundness, which describe the particle's volume deviation from a sphere and the sharpness of its corners, respectively. Efforts have been made to modify DEM to account for particle shape, often by clumping spheres (Garcia et al. 2009) or using polyhedra (Cundall 1988). While these geometric representations can represent the higher-order sphericity parameter well, they leave particles looking “clumpy” or “blocky” in the cases of clumping and polyhedra, respectively, and thus cannot adequately capture the lower-order roundness parameter and have had little success at reproducing experimental results without heavy numerical treatment or reducing the scope of the comparison. An attempt to improve the fidelity of particle representation by using B-splines as the geometric basis of particles (Andrade et al. 2012b) has been successful in replicating experimental results (Lim et al. 2016), but this method is computationally expensive in that it has only able to simulate a maximum of around one thousand particles. In order to be able to both simulate a reasonable amount of particles—even small triaxial specimens such as the ones in this thesis have between thousands and tens of thousands of particles—while being able to faithfully represent particle geometries, a new method was needed.

The avatar paradigm

The avatar paradigm is a complete experiment-to-simulation process that extracts mathematical descriptors (“avatars”) of particles from 3-D XRCT images of granular specimens through a method called level set imaging (LS-imaging) and simulates the kinematic and mechanical behavior of these particles through a method called the level set discrete element method (LS-DEM). While the idea for an experiment-to-simulation process has been in place for several years (Andrade et al. 2012a) and LS-imaging (Vlahinic et al. 2013) was developed before any of the content in this thesis, continued work on LS-imaging and the development of LS-DEM have allowed the avatar paradigm to fully come to fruition.



through repeating the process for every particle in the assembly.

Once LS-imaging has been performed to generate an avatar of every particle in an assembly, LS-DEM—described in detail in Chapter 3 and the crux of this thesis—is used to simulate the assembly computationally, where parameters such as interparticle friction are calibrated to match simulation results, at both the particle scale and the continuum scale, with those of the experiment. The resulting LS-DEM output is valuable because it provides crucial interparticle force and local stress information that the experiment does not, which can help to better explain granular phenomena, such as the behavior of shear bands. Finally, the avatars may be used again with LS-DEM but this time to simulate and explore other loading conditions and tests that may be difficult to perform experimentally, knowing that they have been calibrated and validated to some extent.

1.3 Thesis contents

Although the following chapters of this thesis are independent and can be read separately, they detail, in order, the development and continued improvement of the avatar paradigm. Since the chapters are individual journal articles that have been published or are in preparation, there may be some content repetition between them.

Chapter 2 shows the ability of the characterization process, LS-Imaging, to generate avatars from 3-D XRCT images of specimens of triaxial experiments and track particle and interparticle quantities such as kinematics and contacts. LS-Imaging was verified for accuracy using synthetic images with respect to image resolution and noise, then was applied to two types of granular materials.

Chapter 3 describes the first use of the entire avatar paradigm, from LS-Imaging to LS-DEM, which is introduced and detailed here, to simulate the macroscopic stress-strain and volume-strain behavior of two triaxial specimens of approximately 3,000 particles each of a Martian-like sand. The LS-DEM simulation was calibrated to the behavior of one specimen and used to predict the behavior of the other.

Chapter 4 expands greatly on the avatar paradigm described in Chapter 3, which was used to characterize and simulate a triaxial specimen of approximately 53,000 particles of Hostun sand. Modeling of boundary conditions—the loading platen and membrane—was improved to allow a shear band to form as in the experiment. Although the LS-DEM simulation was calibrated only to the macroscopic behavior of the specimen, it was also able to capture similar particle kinematics and local

behavior, such as that of the shear band, as the experiment. The LS-DEM results of the shear band were analyzed to shed light on its formation and properties.

Chapter 5 summarizes this thesis and provides a future outlook.

Chapter 2

FROM COMPUTED TOMOGRAPHY TO MECHANICS OF GRANULAR MATERIALS VIA LEVEL SET BRIDGE

The content in this chapter is adapted from:

Vlahinić, Ivan, Reid Kawamoto, Edward Andò, Gioacchino Viggiani, and José Andrade (2017). “Towards a more accurate characterization of granular media: extracting quantitative descriptors from tomographic images”. English. In: *Granular Matter*. doi:10.1007/s10035-013-0460-6, pp. 1–13. ISSN: 1434-5021.

Painstaking work by Oda and colleagues throughout the 1970s yielded discoveries of how granular materials evolve at the grain level in response to loading. At the time, via a series of classic triaxial compression experiments, Oda and colleagues first deformed sand to different levels of strain and then “froze” the microstructure in place by injecting polyester-resin, a hardening agent, . This preserved the spatial arrangement of granular particles of sand, or grain fabric, under load. Sand samples were subsequently sectioned and behavioral tendencies of the material during deformation were described in detail. Of specific interest were the patterns of deformation at the grain scale as sand approached critical state – defined macroscopically as the state at which sand maintains a constant shear strength without undergoing further volume change (Schofield and Wroth 1968). The motives of their decade-long studies, as described in the seminal paper by Oda (Oda 1972), were clear:

“In order to realize mechanical properties of granular materials, one must first study in detail morphological and physical properties of granular particles and their configuration relations.”

Four decades later, the above statement rings as true as it did then—except that today, nondestructive 3-D X-Ray Computed Tomography (3-D XRCT) experiments replace destructive (and extremely laborious) experiments by Oda et al. While 3-D XRCT exhibits remarkable potential for truly quantitative grain-scale insight, the continuing challenge has been the interpretation of 3-D XRCT data. The microstructural images coming from 3-D XRCT—3-D fields of X-ray attenuation—are subject to random noise, blur, and geometrical artifacts. To enable quantitative insight, which can

only come from statistical evaluation of grain motion and grain interactions, any approach utilizing these experiments must be able to do the following:

1. Identify individual grains and “extract” them from a 3-D XRCT image, capturing particle morphology.
2. Track these individual grains from image to image, or rather load state to load state, accurately inferring spatial and temporal evolution of grain contacts and grain kinematics.

With respect to the first requirement, the key difficulty lies in the irregularity of individual particles and also in the fact that particles in the image are touching, with each particle having multiple contact points. Overcoming these challenges to gain a mathematical description of each particle, in the form of a level set function, was the subject of our previous work (Vlahinic et al. 2013). In this work, we focus on the second requirement above.

Specifically, we present a methodology based on a level set platform that serves as a total solution for the inference of all geometric quantities that, at present, can be extracted from 3-D XRCT. These include grain contacts (location and contact-normal orientation) and grain kinematics (translation and rotation). Grain contacts or grain fabric can serve as a proxy to stress. For example, Oda and colleagues found that the evolution of fabric is related to the mechanical properties such as mobilized strength and dilatancy (Oda 1972). Also, modern continuum models such as those of Li and Dafalias (Li and Dafalias 2012) have been specifically developed to take into account evolution of grain fabric, which in turn controls the evolution of constitutive properties at the macro scale (Oda and Iwashita 1999). Grain kinematics are directly convertible to strain quantities of choice, for example approaches such as Bagi strain (Bagi 1996) allow a given strain tensor to be derived locally on tetrahedra connecting four grain centroids, from the measured displacement of these four points. Grain rotations, which are particularly relevant during strain localization (Andò et al. 2012a), have a much less immediate connection to continuum strain quantities - which is precisely the reason for studying strain localization at the grain scale in the first place.

We term the proposed platform ‘level set bridge’ precisely because of its potential to relate grain-scale images to continuum mechanics of geomaterials. At the grain scale, the platform is shown to be remarkably accurate, with mean kinematic errors

not exceeding 0.2 voxels and 0.5 degrees (translation and rotation) and mean contact-normal orientation errors not exceeding 0.65 degrees for a wide range of image noise and grain sizes.

In addition to presenting the level set platform, we also report some notable results on real, opaque granular media. For the first time, we show changes in grain fabric in the shear band at the start and the end of a triaxial compression experiment. We quantitatively show that at a granular level, a shear band is characterized by a significant loss of contacts in the direction of minimum principal stress (compression positive) and a significant gain in contacts in the maximum principal stress direction. Changes in contact statistics are not nearly as pronounced in the bulk, i.e., outside of the shear band, though they still track the same tendencies.

Grain kinematics inside the shear band also show some interesting features. Grain translations appear quite predictable, with all grains moving roughly parallel to the orientation of the band, though with a slight normal component due to dilatancy. On the other hand, grain rotations during shearing are much less organized, with polarization of the rotation axes only becoming apparent on average.

As a side note, based on the conclusions above, it can be said that neither 2D experiments nor 3-D experiments containing spherical particles are capable of mimicking grain scale complexities encountered in natural 3-D materials. For this reason, we urge adoption of 3-D codes capable of incorporating complex particle shapes, particularly when discussing statistical results on grain fabric evolution and grain rotations.

The presentation in the rest of the chapter is as follows: Section 2.1 provides a brief recap of a previous paper on LS-imaging. Section 2.2 contains the technical content. In Section 2.3 the results are presented. Finally, in Section 2.4, we provide a summary of main conclusions.

2.1 Review of previous studies

3-D X-Ray CT procedure - experimental viewpoint

XRCT is revolutionizing the field of experimental mechanics due to its ability to image the microstructure in opaque materials. Particularly promising is the ability of XRCT to capture a sequence of images of a deforming material non-destructively, with the promise of quantifying the microstructural origins of macroscale phenomena.

During the experimental process, 2D radiographs (“projections”) are acquired from the sample at a number of different angles from 0 to 360 degrees. The 3-D image is reconstructed, slice by slice (slices are normal to the rotation axis), from 2D radiographs at different angles by solving the inverse problem of the Radon transform. The result is a greyscale 3-D field of X-ray attenuation of a material in a given state (3-D XRCT). There is a strong correlation between X-ray attenuation and material density. Of great importance for the imaging of a given microstructure at the right scale is the resolution of the image (ideally not far from the pixel-size of the image, which describes the physical volume that each 3-D pixel, or “voxel” occupies).

Coupled with an X-ray transparent loading apparatus, 3-D XRCT also allows an uninterrupted sequence of 3-D snapshots, each containing thousands of grains, to be collected over the course of a single experiment. Comparing successive snapshots gives insight into the incremental microstructural changes as a function of an external state (e.g.,load). Unlike at any point in history, this experimental process has created significant opportunities for relating discrete microstructural features to continuum macroscopic quantities (Calvetti, Combe, and Lanier 1997; Andrade and Tu 2009; Oda and Iwashita 1999). The process has also helped steer research focus from phenomenology towards a more physics-based approach, with the promise of validating and improving models for granular media, and just as importantly, unmasking the physical origins of observed phenomena such as shear bands (Andrade et al. 2010; Rechenmacher and Finno 2004; Andò et al. 2012b).

Extracting grains from 3-D X-Ray CT - a birds-eye view

A significant challenge in using imaging (such as 3-D XRCT) for quantitative analysis lies in the the translation of what are essentially three dimensional photographs into palatable “quantities”. In other words, the photographs need to be converted into quantitative descriptors of particle morphology and kinematics that can then be used in quantitative analysis. This step helps reduce what are extremely large data sets (typically 1500x1500x1500 voxels) into a smaller set of geometric and/or statistical descriptors. From a physical perspective, the key difficulty lies in identifying grains as individual units, i.e.discriminating grains from voids (separating phases), and also grains from other grains (separating objects). This is challenging because grains can take on complex shapes and touch at contacts, which complicates differentiating grains from other grains.

To generate quantitative descriptors of these 3-D XRCT images, we use an edge-

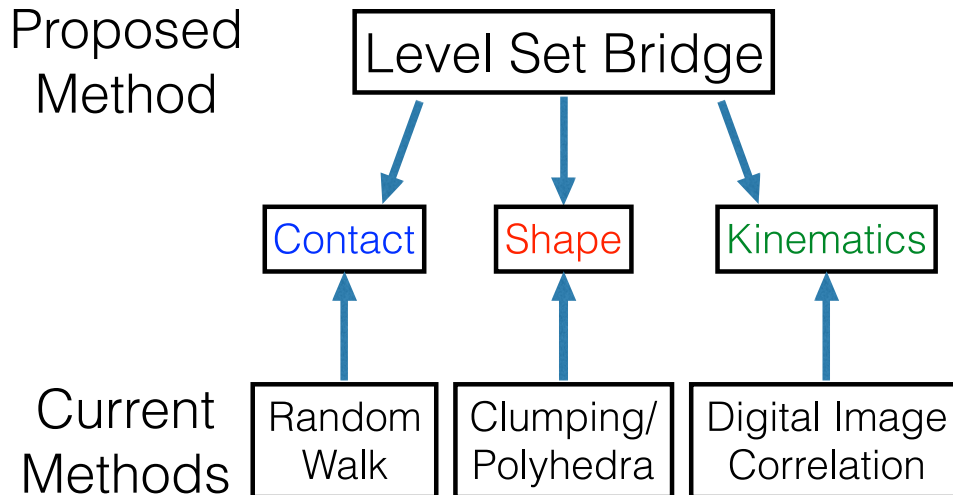


Figure 2.1: Overview of proposed method versus current methods. The bridge is a total solution for characterization, while current methods require separate algorithms. See (Vlahinic et al. 2013) for more on extracting shape from 3-D XRCT images.

based variational level set (LS) method (Caselles et al. 1993; Kichenassamy et al. 1996; Li et al. 2005; Li et al. 2010; Osher and Sethian 1988) that is free from voxelated structures. Instead, the algorithm works directly on greyscale 3-D XRCT images to translate these to smooth descriptions of particle morphology by locating a grain surfaces in a reconstructed 3-D XRCT image via locally minimizing an appropriate energy functional. To this end, an LS function which is the same size as the image domain is created, and its zero LS contour is subsequently evolved until the scalar energy functional of its LS function is minimized.

Figure 2.1 provides a brief snapshot of the results available using the proposed LS-based methodology. That we can visually discriminate morphology (rounded versus angular) of the individual grains on the order of 100 microns speaks to both the success of the 3-D XRCT experiments and also of the LS based platform for interpreting the data.

2.2 Algorithms for grain fabric and kinematics

In a typical experiment on sand, a “representative” sample may be comprised of tens of thousands of grains, which provides an impetus for devising a computer-automated process for analysis. This process should, from a single 3-D XRCT image, identify individual particles, determine their shape and morphology, and determine orientation of contacts between particles. Furthermore, using multiple

3-D XRCT images at successive stages of loading, such a process should also be able to track particles from image to image (translation and rotation) based on their morphological footprint as well as the evolution of contacts. Ultimately, this process should shed insight into the incremental microstructural changes of the sample as a function of external state (e.g. loading). In practice, however, such a process has been absent until now. We describe this new process below using level sets as a platform for interpreting 3-D XRCT images.

Grain description via Level Sets In our previous contribution (Vlahinic et al. 2013), we introduced a level set methodology to extract individual grains from 3-D XRCT images. The advantage of LS in describing complex geometric shapes is that it resides on a regular Eulerian grid identical to that of the underlying image. In this way, different grain shapes take on different functional values, while the underlying computational grid remains the same.

In mathematical terms, a grain surface Γ is defined as a zero-level contour of the level set function $\phi(\mathbf{x})$, where \mathbf{x} describes a 3-D domain. In the grain interior, namely in the region Ω^- , ϕ is negative, while in the grain exterior, namely in the region Ω^+ , ϕ is positive, such that:

$$\begin{aligned}\phi(\mathbf{x}) < 0, & \text{ region inside grain surface, denoted by } \Omega^- \\ \phi(\mathbf{x}) = 0, & \text{ grain surface } \Gamma, \text{ denoted by } \partial\Omega \\ \phi(\mathbf{x}) > 0, & \text{ region outside grain surface, denoted by } \Omega^+\end{aligned}$$

In principle, any function satisfying the above criteria can be used as an LS function. However, a signed distance function is typically adopted because it provides the following convenient properties:

$$|\nabla\phi| = 1; \quad \mathbf{n} = \frac{\nabla\phi}{|\nabla\phi|} = \nabla\phi \quad (2.1)$$

where ∇ is the gradient operator and \mathbf{n} is the vector normal.

A signed distance function also enables a quite accurate determination of a grain centroid, via a volume integral. Recall that all material points belonging to the grain, $\mathbf{x} \in \Omega^-$, are simply those satisfying the constraint $\phi(\mathbf{x}) < 0$, while on the grain surface $\mathbf{x} \in \partial\Omega$, $\phi(\mathbf{x}) = 0$. In this way, we may define a volume integral on Ω^- , such that

$$\text{volume integral} \quad \int_{\Omega} H(-\phi(\mathbf{x})) dx$$

with $H(\phi)$ representing the integral of the Heaviside function, the solution of which is a volume of Ω^- . In practice, for improved numerical accuracy, $H(\phi)$ is typically smeared over a finite distance $\epsilon = 1.5$ (Osher and Sethian 1988), expressed in grid units:

$$H(\phi) = \begin{cases} 0 & : \phi \leq -\epsilon \\ \frac{1}{2} + \frac{\phi}{2\epsilon} + \frac{1}{2\pi} \sin\left(\frac{\pi\phi}{\epsilon}\right) & : -\epsilon \leq \phi \leq \epsilon \\ 1 & : \epsilon \leq \phi \end{cases}$$

A centroid may then be calculated as

$$\mathbf{x}_c = \frac{\int_{\Omega} H(-\phi) \mathbf{x} d\mathbf{x}}{\int_{\Omega} H(-\phi) d\mathbf{x}} \quad (2.2)$$

The rest of the technical sections assume LS functions of individual grains is available to the user, determined per recipe discussed in our previous work.

Grain contacts (fabric) The level set platform provides a simple procedure for determination of grain fabric. To this end, we first define a proximity function between each ‘‘possibly contacting’’ pair of grains :

$$\text{grain proximity} \quad f(\phi_1, \phi_2) = \max [\phi_1(\mathbf{x}), \phi_2(\mathbf{x})]$$

where ϕ_1 and ϕ_2 are the level set functions of a given pair of grains. Like the level set functions, the proximity function is defined on the Eulerian grid. $\min f(\phi_1, \phi_2)$ identifies a grid point where the two level sets, and thus neighboring grains, are closest together. A grid point does not represent a closest point between the two surfaces, however. This is because a true grain surface is located at arbitrary locations within the grid, being the zero contour of ϕ . As a result, contact location and also the orientation need to be determined in an average sense, in terms of the proximity function. The simplest approach is to perform weighted averaging, with weights decaying quickly away from the contact region. Here, we adopt a function of exponential form, such that:

$$\text{contact weights} \quad w(\phi_1, \phi_2) = \frac{1}{\exp[f - f_0]}$$

where a normalizing constant $f_0 = \min(f)$. The constant is included to ensure that the highest weight is unity at all contact pairs. With these expressions in mind, we

create a definition for calculating the contact centroid and normal as follows:

$$\begin{aligned}
 \text{contact centroid} \quad \mathbf{x}_{contact} &= \frac{\int_{\Omega} w \mathbf{x}}{\int_{\Omega} w} \\
 \text{contact normal} \quad \mathbf{n}_{contact} &= \frac{\mathbf{n}^*}{\|\mathbf{n}^*\|}, \quad \text{where } \mathbf{n}^* = \int_{\Omega} w (\nabla\phi_1 - \nabla\phi_2)
 \end{aligned} \tag{2.3}$$

Note that contact normal has no preferred orientation, or rather \mathbf{n}^* and negative \mathbf{n}^* identify the same contact normal.

Grain kinematics The level set platform provides a similarly simple procedure for determination of grain kinematics. Both grain translation and rotation can be found using a single algorithm. This is accomplished by minimizing an appropriate cost function, dependent on the difference between LS functions at distinct (imaged) load stations. In a physical experiment, recall that grains are imaged independently, and the same grain at two different load stations will have a different orientation and therefore different level set functions. Thus, a minimization procedure is required to correlate the two different level set functions of the same grain in order to find its kinematics. We assume that the grains are rigid, i.e., the incremental grain movement entails rigid body motion only (a lack of grain deformation is a valid assumption for sand-type materials). Furthermore, we assume that grains remain whole, i.e., there is no particle breakage. This assumption is valid for the low-confinement experiments studied in this chapter, but if particles do break, a more robust algorithm would need to be developed. The ultimate goal is to characterize grain rearrangement, leading to macroscopic plasticity phenomena.

A cost function to be minimized can be defined in terms of the displacement and rotation vectors. Translation is simply a three-component vector $\mathbf{t} = (t_x, t_y, t_z)$. Defining rotational degrees of freedom is a slightly more involved. As a starting point, it helps to adopt an *axis-angle* representation, where 3-D rotation is defined by a unit vector $\mathbf{b} = (b_x, b_y, b_z)$ and rotation angle θ around the unit vector. In this way, via a Rodrigues rotation formula, a 3-D rotation tensor \mathbf{r} is defined such that in indicial notation,

$$R_{ij} = \cos \theta \delta_{ij} + (1 - \cos \theta) b_i b_j - \sin \theta \epsilon_{ijk} b_k$$

where δ is the Kronecker delta and ϵ is the permutation or Levi-Civita tensor.

Rather than using 4 rotational unknowns, with a restriction that $\mathbf{b} \cdot \mathbf{b} = 1$, we introduce the following parameterization: $\mathbf{r} = \sin \frac{\theta}{2} \mathbf{b}$. This eliminates the trigonometric functions, restriction on \mathbf{b} , and leads to only three independent unknowns, namely $\mathbf{r} = (r_x, r_y, r_z)$ with $\theta(\mathbf{r}) = 2 \sin^{-1}(\mathbf{r} \cdot \mathbf{r})$. Noting the identities $2 \sin^2 \frac{\theta}{2} = 1 - \cos \theta$ and $\sin 2\theta = 2 \sin \theta \cos \theta$, the substitutions ultimately reduce the Rodrigues rotation formula to,

$$R_{ij} = (1 - 2r_l r_l) \delta_{ij} + 2r_i r_j - 2\sqrt{1 - r_l r_l} \epsilon_{ijk} b_k$$

A scalar cost function can finally be constructed (Jenkinson et al. 2002), where

$$C(\mathbf{g}) = \frac{1}{2} \sum_{\alpha=1}^w [\phi^n(\mathbf{x}^\alpha) - \phi^o(\mathbf{m}^\alpha)]^2$$

(2.4)

where $\mathbf{x}^\alpha = \mathbf{t} + \mathbf{r}(\mathbf{r}) \cdot \mathbf{m}^\alpha$

with $\mathbf{g} = [\mathbf{t}, \mathbf{r}]^T$ being the parameter vector over which minimization will take place. Vector \mathbf{m}^α represents a collection of relative distances between α number of points in Ω^- and the grain centroid, as determined at time step $t = 0$. Note that ϕ is initially evaluated at a starting configuration, namely ϕ^o , and therefore its interpolation is not needed. However, ϕ^n corresponding to a particle's LS function at any subsequent load station is evaluated at the arbitrary locations \mathbf{x}^α , which does require interpolation.

There are several popular methods that can be used to minimize the residual $C(\mathbf{g})$. The quickest are gradient-based methods, which, at minimum, require evaluation of the first-order gradient of $C(\mathbf{g})$. Analytic expressions for the gradient of C can be found in (Jenkinson et al. 2002), though they are not necessary to implement. A quasi-Newton method available in MATLAB allows for a numerical evaluation of the gradient of $C(\mathbf{g})$, requiring on average 5-25 iterations to reach a final solution, depending on the magnitude of the rotation angle. We found that a unit length maximum must be imposed on the magnitude of vector \mathbf{r} during each iteration. Besides this restriction, we find no problems in terms of convergence. In real tests using a MATLAB implementation (“fminunc”) on a standard Intel i7 laptop, even for very large angular rotations of up 90 degrees, we find that the method converges to a solution in approximately one second for the grid sizes used in this study. We believe that this is a byproduct of a smooth profile of the LS function that describes grains, in contrast to, for example, applying the same algorithm directly to noisy

source images such as the grain-based Discrete Digital Volume Correlation (Andò et al. 2012a).

Note that grain translation is estimated to a great precision from information about the centroids. As such, vector of unknowns \mathbf{g} can be modified to contain only rotational unknowns, i.e., $\mathbf{g} = \mathbf{r}^T$, reducing the 6 unknowns to 3. However, we also find that keeping all 6 unknowns does two things: (1) it provides an independent check on the converged results, without significant overhead with respect to minimization, and (2) it can ultimately help improved particle characterization, with slightly better matching between the reference and new state.

2.3 Results

We apply the algorithms presented in the previous section to three types of grains: synthetic grains, glass ballotini, and Caicos ooid sand. We first apply our methods to synthetic images to validate their accuracy, then to ballotini to examine a real but idealized and simply-shaped material, and finally to Caicos ooids to analyze an actual geological granular system. In the cases of ballotini and Caicos ooids, we looked in particular at the behavior of grains and fabric in the shear band of a triaxial test. Table 2.1 shows a summary of the analyses performed in this section.

Material	Type	Translation	Rotation	Contact
synthetic	computer generated	Y	Y	Y
ballotini	engineered glass	Y	N	Y
Caicos ooid	natural sand	Y	Y	Y

Table 2.1: Summary of experiments and statistical inferences performed as part of this study.

Synthetic test: accuracy with respect to image resolution and image noise

In this section, we apply the algorithms presented in the previous section to synthetic images of grains. Synthetic images are created by discretizing analytical functions of geometric shapes into volumes over a voxelated grid, where image intensity corresponds to the volume fraction of the shape(s) in each voxel. This process leads to images analogous to XRCT images, whose intensity corresponds to the density of each voxel (Vlahinic et al. 2013). The synthetic study is done to determine the accuracy of the level set based algorithms. Image resolution (voxels per grain diameter), white noise (signal to noise ratio) and also contact topology (convex versus concave) vary in the expected range of 3-D XRCT images. This study is done as a precursor to the analyses on real grains in the following two sections.

For the test of accuracy of the contact normal calculations, we synthesize results of one thousand 3-D XRCT-like images of two grains contacting at randomly assigned orientations. A typical image of a synthetic contact is shown in Figure 2.2. Figure 2.3 shows the results of this test. Each column in the figure corresponds to a particular contact geometry. The top row of the results varies the image noise σ from 0 to 5% standard deviation of signal to noise ratio, keeping the average grain diameter D fixed at 30 voxels. The bottom row varies the grain diameter between 20 and 40 voxels without introducing any noise.

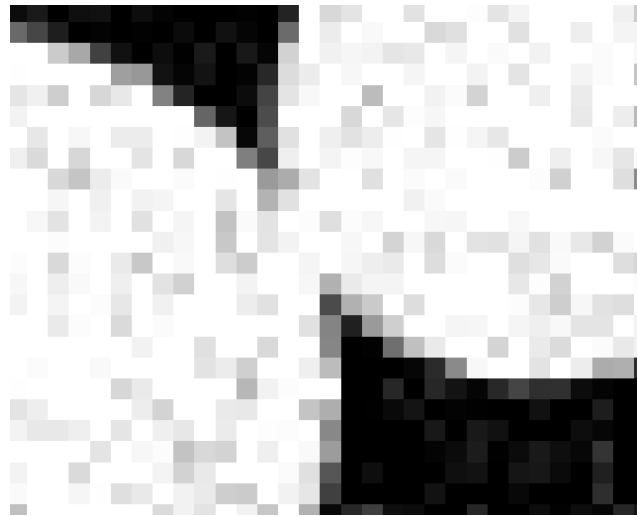


Figure 2.2: An image of a convex-convex synthetic contact with random noise ($\sigma = 0.01$) of two synthetic grains of diameter 30 voxels, typical of images of synthetic contacts in this section. Note that the image shown is a 2-D slice of a 3-D image.

The following are general conclusions, which can be gleaned from the histogram data:

1. For the range of image resolutions used in this study, between 20 and 40 voxels per grain diameter, image resolution has little influence on the overall results, regardless of the contact type.
2. In relative terms, convex-convex grain contacts yield the most accurate results, while convex-concave contact types yield the least accurate results. Contact type appears to have the largest impact on accuracy. However, for all resolutions and noise levels, the mean error in contact orientations is below 1 degree.

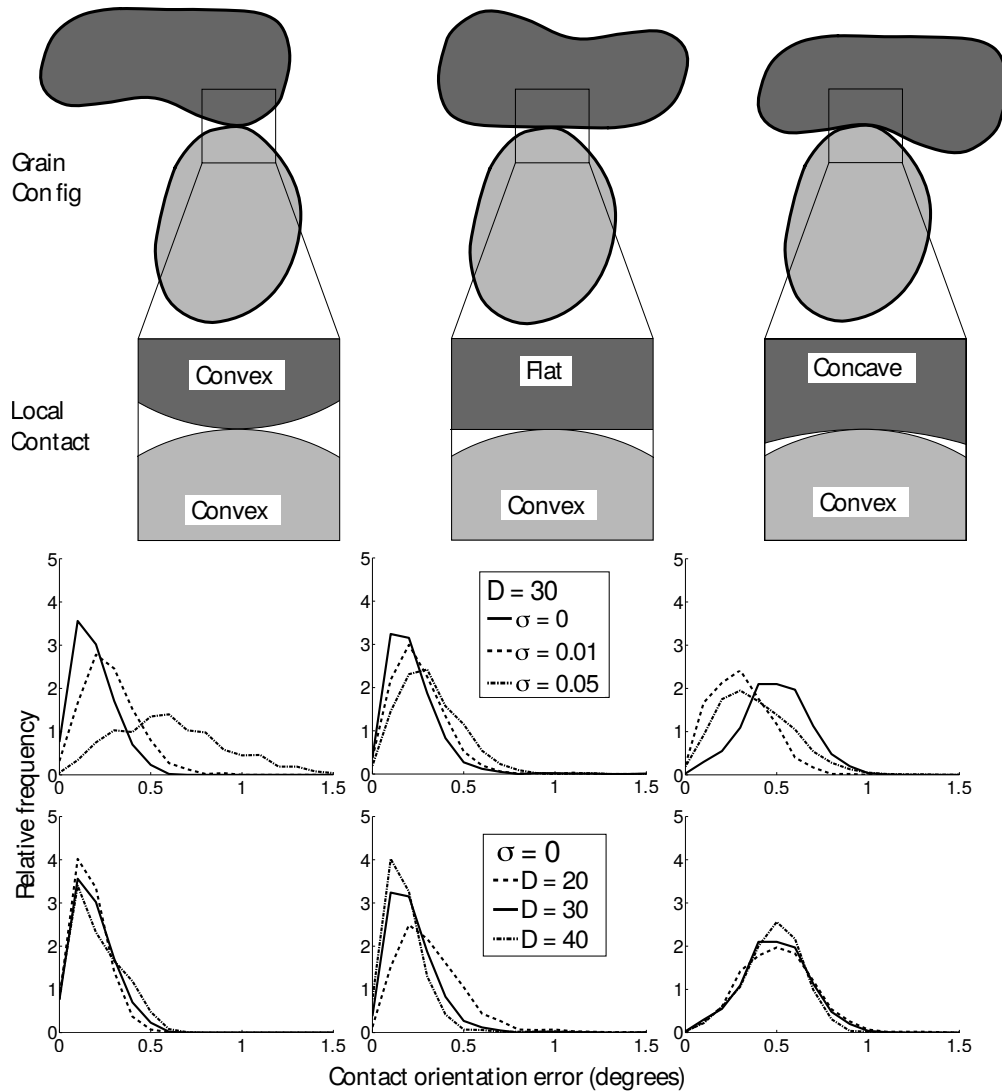


Figure 2.3: 2-D schematic of the three different contact types, with magnified insets. Below, histograms of contact orientation errors for 1000 trials each of two contacting grains in random orientations, for varying levels of white noise σ (signal to noise ratio) and grain resolution D (voxels per grain diameter). Note that while the schematic above is 2-D, all tests and reported results are based on 3-D geometries.

3. As expected, noise level and accuracy are shown inversely proportional. This is most apparent for the convex-convex contact type, where the average error with 5% noise is more than triple the average error with no noise. However, even with 5% noise, the average error in contact orientation is still only 0.62 degrees. In the convex-flat and convex-concave cases, noise level makes little difference.

In the test of accuracy of grain kinematics, we synthesize results of a single grain in one thousand random initial and final positions and orientations, and calculate the displacement and rotation errors, comparing those results to the exact values used to synthesize the images. A typical image of a grain used in this study is shown in Figure 2.4. Figure 2.5 shows the results of this test. The left column corresponds to rotation tests, while the right column corresponds to translation tests. Variations in resolution and noise remain identical to the previous test, namely 0 to 5% std. deviation of signal to noise ratio and 20 to 40 voxel grain resolution.

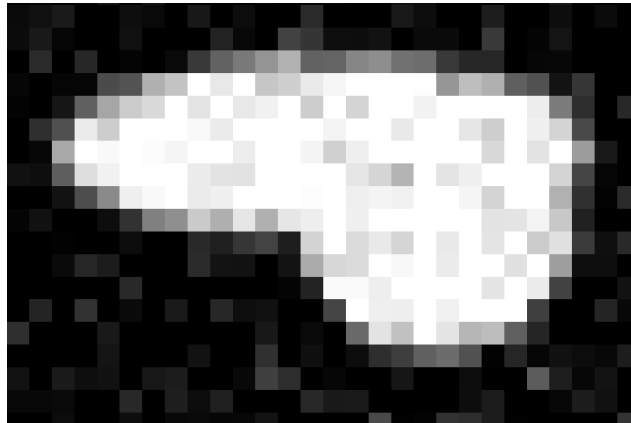


Figure 2.4: An image of a synthetic, randomly oriented grain with random noise ($\sigma = 0.01$) and a diameter of 30 voxels used in the test of kinematic accuracy, typical of images of synthetic grains used to track kinematics in this section. Note that the image shown is a 2-D slice of a 3-D image.

The following again are our general conclusions:

1. In terms of grain rotation, noise level and accuracy appear inversely proportional. The error, however, is very well controlled, not exceeding the mean 0.5 degrees (with respect to absolute values) at the highest noise level.
2. Higher resolution images lead to higher kinematic accuracy. There appears to be a cutoff point at which a higher resolution ceases to significantly affect accuracy. Nevertheless, in all cases, the error appears well controlled, with subvoxel accuracy in all cases.

Glass ballotini

We now turn to the first of two sets of results on real granular materials imaged via 3-D XRCT. Ballotini, an engineered glass material, is chosen for its nearly spherical grain shape and varied size, with diameters between 150 and 600 μm .

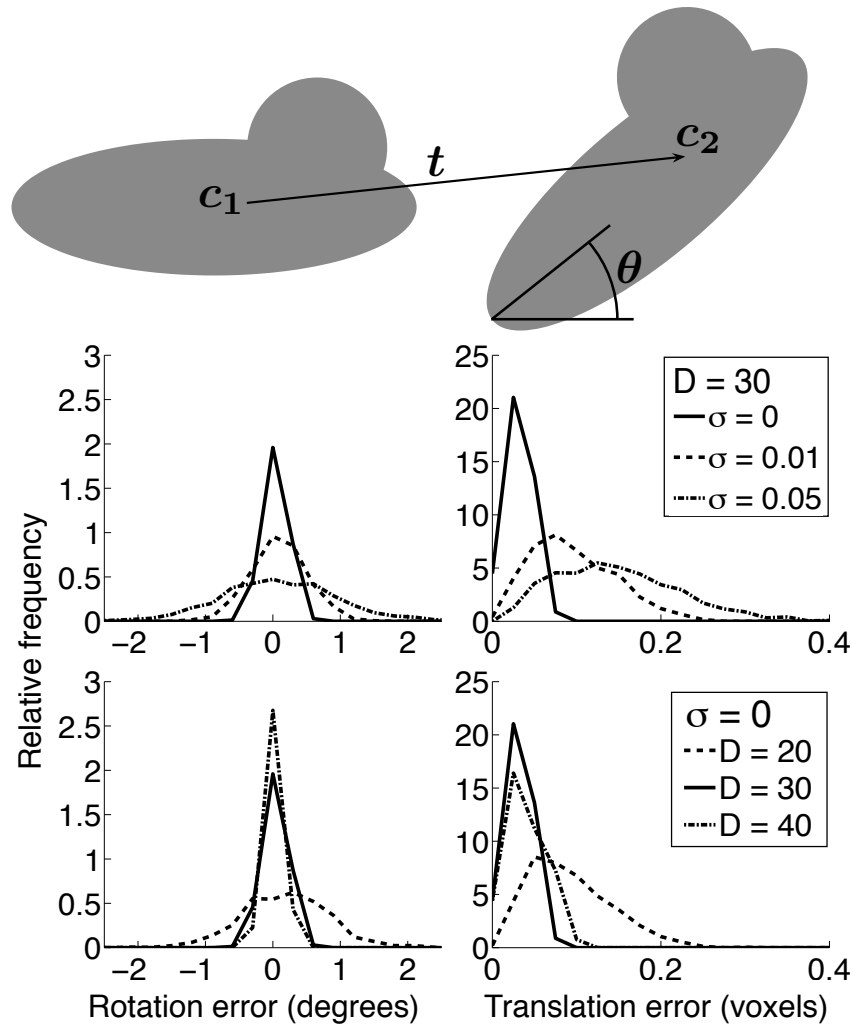


Figure 2.5: Histograms of rotation and translation errors for 1000 trials each of a single grain translating and rotating from an initial position and rotation to a random position and rotation, for varying levels of noise σ and grain diameter D . Note that while the schematic above is in 2-D, all tests performed are 3-D.

Owing to their spherical shape, ballotini grains are constrained in terms of contact type, experiencing only convex-convex contacts, though at different resolutions as reflected by differences in their particle size. 3-D XRCT images taken at four time stations are of particular note: time stations 1 and 2, representing the beginning of loading, and time stations 16 and 17, representing the post-localized state of the material under triaxial compression (see Figure 2.6).

In the middle portion of the sample, incremental grain translations are first calculated by subtracting the grain centroids of individual grains from successive load steps, namely load step 1-2 and 16-17, per the procedure outlined in the previous section.

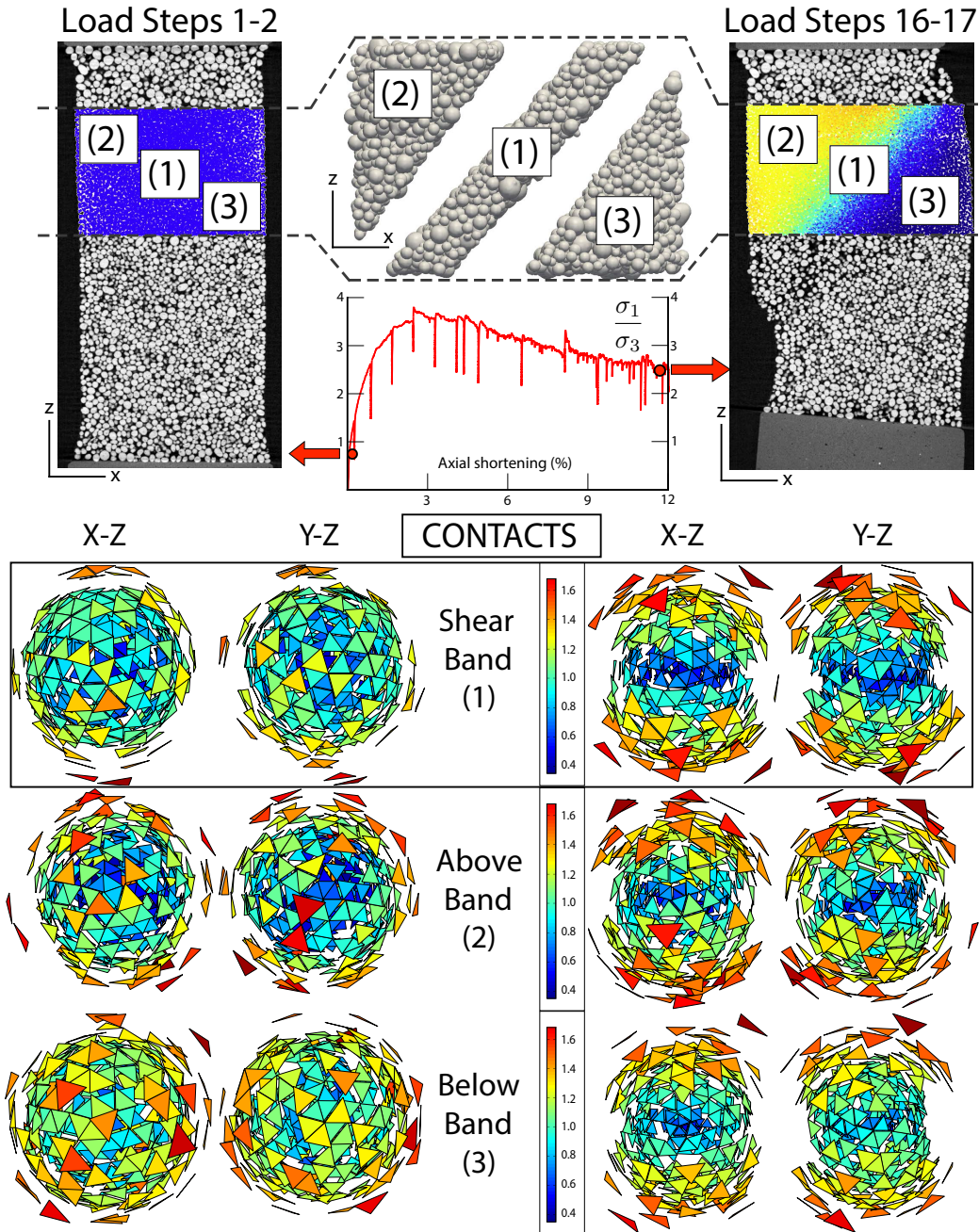


Figure 2.6: 3-D XRCT images of ballotini specimen at the onset of loading and post-localization (top), along with the macroscopic stress-strain. Contact statistics are reported for a region inside and two regions outside of the shear band. Individual grains belonging to these regions are shown as level set contours in top middle of the figure. The overlay over 3-D XRCT images is colored by displacement magnitude of individual grains, an indicator of the shear band location. Contact statistics (bottom histograms) show the relative frequency of contacts occurring in a given direction, indicated by the distance of a given triangle from the origin. We see a significant loss of contacts in the horizontal directions (minimum principal stress; compression positive) and significant gain in the contacts in the maximum principal stress direction, as reported in multiples of mean contacts per grain in each region (e.g., 1.3 corresponds to 130% of the mean contact frequency in a given direction).

The translations are shown collectively, per a color overlay of the original 3-D XRCT images a top left and right of Figure 2.6. Greatest incremental translations correspond to roughly 3.5 voxel units, or just under 0.1 mm. Incremental rotations cannot be determined because the ballotini grains are nearly spherical. Note that all calculations are performed in 3-D, though for simplicity, only a 2D slice is shown in Figure 2.6.

Based on the incremental translations, the shear band region can clearly be delineated. For this study, in total, we choose three sub-regions to analyze: volumes above and below the shear band, and a volume within the shear band. These regions are clearly identified at top of Figure 2.6. In addition, extracted level set contours, i.e., mathematical representations of the particles in these regions, are shown in top middle of the figure.

For this example we are particularly interested in changes in the distribution of contact normals between the onset of loading and post-localization in each of the three regions. As discussed in the introduction, contact normals are an important quantity for granular materials, as gravity forces dominate at scales roughly above 1/10 mm (Santamarina 2003) and forces within the material are distributed via physical grain-grain contacts. In this way, contact orientation serves as a proxy for understanding changes the load-resisting network within the material (Behringer et al. 2014).

Results from our statistical analysis, in the form of histograms plotted in spherical coordinates, are shown in the lower part of Figure 2.6. The scale of its plots, indicated by blue-to-red colors, is reported in multiples of the mean number of contacts per grain. Directions are grouped into triangles of equal areas, as seen in the histogram plots. X and Y axis were aligned such that the shear band lies in the X-Z plane.

That the contact histograms look nearly spherical (or circular in 2D projections) indicates that at the onset of loading contacts were evenly distributed in all directions. Post-localization, however, a significant gain in contact density in the direction of loading (vertical z-direction) is evident in all regions of the sample, though the greatest gains are visible inside the shear band, where the gain in contact density is roughly 150% of the mean. Conversely, the contact density in the sample decreases in the direction of smaller principal compressive stress (radial specimen directions x and y). Again, the greatest losses are concentrated in the shear band regions, where density falls to 50% of the mean.

Caicos ooids

Caicos ooids, a highly rounded sand originating in the warm waters of the Caribbean, presents a truly natural material. We apply level set methods to 3-D XRCT snapshots taken at different time stations of a triaxial compression test on ooids. Stress-strain for the material curve is shown in top middle of Figure 2.7, marked by post-peak strength softening accompanied by shear band localization. Though rounded, the particles are not constrained in terms of shape, with many exhibiting elongated shapes and occasional non-convexity.

In terms of contact statistics, as in the case of ballotini, we examine contact normal orientations at the onset of loading and at the post-localized material state. These correspond to load stations 1 and 17. Changes in contact statistics are reported in Figure 2.7. Only the shear band region is studied, containing roughly three thousand independent contact surfaces. Tendencies of the material to gain contacts in the direction of loading and lose contacts in the minimum principal stress direction remain consistent with the previous example. Similarly, highest contact density appears to be in the same direction as the principal loading direction.

The difference here, however, is that the magnitude of the contact gains and losses is more exaggerated than that of the ballotini experiment. We believe this to be a product of non-spherical grain shape. In other words, as grain shape becomes less spherical, contacts densities in minimum and maximum principal stress directions tend toward greater extremes. This is evident by simply looking at the shape of the histogram, which visually reflects its color values. Also, contact densities in and out of the plane of shearing (X-Z and Y-Z planes) become more dissimilar, despite the fact that macroscopically, principal stress is the same in all radial directions.

At bottom of Figure 2.7, incremental translations (in voxel units) and rotations (axis and magnitude) are shown for the twelve grains that remain inside the subregion during all 16 loading stages. Each colored line identifies a cumulative path of a different grain. Grains that enter or leave the region during all load steps are not shown, though they follow the same pattern of behavior described next. Primarily, we observe that the direction of grain motion very predictably reflects the orientation of the shear band. Also, as expected, it can be seen that the grains are also slightly moving apart from one another, i.e., with a small band-normal component, indicating dilative tendencies of the Caicos sample.

More interesting, however, is the rotational freedom of grains, or rather a lack thereof. Specifically, cumulative grain rotations plotted in vector form (vector magnitude =

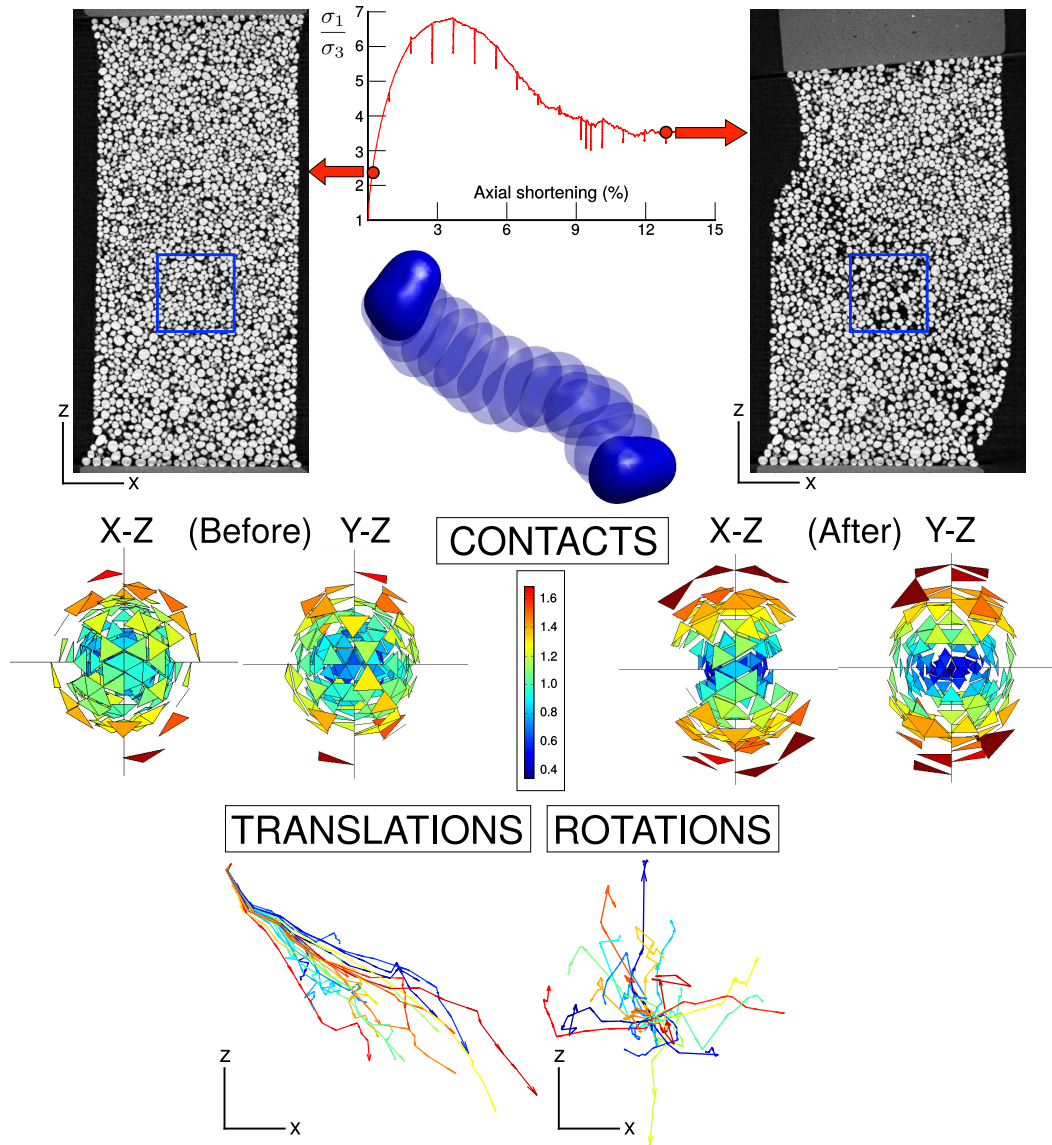


Figure 2.7: 3-D XRCT images of Caicos ooid specimen at the onset of loading (left) and post-localization (right), with the analyzed subvolume encompassed by a blue square. In the middle, statistical histogram of contacts is shown for loads steps 1 and 16. Description of the axis and scale is the same as for glass ballotini. At the bottom, incremental translations (in voxel units) and rotations (axis and magnitude) are shown for the 15 grains that remained inside the subregion during all 16 loading stages. Note the grain rotations appear entirely random, seemingly unaffected by shear band orientation or loading direction. The kinematics of one of the grains during all loading stages (shown in blue) exemplifies typical temporal resolution available in a 3-D XRCT experiment.

magnitude of rotation; vector direction = axis of rotation) indicate that rotations within shear band vary wildly. To the authors, at least, it is quite surprising that grain rotations display little to no correlation with shear band orientation or loading direction. In other words, in natural 3-D materials, rotations appear subservient to translational degrees of freedom, with grains relieving their frustration by rotating in any direction possible, as dictated by local geometric constraints.

In terms of relative magnitude, cumulative grain kinematics during loading to critical state are significant. We consistently find cumulative rotations up to 180 degrees (though in diverging incremental directions) for each translational equivalent of two particle diameters.

2.4 Conclusions

In this work, we present our level set platform, termed “level set bridge.” The platform provides a crucial link between X-ray CT experiments and micro mechanics of granular media. In particular, it enables us to not only extract particle morphology from 3-D XRCT images, but also to leverage this information to report with great accuracy the spatial interactions between particles (contact statistics) as well as grain-level kinematics (particle rotations and translations) as a function of load state. The following studies were performed as part of this work:

First, motion and contact of synthetic grains was studied in order to determine the accuracy of the platform. It was found that the proposed platform produces excellent results - indicating the rotation error does not exceed half a degree at typical 3-D XRCT noise level and resolution. Grain kinematics between successive load steps also proved quite accurate, with mean translation error limited to a fraction of a voxel and mean particle rotation error at a fraction of one degree in 3-D.

Second, the algorithm was applied to two real materials, glass ballotini and Caicos ooids, sieved to limit the particle size to those of typical sand (with mean grain diameter in the range of 0.2 mm). At this scale, gravity forces dominate¹. 3-D quantitative statistics in the regions inside the shear band for non-spherical particles are reported for the first time in literature.

This represents the highest resolution quantitative (i.e., grain-scale kinematics and fabric) in-situ experimental study of its kind on 3-D real materials thus far. Level set based algorithmic accuracy enabled new insight into material state before and

¹along with capillary effects, but in this study, the specimens were tested dry and not affected by capillary effects

after localization. Main findings were summarized in the introduction section, and detailed in the results section. Ultimately, what made this study possible were advances in both experimental 3-D XRCT technology (Andò et al. 2012b; Andò et al. 2012a) and also advances in interpretation of image-based data (Li et al. 2010), as exemplified by our previous published works (Andrade et al. 2012a; Vlahinic et al. 2013).

*Chapter 3***LEVEL SET DISCRETE ELEMENT METHOD FOR
THREE-DIMENSIONAL COMPUTATIONS WITH TRIAXIAL
CASE STUDY**

The content in this chapter is adapted from:

Kawamoto, Reid, Edward Andò, Gioacchino Viggiani, and José E. Andrade. “Level set discrete element method for three-dimensional computations with triaxial case study”. In: *Journal of the Mechanics and Physics of Solids* 91, pp. 1–13. doi: <http://dx.doi.org/10.1016/j.jmps.2016.02.021>. ISSN: 0022-5096.

In this chapter, we describe and validate the level set discrete element method (LS-DEM) which enables the simulation of systems of arbitrarily-shaped 3D particles using level set functions as a geometric basis. LS-DEM is similar to the classic discrete element method (DEM) (Cundall and Strack 1979) in that it simulates the kinematics and mechanics of a system of discrete particles, with the only difference being its ability to model arbitrary shapes as opposed to only spheres as in DEM. LS-DEM was motivated for three reasons:

1. Particle shape plays an enormous role in determining the macroscopic properties of an assembly, particularly strength, which has been shown both experimentally (Cho, Dodds, and Santamarina 2006) and computationally (Jerves, Kawamoto, and Andrade 2016), thus having a method able to account for particle shape is paramount. Level set functions represent the next step in high-fidelity shape representation and are able to fully capture the complex morphology of real granular materials.
2. Recent developments in the characterization of grain assemblies from X-ray computed tomographic (XRCT) images of granular systems using level set imaging methods (Vlahinic et al. 2013) have provided particular reason to develop a level set-based simulation method that can directly use the level set data from characterization of XRCT images as an input, avoiding the need to switch geometric formulations.
3. The level set framework is computationally time-efficient, even at high resolutions, due to its formulation.

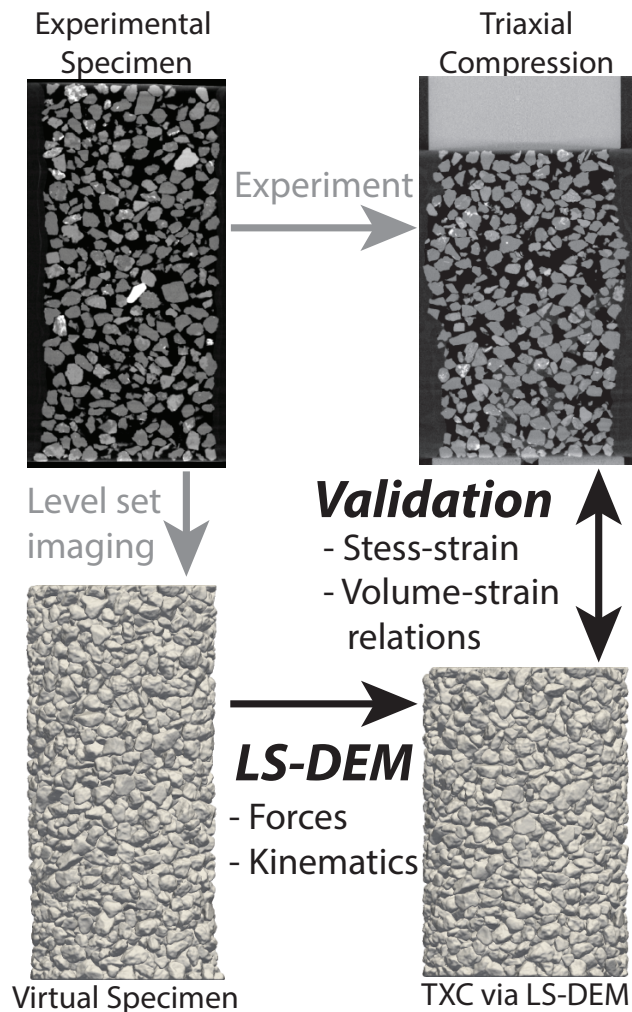


Figure 3.1: Illustration of this chapter’s contents, LS-DEM and its validation (bold-italicized), which are the links that allow us to fully connect the four areas between experiments and computations. Note that the experimental images are 2D slices of a 3D XRCT image, and the virtual specimen is 3D.

With these motivations in mind, we describe the level set-based shape representation and contact algorithms unique to LS-DEM, then verify the method by applying it to two virtual assemblies obtained from XRCT images of experimental specimens. As shown in Figure 3.1, LS-DEM and its validation represent the the links in being able to fully bridge the gap between experiments and computations in discrete modeling with full-sized specimens.

3.1 Level set discrete element method

Here, we detail the level set discrete element method, starting with level set functions, moving to interpolation and computation of inertial properties using level set

functions, and ending with contact, forces and moments, and motion in LS-DEM.

Level set functions

A level set function is a scalar-valued implicit function $\phi(\mathbf{p})$ whose value is the signed distance from a point \mathbf{p} to an interface (Osher and Fedkiw 2003). In the context of LS-DEM, the interface is the particle's surface. Consider a grain particle surface such as the one in Figure 3.2a. Contour lines can be added around the grain surface as in Figure 3.2b. These contour lines represent the distance or 'elevation' from the grain surface, positive outside the grain and negative inside the grain. Next, a grid can be superimposed over the contours as in Figure 3.2c and the elevation can be found at each grid point. Figure 3.2d illustrates the elevation at each grid point, and this is the level set function which is stored in computer memory and is the geometric basis of LS-DEM.

Although level set functions can be constructed through the method above, i.e., using point-distance formulas to arrive at Figure 3.2d, all of the level set functions in this chapter are generated from XRCT images of experiments on real grains using level set-based imaging algorithms in (Vlahinic et al. 2013).

Through interpolation of values at surrounding grid points, the value of the level set function at any point can be evaluated (Figure 3.2e). We define $\Omega^+ = \{\mathbf{p} \mid \phi(\mathbf{p}) > 0\}$ as the outside of the grain and $\Omega^- = \{\mathbf{p} \mid \phi(\mathbf{p}) < 0\}$ as the inside of the grain. Then, the original grain surface (Figure 3.2f) can be reconstructed by finding the set of points $\partial\Omega = \{\mathbf{p} \mid \phi(\mathbf{p}) = 0\}$ (the "zero level set") via interpolation.

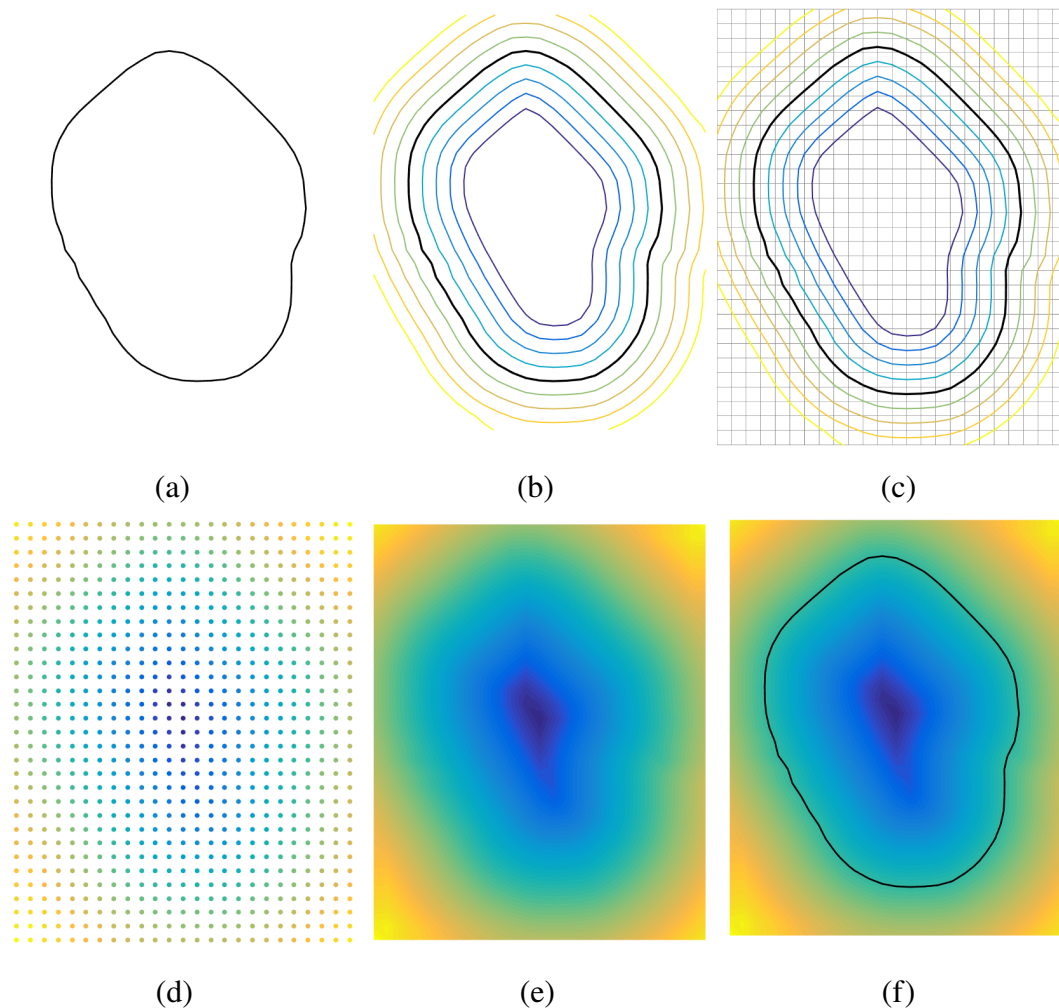


Figure 3.2: Illustration of a level set function. (a) Grain particle surface. (b) Contour lines representing signed distance from surface. (c) Superimposition on grid. (d) Discretized level set function. (e) Level set function with interpolation between grid points. (f) Reconstruction of original grain surface via interpolation. Note that the level set functions shown here are 2D for illustrative purposes only.

Interpolation in level set functions

For use in the level set discrete element method, we must be able to compute two quantities from a level set function ϕ : its value $\phi(\mathbf{p})$ and its gradient $\nabla\phi(\mathbf{p})$ at any point \mathbf{p} within its grid boundaries. This is done through interpolation of values of the discretized level set function at grid points surrounding \mathbf{p} . Any order of interpolation can be used, but linear interpolation was used here for its simplicity and speed. Let:

1. ϕ be stored on a uniform grid with grid spacing g in all directions.

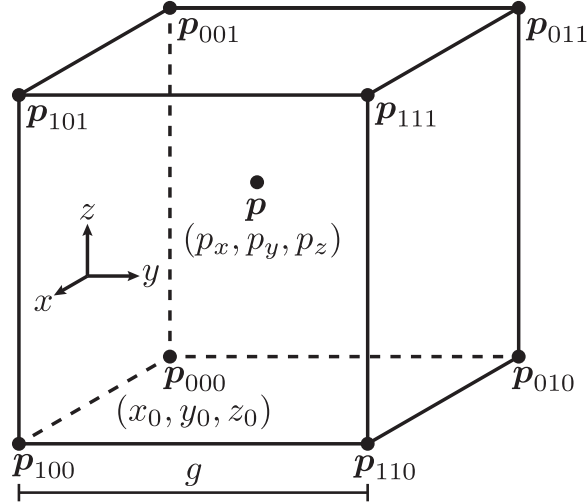


Figure 3.3: Schematic of point \mathbf{p} with surrounding grid points \mathbf{p}_{abc} .

2. \mathbf{p} be a point in space with components p_x , p_y , and p_z and surrounded by grid points \mathbf{p}_{abc} with $a, b, c \in \{0, 1\}$ as shown in Figure 3.3. Furthermore, let \mathbf{p}_{000} have components (x_0, y_0, z_0) .
3. $x = \frac{(p_x - x_0)}{g}$, $y = \frac{(p_y - y_0)}{g}$, $z = \frac{(p_z - z_0)}{g}$
4. $\phi_{abc} = \phi(\mathbf{p}_{abc})$ for convenience in notation.

Using trilinear interpolation to find $\phi(\mathbf{p})$,

$$\phi(\mathbf{p}) = \sum_{a=0}^1 \sum_{b=0}^1 \sum_{c=0}^1 \phi_{abc} [(1-a)(1-x)+ax][(1-b)(1-y)+by][(1-c)(1-z)+cz] \quad (3.1)$$

The gradient of the level set function $\nabla\phi(\mathbf{p})$, using trilinear interpolation, is

$$\nabla\phi(\mathbf{p}) = \begin{pmatrix} \sum_{a=0}^1 \sum_{b=0}^1 \sum_{c=0}^1 \phi_{abc} (2a-1) [(1-b)(1-y)+by][(1-c)(1-z)+cz] \\ \sum_{a=0}^1 \sum_{b=0}^1 \sum_{c=0}^1 \phi_{abc} [(1-a)(1-x)+ax] (2b-1) [(1-c)(1-z)+cz] \\ \sum_{a=0}^1 \sum_{b=0}^1 \sum_{c=0}^1 \phi_{abc} [(1-a)(1-x)+ax][(1-b)(1-y)+by] (2c-1) \end{pmatrix} \quad (3.2)$$

Note that the interpolation functions to find $\phi(\mathbf{p})$ and $\nabla\phi(\mathbf{p})$ are not functions of grid size. Therefore, the time complexity of these calculations are constant; they do not increase if ϕ is refined to a finer grid.

Inertial properties

The inertial properties, i.e., mass, center of mass, and moment of inertia, of a given grain must be known for its use in LS-DEM. These quantities are computed directly from the grain's level set function. Defining the smoothed Heaviside function $H(\phi)$ as

$$H(\phi) = \begin{cases} 0 & \text{if } \phi < -\epsilon \\ \frac{1}{2}\left(1 + \frac{\phi}{\epsilon} + \frac{\sin(\frac{\pi\phi}{\epsilon})}{\pi}\right) & \text{if } -\epsilon < \phi < \epsilon \\ 1 & \text{if } \phi > \epsilon \end{cases} \quad (3.3)$$

where ϵ is a smoothness parameter. $\epsilon = 1.5$ was used in this study. The mass of a grain of uniform density ρ and grid spacing g represented by level set function ϕ is

$$m = \rho g^3 \sum_{i=1}^I \sum_{j=1}^J \sum_{k=1}^K H(-\phi(x_i, y_j, z_k)) \quad (3.4)$$

where $\phi(x_i, y_j, z_k)$ is the value of ϕ at grid point (x_i, y_j, z_k) , and I , J , and K are the number of grid points in the x , y , and z directions, respectively, of ϕ . In other words, the mass is proportional to the summation of $H(-\phi)$ over every grid point of ϕ . The components of its center of mass are

$$\begin{aligned} c_x &= \frac{\rho g^3}{m} \sum_{i=1}^I \sum_{j=1}^J \sum_{k=1}^K H(-\phi(x_i, y_j, z_k)) x_i \\ c_y &= \frac{\rho g^3}{m} \sum_{i=1}^I \sum_{j=1}^J \sum_{k=1}^K H(-\phi(x_i, y_j, z_k)) y_j \\ c_z &= \frac{\rho g^3}{m} \sum_{i=1}^I \sum_{j=1}^J \sum_{k=1}^K H(-\phi(x_i, y_j, z_k)) z_k \end{aligned} \quad (3.5)$$

Finally, the components of its moment of inertia are

$$\begin{aligned}
I_{11} &= \rho g^3 \sum_{i=1}^I \sum_{j=1}^J \sum_{k=1}^K H(-\phi(x_i, y_j, z_k)) [(y_j - c_y)^2 + (z_k - c_z)^2] \\
I_{22} &= \rho g^3 \sum_{i=1}^I \sum_{j=1}^J \sum_{k=1}^K H(-\phi(x_i, y_j, z_k)) [(x_i - c_x)^2 + (z_k - c_z)^2] \\
I_{33} &= \rho g^3 \sum_{i=1}^I \sum_{j=1}^J \sum_{k=1}^K H(-\phi(x_i, y_j, z_k)) [(x_i - c_x)^2 + (y_j - c_y)^2] \\
I_{23} = I_{32} &= -\rho g^3 \sum_{i=1}^I \sum_{j=1}^J \sum_{k=1}^K H(-\phi(x_i, y_j, z_k)) (y_j - c_y)(z_k - c_z) \\
I_{13} = I_{31} &= -\rho g^3 \sum_{i=1}^I \sum_{j=1}^J \sum_{k=1}^K H(-\phi(x_i, y_j, z_k)) (x_i - c_x)(z_k - c_z) \\
I_{12} = I_{21} &= -\rho g^3 \sum_{i=1}^I \sum_{j=1}^J \sum_{k=1}^K H(-\phi(x_i, y_j, z_k)) (x_i - c_x)(y_j - c_y)
\end{aligned} \tag{3.6}$$

Boundary node discretization

LS-DEM uses a node-to-surface contact algorithm that is utilized in finite element models (Laursen 2002) as well as discrete element models (Lim, Krabbenhoft, and Andrade 2014) for the handling of nonconvex particles with multiple contact points as well as computational ease, whereby nodes are seeded onto the surface $\partial\Omega$ of each particle (Figure 3.4). The density of nodes on a given particle is a matter of choice and has implications on particle behavior; however, we find that seeding with a maximum node-to-node spacing of less than $d/10$, where d is the particle diameter, is adequate to capture particle morphology as higher nodal densities have a negligible impact on behavior. Contact is then determined by checking each node of a master particle against the boundary of a slave particle for penetration. Because each node is checked for contact, the computational cost of contact is proportional to the number of nodes seeded onto the master particle.

Note that the number of nodes seeded onto a particle does not change its underlying geometry, which is defined by its level set function, unlike polyhedra and clumping methods where changing the number of vertices or spheres completely modifies their geometries. Thus, more advanced schemes such as adaptive seeding near areas of contact during time integration are possible if such precision is desired.

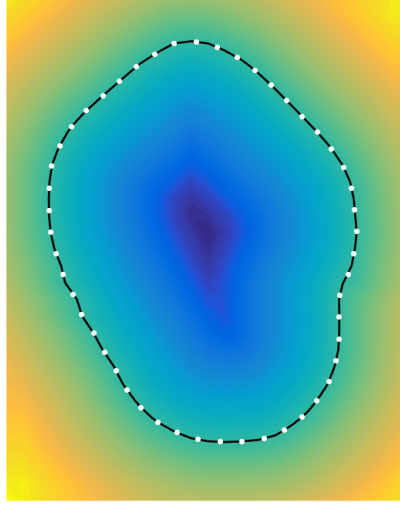


Figure 3.4: Example of boundary node discretization with nodes in white seeded on the grain surface. This is shown in 2D for illustrative purposes only.

Contact

As mentioned in the previous section, contact in LS-DEM is handled through a node-to-surface contact algorithm. Let grain i have nodes \mathbf{m}_a^i with $\{a \in \mathbb{Z} \mid 1 \leq a \leq A\}$, where A is the number of nodes seeded onto i . Contact is determined between master grain i and slave grain j by checking all nodes \mathbf{m}_a^i of grain i with the level set function ϕ^j of grain j . Then,

$$d_a^{j,i} = \phi^j(\mathbf{m}_a^i) \quad (3.7)$$

$$\hat{\mathbf{n}}_a^{j,i} = \frac{\nabla \phi^j(\mathbf{m}_a^i)}{\|\nabla \phi^j(\mathbf{m}_a^i)\|} \quad (3.8)$$

where $d_n^{j,i}$ and $\hat{\mathbf{n}}_a^{j,i}$ are the penetration distance and outward contact normal of j , respectively, between grains i and j at node \mathbf{m}_a^i (see Figure 3.5). These contact equations are very simple and easy to compute due to the formulation of the level set function, whose value at any point represents the distance from that point to the surface, and its gradient at any point represents, in principle, the unit outward normal at that point. However, due to the level set function's discrete nature, the magnitude of $\nabla \phi^j(\mathbf{m}_a^i)$ is very close, but not equal, to unity and therefore is normalized.

If at least one node \mathbf{m}_a^i of master grain i is penetrating slave grain j , that is, if $\exists \mathbf{m}_a^i \mid \phi^j(\mathbf{m}_a^i) < 0$, then we consider the two grains to be in contact, and thus, interparticle forces must be computed.

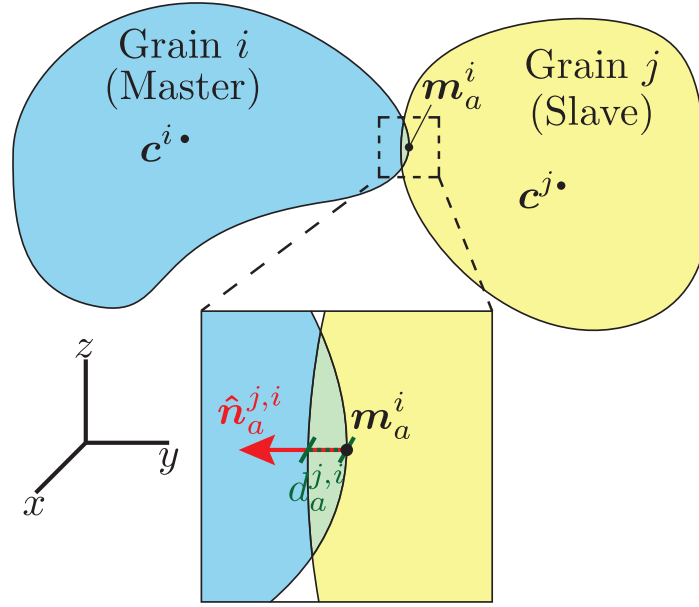


Figure 3.5: Illustration of two contacting grains.

Forces and moments

To compute forces from penetrations, any contact model can be used, but we used a linear elastic contact model for the purposes of this study. Thus, the contact normal force contribution from node \mathbf{m}_a^i on grain i is

$$\mathbf{F}_{n,a}^i = \begin{cases} -k_n d_a^{j,i} \hat{\mathbf{n}}_a^{j,i} & \text{if } d_a^{j,i} < 0 \\ \mathbf{0} & \text{else} \end{cases} \quad (3.9)$$

where k_n is the normal contact stiffness. By action and reaction, the contribution of contact normal force $\mathbf{F}_{n,a}^j$ from node \mathbf{m}_a^i on grain j is

$$\mathbf{F}_{n,a}^j = -\mathbf{F}_{n,a}^i \quad (3.10)$$

The moment $\mathbf{M}_{n,a}^i$ contributed by the contact normal force $\mathbf{F}_{n,a}^i$ at node \mathbf{m}_a^i on grain i is

$$\mathbf{M}_{n,a}^i = (\mathbf{m}_a^i - \mathbf{c}^i) \times \mathbf{F}_{n,a}^i \quad (3.11)$$

where \mathbf{c}^i is the centroid of grain i . Similarly, the moment $\mathbf{M}_{n,a}^j$ contributed by the contact normal force at node \mathbf{m}_a^i on grain j is

$$\mathbf{M}_{n,a}^j = (\mathbf{m}_a^i - \mathbf{c}^j) \times \mathbf{F}_{n,a}^j \quad (3.12)$$

where \mathbf{c}^j is the centroid of grain j .

For the calculation of frictional forces, LS-DEM uses a Coulomb friction model similar to those in Andrade et al. 2012b and Cundall and Strack 1979. For a given node \mathbf{m}_a^i , frictional forces (and related moments) only exist if $\mathbf{F}_{n,a}^i \neq \mathbf{0}$. The relative velocity \mathbf{v}_a of node \mathbf{m}_a^i to grain j is

$$\mathbf{v}_a = \mathbf{v}^i + \boldsymbol{\omega}^i \times (\mathbf{m}_a^i - \mathbf{c}^i) - \mathbf{v}^j - \boldsymbol{\omega}^j \times (\mathbf{m}_a^i - \mathbf{c}^j) \quad (3.13)$$

where \mathbf{v}^i , \mathbf{v}^j , $\boldsymbol{\omega}^i$, and $\boldsymbol{\omega}^j$ are the translational and angular velocities of grains i and j . The incremental shear displacement $\Delta \mathbf{s}_a$ is then

$$\Delta \mathbf{s}_a = [\mathbf{v}_a - (\mathbf{v}_a \cdot \hat{\mathbf{n}}_a^{j,i}) \hat{\mathbf{n}}_a^{j,i}] \Delta t \quad (3.14)$$

The shear force $\mathbf{F}_{s,a}^i$ on grain i contributed by node \mathbf{m}_a^i is updated as such:

$$\mathbf{F}_{s,a}^i \leftarrow \mathbf{Z} \mathbf{F}_{s,a}^i - k_s \Delta \mathbf{s}_a \quad (3.15)$$

where \mathbf{Z} is the rotation matrix that rotates the normal vector $\hat{\mathbf{n}}_a^{j,i}$ at the current timestep to the normal vector at the previous timestep and k_s is the shear contact stiffness. The Coulomb friction law dictates $\mathbf{F}_{s,a}^i$ be capped at a fraction of the normal force $\mathbf{F}_{n,a}^i$:

$$\mathbf{F}_{s,a}^i \leftarrow \frac{\mathbf{F}_{s,a}^i}{\|\mathbf{F}_{s,a}^i\|} \min(\|\mathbf{F}_{s,a}^i\|, \mu \|\mathbf{F}_{n,a}^i\|) \quad (3.16)$$

where μ is the interparticle friction coefficient. By action and reaction,

$$\mathbf{F}_{s,a}^j = -\mathbf{F}_{s,a}^i \quad (3.17)$$

The moment $\mathbf{M}_{s,a}^i$ contributed by node \mathbf{m}_a^i 's shear force on grain i is

$$\mathbf{M}_{s,a}^i = (\mathbf{m}_a^i - \mathbf{c}^i) \times \mathbf{F}_{s,a}^i \quad (3.18)$$

Similarly, the the moment $\mathbf{M}_{s,a}^j$ contributed by node \mathbf{m}_a^i 's shear force on grain j is

$$\mathbf{M}_{s,a}^j = (\mathbf{m}_a^i - \mathbf{c}^j) \times \mathbf{F}_{s,a}^j \quad (3.19)$$

The total contact force on grain i is found by summing all nodal contact forces:

$$\mathbf{F}_{tot}^i = \sum_{a=1}^A (\mathbf{F}_{n,a}^i + \mathbf{F}_{s,a}^i) \quad (3.20)$$

By action and reaction,

$$\mathbf{F}_{tot}^j = -\mathbf{F}_{tot}^i \quad (3.21)$$

The total contact moment on each grain is found by summing all nodal contact moments:

$$\mathbf{M}_{tot}^i = \sum_{a=1}^A (\mathbf{M}_{n,a}^i + \mathbf{M}_{s,a}^i) \quad (3.22)$$

$$\mathbf{M}_{tot}^j = \sum_{a=1}^A (\mathbf{M}_{n,a}^j + \mathbf{M}_{s,a}^j) \quad (3.23)$$

Motion

Given a grain's inertial properties and the force and moment on it, the translational velocity, angular velocity, position, and rotation of the grain are updated using an appropriate time integration scheme. In this chapter, the scheme described in Lim and Andrade 2014 and Walton and Braun 1993 was used to update the positions of the center of mass and nodes of each grain. This scheme solves Newton's and Euler's governing equations of motion

$$\mathbf{F} = m\mathbf{a} + m\xi\mathbf{v} \quad (3.24)$$

$$M_1 = I_1\alpha_1 - \omega_2\omega_3(I_2 - I_3) + \xi I_1\omega_1 \quad (3.25)$$

$$M_2 = I_2\alpha_2 - \omega_1\omega_3(I_2 - I_3) + \xi I_2\omega_2 \quad (3.26)$$

$$M_3 = I_3\alpha_3 - \omega_1\omega_2(I_2 - I_3) + \xi I_3\omega_3 \quad (3.27)$$

where \mathbf{F} is the total force on a particle, m is its mass, ξ is a damping parameter, \mathbf{v} is its velocity, $i = 1,2,3$ are the three principal directions such that the particle's moment of inertia \mathbf{I} is diagonal, and w_i is its angular velocity. These equations of motions are solved via an explicit time integration algorithm with a predictor-corrector algorithm to update the rotational kinematics as those equations are nonlinear.

It is important to note that, to minimize computational cost, the level set function of each grain is never updated as it moves; each level set function remains in a reference configuration. To accommodate this, when computing contact, the nodes \mathbf{m}_a^i of grain i (in the global frame) are moved temporarily into the reference configuration of grain j 's level set function. From there, contact forces and moments are found (in the reference configuration of grain j) and then moved back to the global frame.

3.2 Case study: Triaxial compression test

We test the validity of LS-DEM by simulating a triaxial compression (TXC) test using XRCT data taken from two real TXC experiments on a Martian regolith-like sand. Our goal is to capture, through LS-DEM, both the axial stress-axial strain and volumetric strain-axial strain relations measured in the experiment. We calibrate the parameters of the LS-DEM model to replicate the results of one experiment, then use those parameters to predict the behavior of the other experiment.

The experiment

Two cylindrical specimens, each 11 mm in diameter and 24 mm in height, of a Martian regolith-like sand are compressed isotropically to 100 kPa, then triaxially compressed at an axial strain rate of $\dot{\epsilon}_1 = 0.1\%/s$ and a constant radial pressure of $\sigma_3 = 100$ kPa. 3DXRCT images with voxel edge length $31.1 \mu\text{m}$ were taken of each specimen at the onset of axial strain. The stress-strain and volume-strain relations are plotted in Figure 3.6; the difference in behavior of the two specimens is attributed to the difference in the number of grains and therefore initial porosity of the two specimens; the looser specimen has 2,773 grains and an initial porosity of 41%, while the denser specimen has 3,158 grains and an initial porosity of 36%.

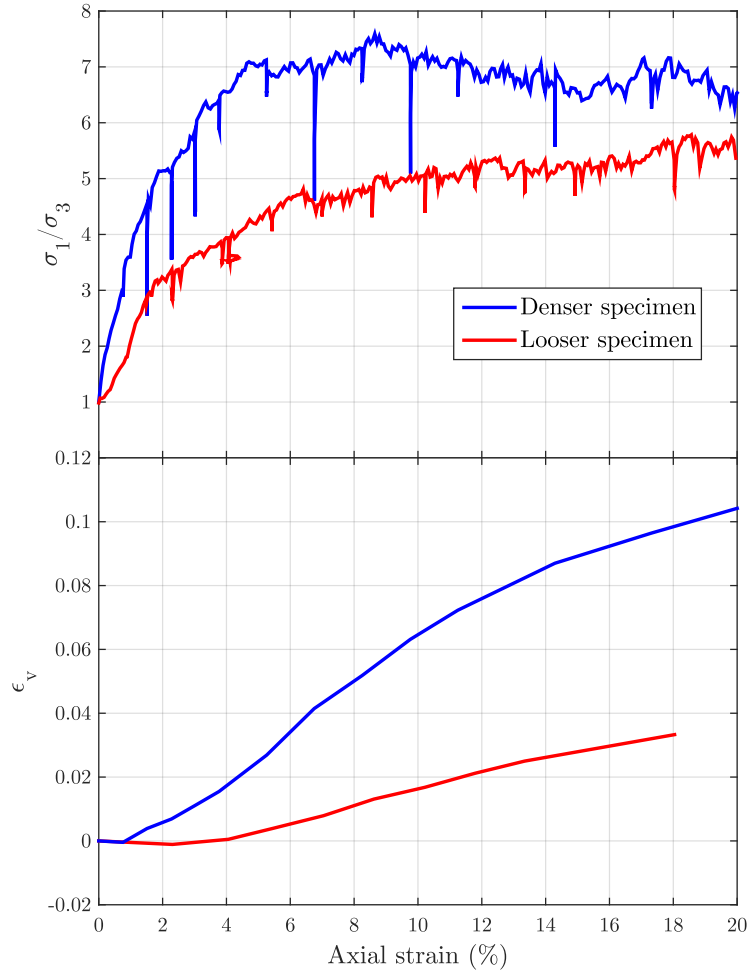


Figure 3.6: Stress-strain and volume-strain results of experiments. Note: experimental volume-strain data for the looser specimen was stopped at 18%.

LS-DEM calibration of looser specimen

We apply the characterization technique described in Vlahinic et al. 2013 to produce level set functions of every grain from the XRCT image of the looser specimen at the onset of triaxial compression. In other words, we generate a virtual specimen where each grain is represented 1:1 in both shape and position (Figure 3.7). Our goal is to calibrate the values of the interparticle normal stiffness k_n and interparticle friction μ in an LS-DEM simulation to match experimental results. Grain density is set at 2500 kg/m^3 and shear stiffness k_s is held at $0.9k_n$. While we are not able to reproduce the $\dot{\epsilon}_1 = 0.1\%/s$ strain rate of the experiment due to computational limitations, as such a low strain rate would take prohibitively long to simulate, values of $\dot{\epsilon}_1$, global damping, and Δt are chosen to maintain quasi-static conditions, numerical stability, and computational tractability (Tu and Andrade 2008). Rigid, frictionless walls

were used and wall stiffness are set to be the same as grain stiffness k_n . We apply isotropic compression to the virtual specimen to a pressure of 100 kPa, then axially compress the assembly to $\epsilon_1 = 20\%$ while maintaining radial pressure $\sigma_3 = 100$ kPa, the final configuration of which is shown in Figure 3.7. The stress-strain and volume-strain relations are plotted in Figure 3.8 with three different values each of k_n and μ .

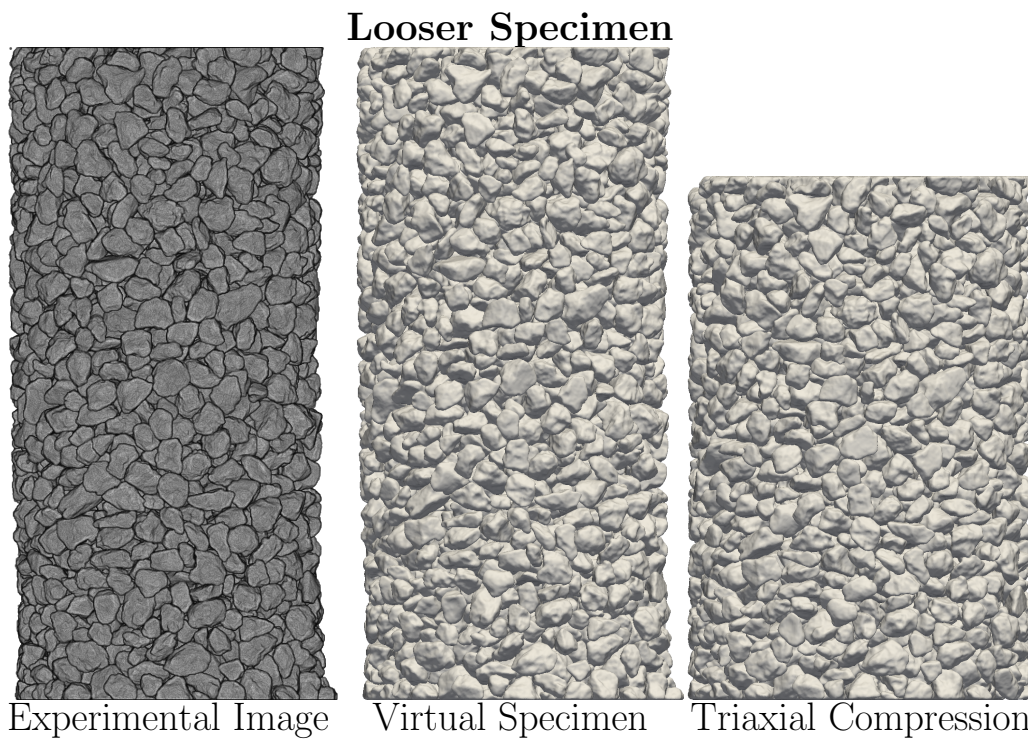


Figure 3.7: Left: 3D rendering of XRCT image of uncompressed looser specimen. Center: Virtual level set function representation of looser specimen. Right: Virtual specimen after triaxial compression.

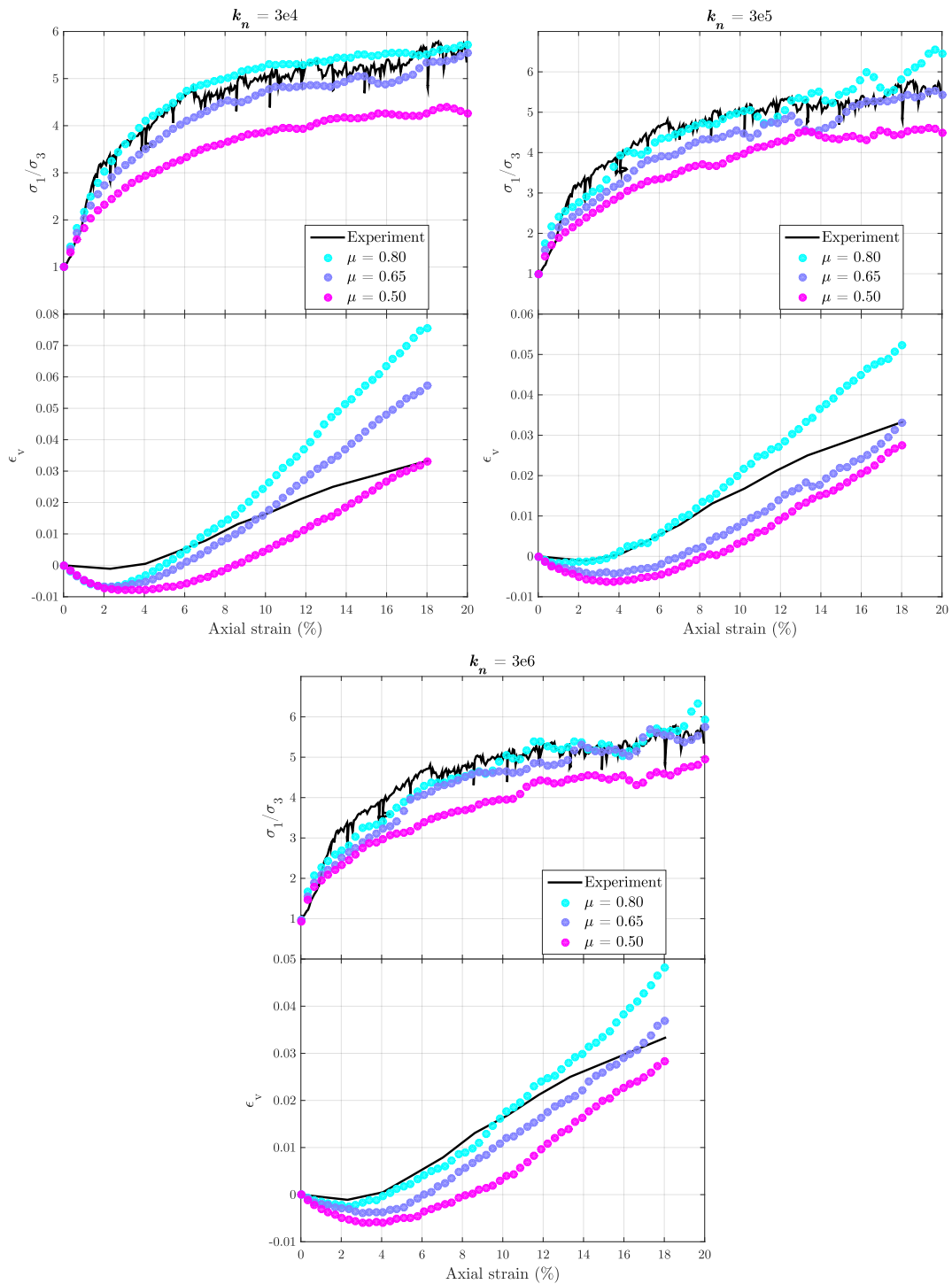


Figure 3.8: Stress-strain and volume-strain relations for LS-DEM simulations on looser specimen. The values $k_n = 3 \times 10^6$ and $\mu = 0.65$ are chosen as best-fit parameters.

From Figure 3.8, the values of k_n and μ that result in the closest match in both

stress-strain and volume-strain behavior are 3×10^6 N/m and 0.65, respectively. The contact stiffness k_n overall does not have a particularly large effect on the behavior of the specimen, and a value of 3×10^6 N/m seems reasonable especially in the context of DEM. As for the interparticle friction coefficient μ , while there is a wealth of experimental data on macroscopic rock friction at high pressures (Byerlee 1978; Hoskins, Jaeger, and Rosengren 1968), there is not much research at the low pressures and small length scales in the regime of this case study. Grain-scale experiments performed on quartz, a relatively “smooth” particle, have found an interparticle friction coefficient of about 0.24 (Senetakis, Coop, and Todisco 2013). While an interparticle coefficient of friction of 0.65 seems quite high in that context, the sand used in this case study’s experiment consist of unweathered rock fragments meant to mimic those of Mars. It is therefore not unreasonable that the grains have a high amount of surface roughness unable to be captured by the resolution of the XRCT image, which manifests itself in a high coefficient of interparticle friction, especially at low pressures where friction is highly dependent on surface roughness (Byerlee 1978).

LS-DEM simulation of denser specimen

We now seek to predict the experimental results of the denser specimen by using the calibrated values obtained from simulations on the looser specimen to simulate the denser specimen. The characterization process is repeated: from its XRCT image, we generate a virtual specimen of the denser specimen (Figure 3.9). We then repeat the LS-DEM process of isotropic compression and triaxial compression with the calibrated values of $k_n = 3 \times 10^6$, $\mu = 0.65$ and all other parameters the same as before.

As Figure 3.10 of the stress-strain and volume-strain relations indicates, using the calibrated parameters gives a reasonable prediction of the behavior of the denser specimen (right), but it is not as accurate as the results from the looser specimen with which we use to calibrate (left).

3.3 Discussion

In terms of assessing the validity of our LS-DEM model, further investigation can be done. First, we can check if indeed the calibrated parameters k_n and μ are reasonable by performing experiments on individual grains of the specimens using apparatuses and procedures in Cil and Alshibli 2014b and Senetakis, Coop, and Todisco 2013 to compute k_n and μ , respectively. Second, while slight bulging is

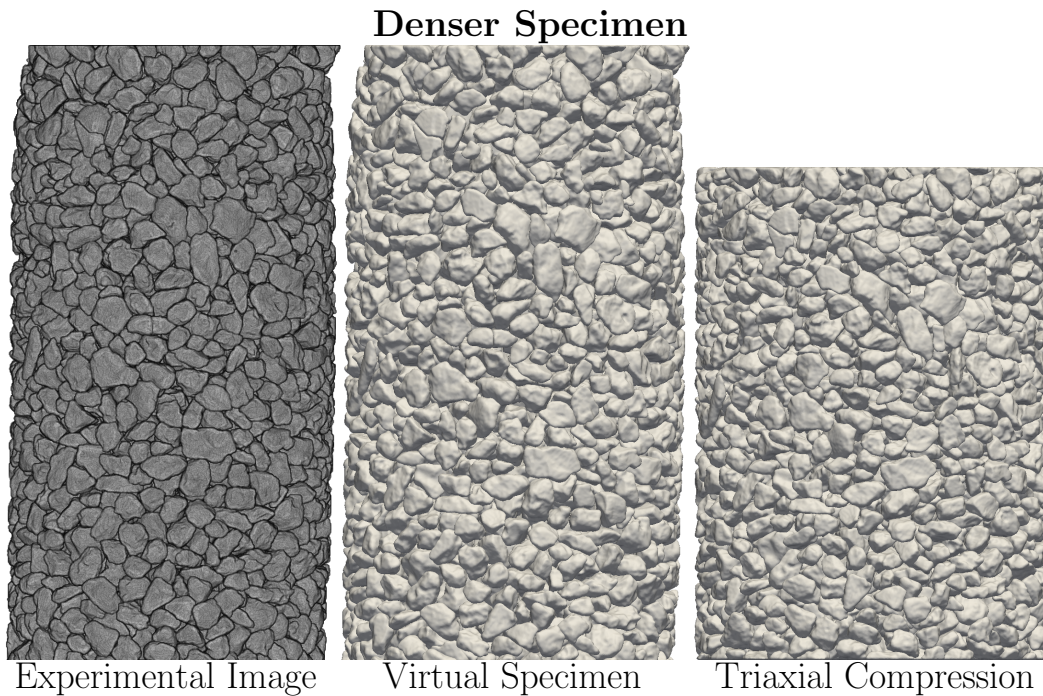


Figure 3.9: Left: 3D rendering of XRCT image of uncompressed denser specimen. Center: Virtual level set function representation of denser specimen. Right: Virtual specimen after triaxial compression.

seen in the experimental specimens, in our simulations, we use rigid, straight walls, which prevent bulging from happening computationally. It would be interesting to see if the implementation of a flexible membrane instead of rigid walls in our simulations could improve results. Finally, the Coulomb friction model used was the most simple of various friction models; more complex models invoke the rate of slip rather than just the amount of slip (note that while macroscopic loading is quasistatic, particle-to-particle interactions may not be and thus subject to rate-based friction) as well other state variables (Dieterich 1979; Ruina 1983). Other models have expanded on on these “rate and state” models to incorporate concepts of viscoplasticity (Perfettini and Molinari 2017) and atomistic considerations (Hatano 2015). Incorporating such friction laws may lead to improved results.

The shape-based nature of LS-DEM makes it rife with possibilities in studying the mechanical properties of granular assemblies. One area that looks promising is grain breakage and comminution. Experiments and computations of grain breakage at the grain-scale have been performed (Cil and Alshibli 2012; Cil and Alshibli 2014b; Parab et al. 2014), some of which were also investigated using DEM. Determining fracture criteria (a function of contact forces (Jaeger 1967), coordination

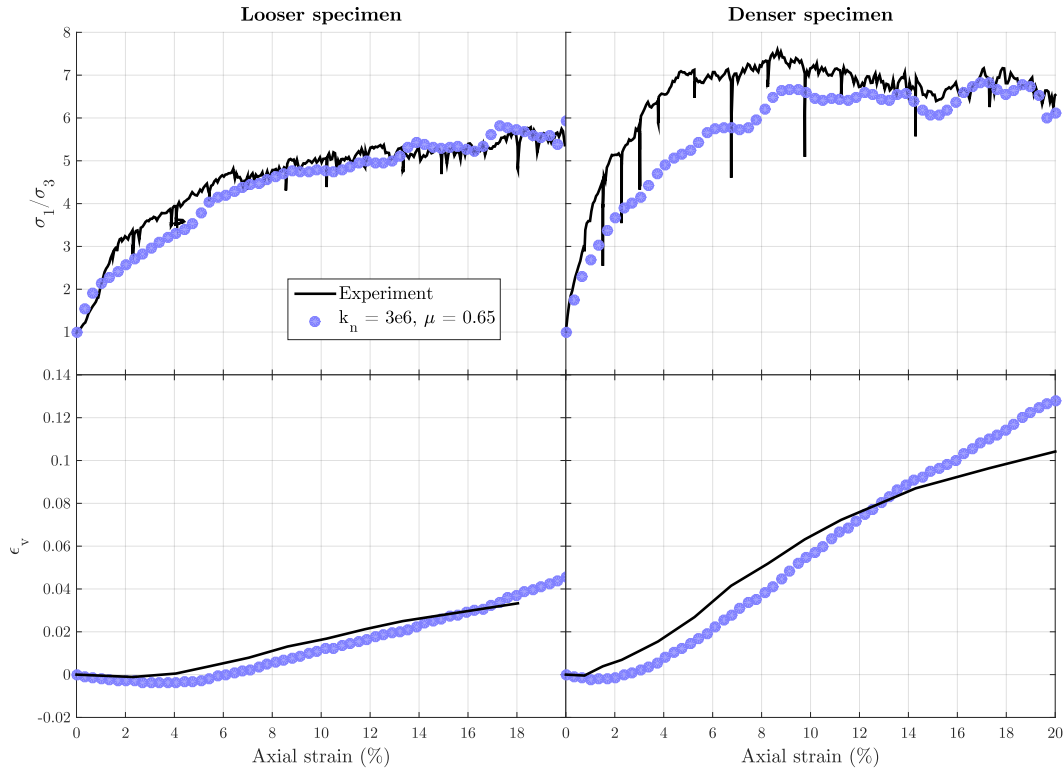


Figure 3.10: Stress-strain and volume-strain relations for LS-DEM simulations on looser (left) and denser (right) specimens with $k_n = 3 \times 10^6$ and $\mu = 0.65$.

number (Casini, Viggiani, and Springman 2013; Sammis, King, and Biegel 1987), and probability (Weibull 1939; Weibull 1951)) and direction of fracture planes (a function of Mohr-Coulomb failure surfaces (Shen, Stephansson, and Rinne 2014) and location of contact forces) for grains of arbitrary morphology are not a trivial tasks. However, once fracture criteria and fracture planes have been determined, the level set framework is convenient for modeling grain breakage as fracture planes can be represented by level set functions which then can be used to split a grain using binary operations between the level set function of the grain and the level set functions of the fracture planes, which would allow replications of exact fracture patterns that occur in experiments. Another area in which LS-DEM could be applied is in multiscale methods, such as the one developed and implemented in (Andrade et al. 2010; Lim et al. 2015), or using LS-DEM to infer continuum quantities such as dilatancy and macroscopic friction angle to shed light on how these continuum properties originate from the grain scale. Essentially, the potential applications of LS-DEM fall under the same umbrella as those of classic DEM, but with its ability to capture shape, LS-DEM will hopefully enable us to arrive at a deeper, more

quantitative understanding of the behavior of granular materials.

There are also possible extensions and studies of LS-DEM in the computational realm. The computational time complexity of LS-DEM does not scale with increased grid resolution and is relatively low compared to that of polyhedral or NURBS-based methods as contact detection does not require traversal a tree of bounding volumes (Ericson 2004; Lim and Andrade 2014) but rather is constant and only requires a lookup of values at grid points. In this sense, level set functions work essentially as lookup tables of penetration distances and contact normals where values between grid points are estimates found via interpolation. Two interesting questions arise as a result of this. First, how does grid fineness relate to accuracy? In this study, grid fineness was held constant as the grains' level set functions resided on grids at the same resolution as the XRCT images themselves. Second, what effect does memory consumption have on the computational cost and limitations of LS-DEM? Because LS-DEM requires an underlying grid with a value of ϕ at every grid point, it consumes a large amount of memory. A $40 \times 40 \times 40$ level set function requires 64,000 values to be stored, while a NURBS curve with 20 knots in each direction or a polyhedra with 400 vertices requires only 1,200 values to be stored, which is a memory consumption of less than 2% than that of the aforementioned level set function's memory footprint. Even though LS-DEM's contact algorithm has constant time complexity with respect to grid resolution, a large memory footprint nonetheless may lead to increased computation time due to cache misses. It could even lead to crashes if memory overflows, limiting the amount of grains that can be simulated. However, many clusters today have large amounts of memory; the cluster on which our LS-DEM simulations were run has 48 gigabytes of RAM per processor, and the memory consumption of the entire simulation was around 1 gigabyte, which means that, only taking into account memory constraints, it would have been possible to run a simulation containing upwards of 140,000 grains. Furthermore, techniques to reduce the amount of memory used by the level set functions are possible, such as storing their values as floats instead of doubles and/or removing values either outside or very deep inside the particles by storing the level set functions in trees instead of on grids, but these techniques may affect accuracy or computational cost and remain areas to be researched.

3.4 Conclusion

Along with factors such as friction and void ratio, grain shape is an important factor that affects nearly every macroscopic quantity (Cho, Dodds, and Santamarina

2006) of granular systems. We have presented a method, LS-DEM, to simulate systems of arbitrarily-shaped particles that can directly use outputs of level set-based characterization methods as its geometric basis. Furthermore, we have applied LS-DEM to two full virtual triaxial specimens with particle morphology coming directly from XRCT images of real experiments, being able to capture quantitatively, through LS-DEM, both the stress-strain and volume-strain relations observed in the experiments. By calibrating the parameters of our model to match the results of one experiment, we formulated a prediction of the behavior of the second experiment. Finally, we have highlighted some areas in which LS-DEM can be further explored, in mechanical, computational, and algorithmic respects.

*Chapter 4***ANALYSIS OF SHEAR BANDING OF GRANULAR MATERIALS IN TRIAXIAL COMPRESSION USING LS-DEM**

The material in this chapter is adapted from:

Kawamoto, Reid, Edward Andò, Gioacchino Viggiani, and José E. Andrade. “All you need is shape: predicting shear banding in sand with LS-DEM”. In: *Journal of the Mechanics and Physics of Solids* 111 (Supplement C) 375–392.

doi:<https://doi.org/10.1016/j.jmps.2017.10.003>

Despite its familiarity as an everyday material, the mechanical behavior of sand is complex. Sand can be modeled either as a continuous medium responding to Cauchy stress or as an assembly of individual particles following Newton’s laws. Continuum models of sand (MiDi 2004; Schofield and Wroth 1968) are in demand to analyze field problems, and by their very nature they ignore particles and make use of such abstract concepts as stress and strain. In general, these models work acceptably; however, they fare less well in the commonplace yet complex scenario where strain is localized in regions so small that the granular structure cannot safely be ignored (e.g., landslides, hourglass orifice flow). Models such as micropolar theory (Kafadar and Eringen 1971) inherently possess a length scale that allow them to capture strain localization such as shear banding (Mühlhaus and Vardoulakis 1987); however, studies have been limited to 2D conditions (Ebrahimian, Noorzad, and Alsaleh 2012; Tejchman 2008) and many of their parameters’ physical interpretations are not known and must be back-calculated from experimental data (Ehlers and Scholz 2007). Thus, in order to handle 3D strain localization problems, it is generally agreed that an explicit modeling of the particle scale is needed.

As an alternative to continuum modeling, the discrete element method (DEM), directly simulates the interactions between thousands of spherical particles with physical, well-understood parameters such as particle size, stiffness, and coefficient of friction (Cundall and Strack 1979); however, DEM does not adequately reproduce the bulk behavior due to its poor representation of reality as sand particles (and many other types of particles!) are far from spherical. DEM’s lack of ability to capture particle shape has spurred the development of variants able to capture particle shape, ranging from sphere clumping (Garcia et al. 2009) to polyhedra (Cundall

1988) to ellipsoids (Rothenburg and Bathurst 1991; Yan, Regueiro, and Sture 2010) to NURBS (Lim and Andrade 2014). While clumping and polyhedra-based methods can approximate the volume and general shape of sand particles, it has been shown experimentally and computationally that not only do the overall shape of particles (“sphericity”) affect bulk granular behavior, but surface curvature at a lower, local scale (“roundness”) also affects behavior (Cho, Dodds, and Santamarina 2006; Jerves, Kawamoto, and Andrade 2016). Unfortunately, clumping methods usually underestimate and polyhedra methods overestimate roundness unless a very large number of spheres or vertices are used (Gao et al. 2012); however, “a 3D DEM simulation using a statistically valid number of clumps to faithfully simulate a real soil problem is still somewhat unrealistic” (Zheng and Hryciw 2017). Ellipsoid-based particles usually overestimate roundness and are inherently convex. Although clumping, polyhedra, and ellipsoid methods have had modest success in replicating experimental results at the bulk scale (Li et al. 2017; Lee, Hashash, and Nezami 2012; Ting et al. 1993), they have not been compared to experimental results at lower length scales, such as that of strain localization. NURBS-based methods accurately capture particle shape at both length scales and can accurately simulate granular behavior in shear bands, but are computationally time-expensive and have only been able to simulate unit cells of about one thousand particles at most (Lim et al. 2015). One method of overcoming these impediments in both continuum and discrete modeling is the avatar paradigm, able to both characterize and simulate the behavior of granular assemblies through a DEM framework. This characterizes particle shapes (“avatars”) directly from experimental images, can simulate laboratory-scale amounts of particles (over 50,000), and captures the same 3D strain localization trends seen in experiments.

The avatar paradigm is also significant in that it helps to close the gap between experiments and simulations of granular materials. Of the research that exists in investigating granular materials at the particle scale, there are broadly two camps: those who seek to characterize granular assemblies, often through experiments involving X-ray computed tomographic (XRCT) scans or photoelastic discs, and those who seek to simulate granular behavior, typically through DEM, with unfortunately little integration and validation between the two camps. In recent years, an overarching characterization and simulation framework, the avatar paradigm, has been developed. It consists of two parts: one, level set imaging (LS-Imaging) (Vlahinic et al. 2013), which characterizes granular assemblies from XRCT images into avatars, or mathematical representations of individual particles within the assemblies, and

two, the level set discrete element method (LS-DEM) (Kawamoto et al. 2016), a DEM variant which can take avatars from LS-Imaging as an input and simulates their mechanical behavior.

LS-Imaging is the cutting edge in high-fidelity particle-scale characterization. Characterization of granular materials has come a long way since the days of “destructive” methods, which involved dismantling experimental specimens to measure particle-scale quantities (Oda 1972), and 3D XRCT scans and other methods of digital imaging of experiments are now the norm in experimental particle-scale mechanics (Rechenmacher and Finno 2004; Andò 2013). Increases in image fidelity and resolution have led to the current state of the art characterization approach of LS-Imaging, which invokes the use of LS methods to extract surfaces of individual particles (“avatars”) from XRCT images (Gao and Chae 2008; Li et al. 2010; Vlahinic et al. 2013).

Although characterization techniques such as the aforementioned LS-Imaging have seen tremendous progress, they lack the ability to probe one crucial aspect of granular materials: interparticle contact forces. The stress-force-fabric relationship derived from interparticle contact forces (Rothenburg and Bathurst 1989) has been shown to be one of the key ingredients in the description of constitutive models for granular materials. Therefore, a micromechanical model such as DEM (Cundall and Strack 1979) remains a necessary component for the inference of contact forces and related quantities. LS-DEM is one such model that is able to handle real, complex particle morphologies, which then enabled reproduction and prediction of the bulk behavior of small experimental specimens consisting of about 3,000 particles each (Kawamoto et al. 2016).

In this study, the avatar paradigm is built upon and used to characterize and simulate the behavior of a complete and much larger experimental specimen of natural sand, this time consisting of over 53,000 particles, reproducing the behavior of the experiment across three scales: macroscopic, local, and particle level. At the macroscopic level, the simulations using LS-DEM capture very closely the macroscopic stress-strain curve and the dilatancy-strain curve. These results have been obtained before using continuum models and well-calibrated DEM models such as those of Sun and Xiao 2017 and Lee, Hashash, and Nezami 2012. However, in this study, the results are able to go to deeper levels of prediction, which have not been attained before. For example, at the local level, the simulations show striking similarity with shear strain levels in the shear band and other parts of the specimen. Furthermore, the

model is able to predict the shear band orientation, inclination and thickness. This is something where both continuum and discrete models have struggled in the past. Finally, at the particle level, the model predicts particle rotations that on average compare well with those obtained in the experiment. Well beyond reproduction, the avatar paradigm affords the ability to see the evolution of interparticle forces, which are currently impossible to obtain from regular experiments, and which are an active area of research for single-crystal spherical particles (Hurley et al. 2016). Two modeling advancements afford the avatar paradigm higher fidelity: shape and more accurate boundary conditions. We present a model to replicate the boundary conditions of triaxial experiments. In particular, the deformability of the rubber membrane confining the specimen is modeled, as well as the displacement and rotation of the loading platen. Results show that these features are necessary to capture the evolution observed in the experiment, especially the onset and evolution of shear banding. By analyzing the kinematics and interparticle forces in the shear band, insights are gained regarding its formation, positioning, and evolution.

4.1 The experiment: triaxial compression test and imaging of specimen

The experiment considered herein is a triaxial compression test on a small specimen of HN31 Hostun sand, which is performed within an X-ray scanner. The results of this test have appeared previously in (Andò et al. 2012b) and are summarized here; more details can be found in (Andò 2013). The triaxial apparatus is much smaller than those used in conventional soil mechanics testing, and the specimen itself measures only 11 mm in diameter and 22 mm in height. This is because of constraints of the field of view of the XRCT imaging equipment, which is chosen to be able to adequately capture the features of individual particles, which in turn limits the specimen size. Nevertheless, the size of the sample is large enough to be representative of a continuum response of the material, displaying classic features such as stress-strain and volumetric responses observed in triaxial tests on standard-sized specimens, as well as the appearance of shear banding. Figure 4.1 shows XRCT image slices of the specimen.

Hostun HN31 has $D_{50} = 338 \mu\text{m}$, and poor grading. Particles are angular and non-spherical, especially compared to other ‘standard’ sands used in geomechanics research, such as Toyoura and Ottawa sand. Hostun sand is chosen for its particularly challenging particle shapes to showcase the ability of LS-DEM to simulate particles of arbitrary shape.

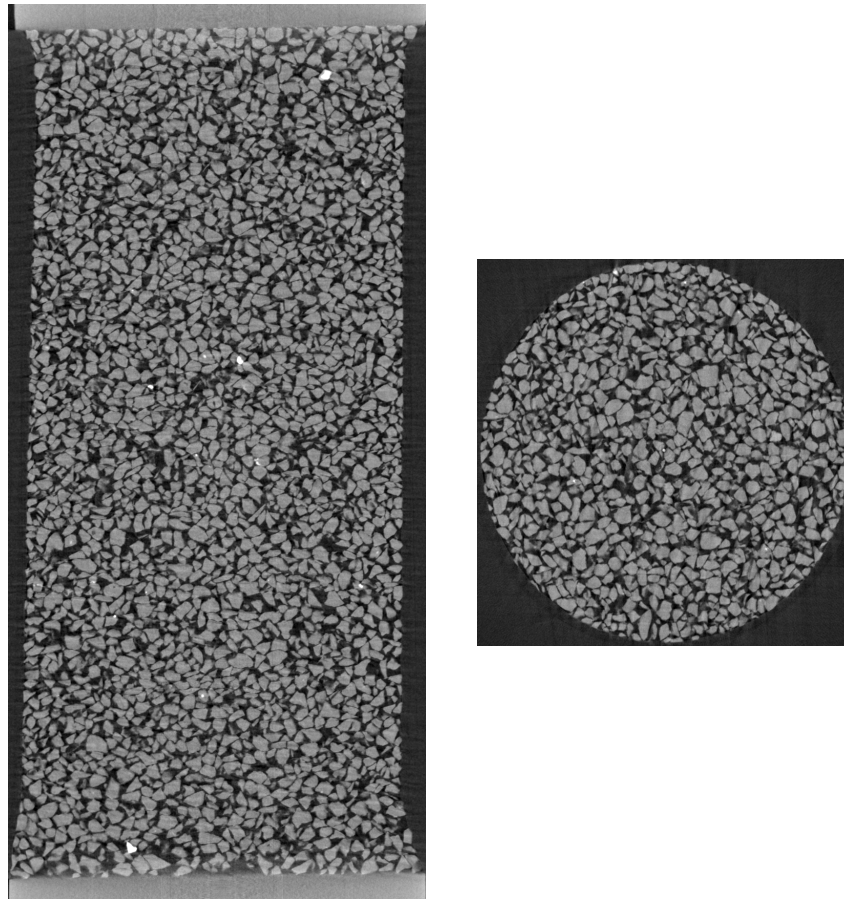


Figure 4.1: 3-D XRCT image slice of the experimental specimen prior to triaxial compression and the specimen's particle size distribution.

The experiment is as follows: a flexible latex membrane 10 mm in diameter and 0.3 mm thick is stretched into a cylindrical mould and filled with Hostun sand using dry pluviation. On the top and bottom of the specimen, the sand is in contact with two ceramic discs, one of which, together with a metal cylinder onto which the loading ram pushes, makes up the loading platen (this important detail is further discussed in Section 4.3). The specimen is then compressed isotropically by increasing the radial cell pressure with the ram out of contact to 100 kPa, and then compressed triaxially by keeping the cell pressure constant at 100 kPa and prescribing a displacement to the ram. Air can escape or enter the through a small hole in the ceramic disk opposite the loading platen which gives for drained loading conditions. The ram is loaded at a rate of 12 μm per minute, except when loading is suspended to image the specimen, to a total axial strain of 15% (3.3 mm).

The "classic" triaxial test results of the experiment are shown in Figure 4.2 and are

typical of a drained experiment on sand. The stress ratio σ_1/σ_3 , the ratio of axial stress to cell pressure, increases to a peak around 5% axial strain, then decreases and appears to level off around 13% axial strain. Meanwhile, the specimen undergoes a slight contraction at the beginning of loading and then dilates until the end of loading when it seems to level off. Other specimens of Hostun sand tested in the same apparatus experienced similar behavior, so this particular experiment is representative of Hostun sand tested in the particular apparatus under the particular loading conditions and offers a good reproduction of key features of the mechanical response of larger specimens (Andò 2013).

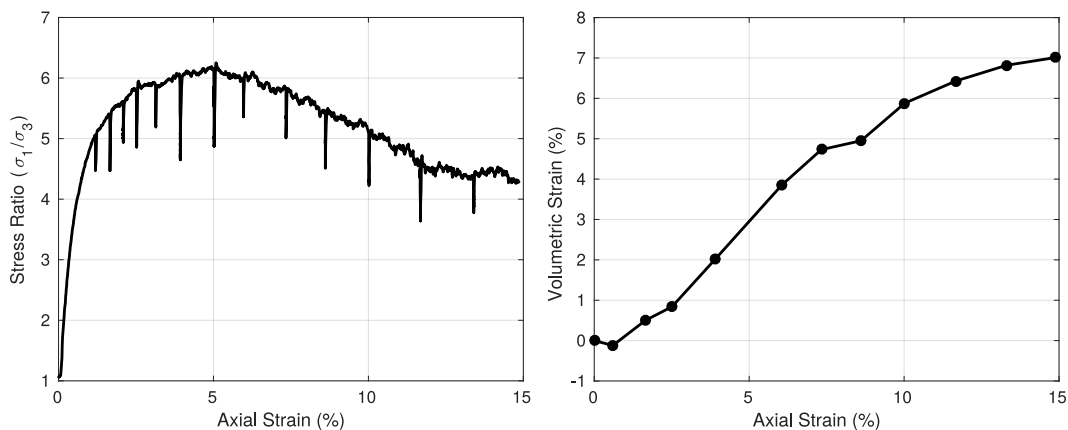


Figure 4.2: Stress-strain responses from the experiment. Positive values of volumetric strain indicate dilation. The stress relaxation in the stress-strain response is because axial loading is stopped during the imaging process. It is observed that, during imaging, no granular rearrangement takes place, which implies that stopping axial loading for imaging has a negligible impact on experimental results.

In addition to the triaxial test itself, the specimen is also imaged at various load stations throughout loading. At each imaging station, the specimen is rotated through 360° while taking 1024 X-ray projections, in approximately two hours. The X-ray projections are then used to reconstruct a three-dimensional image by filtered backprojection (Hsieh 2003). The resulting three-dimensional image has a pixel size of $14.7 \mu\text{m}/\text{pixel}$ edge, which means that the $11\text{mm} \times 22\text{mm}$ specimen has a total of about $750 \times 750 \times 1500$ voxels. A slice of the three-dimensional reconstructed XRCT image and the specimen's particle size distribution curve are shown in Figure 4.1.

4.2 Bridging the experiment and computation: The avatar specimen with LS-Imaging

In order to be able to simulate the experiment, it is necessary to convert the experimental output into a format palatable by computational methods. This intermediate step consists of converting the 3D XRCT image taken from the load station after isotropic compression but before triaxial compression into an avatar specimen, i.e., a computational representation of the specimen that can be simulated with LS-DEM. The XRCT image in this study has a resolution of $15 \mu\text{m}/\text{voxel}$ ($D_{50} = 23$ voxels), and dimensions of approximately $750 \times 750 \times 1500$ voxels. First, the image is binarized via thresholding (Otsu 1979), which determines which voxels are solids and which voxels are voids. Then, the binarized image is segmented using watershed algorithms (Beucher and Lantuéjoul 1979), which label the solid voxels as belonging to individual particles. The segmentation, as well as the gradient of the grayscale image, filtered using a non-local means filter, are used as inputs to level set-imaging algorithms (Gao and Chae 2008; Li et al. 2010; Vlahinic et al. 2013), which yield the particle “avatars” that are used in this study. The accuracy of the avatars in terms of their ability to preserve the same fabric as the particles in the image has been investigated in (Vlahinić et al. 2017). Figure 4.3 illustrates the avatar conversion process described above.

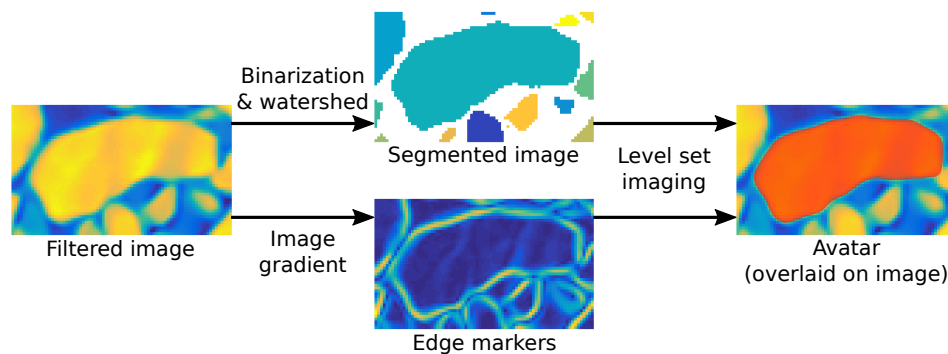


Figure 4.3: Avatar conversion process for a single avatar. The filtered image is both segmented and used to find particle edges, which are then fed into the level set imaging algorithm, which outputs an avatar. Note that these operations are performed in three dimensions; a slice is shown here for clarity.

4.3 Computations: Modeling and simulation of avatar specimen

The simulation of the avatar specimen is performed using LS-DEM (Kawamoto et al. 2016) under the same external loading conditions as the experiment. Since one of the objectives of this study is to provide the best possible replication of the

experiment, two crucial experimental details are implemented in silico: the actual kinematics of the loading platen that compresses the specimen and the flexible membrane used to confine the specimen.

LS-DEM

LS-DEM is a variant of DEM that models particle shape via level set functions that represent the geometry of constituent particles (Kawamoto et al. 2016). When used to represent a particle in LS-DEM, a level set function is an implicit function whose value, at a given point, is the signed distance from that point to the surface of the particle: negative if the point lies inside the particle, positive if the point lies outside, and zero if the point lies on the particle's surface. In a DEM framework, this formulation is convenient because two of the most important ingredients in DEM contact detection, interparticle penetration distance and contact normal, are given as

$$d = \phi(\mathbf{x})$$

$$\hat{\mathbf{n}} = \nabla\phi(\mathbf{x})$$

for a level set function ϕ and given point \mathbf{x} , where d and $\hat{\mathbf{n}}$ are the penetration distance and contact normal, respectively. In practice, the values of a level set function are stored at discrete points on a grid, and interpolation is used to compute values between grid points.

To determine contact between two particles, a master-slave approach is used, where the surface of the master particle is discretized into nodes. Each node of the master particle is checked against the level set function of the slave particle, and if the value of the level set function is negative for any node, contact exists and forces and moments are computed for each penetrating node, which are then summed to give the total interparticle forces and moments. Figure 4.4 illustrates interparticle contact in LS-DEM.

To compute the the normal force, any contact model such as linear contact or Hertzian contact (Johnson and Johnson 1987) may be used. In this study, a linear contact model is used (if a Hertzian model is used, the level set formulation allows local radii of curvature to be computed easily). The tangential force is computed via a Coulomb friction model.

The LS-DEM formulation only affects contact detection and the computation of interparticle forces and moments; other aspects such as time integration are not

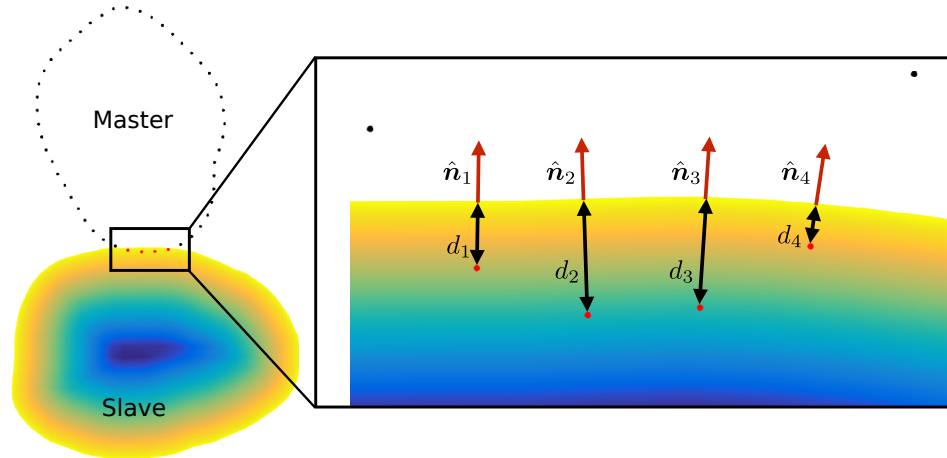


Figure 4.4: Contact between two particles in LS-DEM. Particles shown here are 2D for simplicity; however, 3D particles are used in this study. Penetration depths are exaggerated for clarity.

specific to LS-DEM and thus any implementation can be used such as those used in DEM or contact dynamics (Jean 1999). In this study, an explicit time integration scheme identical to that in DEM is used (Lim and Andrade 2014; Walton and Braun 1993).

Platen modeling

As shown in Figure 4.5, the loading platen is compressed axially by a ram, which is observed not to slip on the platen due to friction. The no-slip condition limits the platen's degrees of freedom to (1) vertical displacement, prescribed by the movement of the ram, and (2) rotation about the ram-platen contact point. In the simulation, the platen is modeled using a cylindrical discrete element with the same properties as the platen in the experiment, shown in Table 4.1, and is only allowed to move vertically and rotate about the ram-platen contact point exactly as in the experiment. While the rotational behavior of the loading platen may be seen as an axis-angle rotation, it is more instructive to instead view the platen's kinematics as the lateral movement of the platen face that is in contact with the specimen, since the direction of this movement is related to the direction of shear in the specimen.

Membrane modeling

As mentioned previously, the membrane is made out of latex and closely follows the deformation of the specimen. Membranes and other soft materials such as textiles have been modeled using DEM (Ballhause, König, and Kröplin 2008; Cil

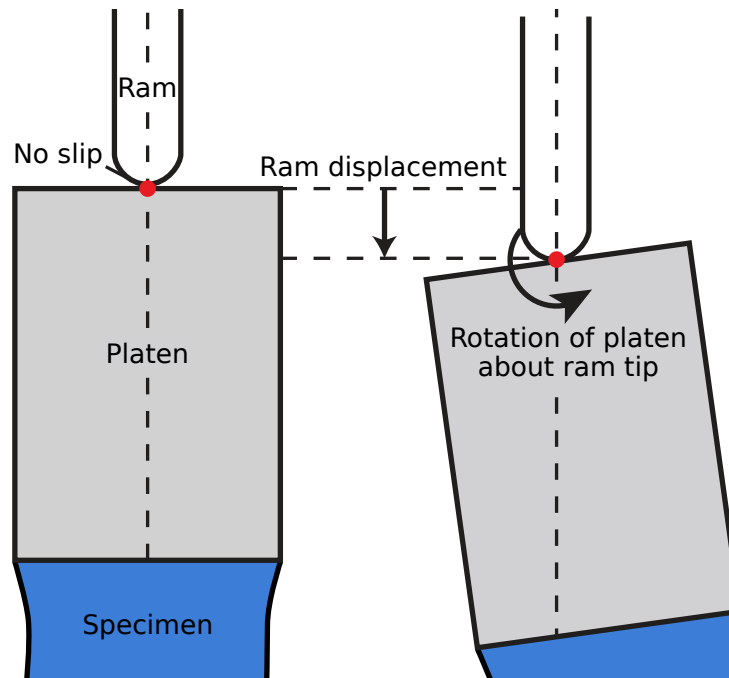


Figure 4.5: Behavior of the platen. The platen does not slip on the loading ram, so it is limited to movement in the vertical direction and rotation about the ram tip.

Platen Parameter	Value	Units
Radius	7.5	mm
Height	11.4	mm
Density	2,500	kg/m ³
Normal stiffness	3.0×10^4	N/m
Shear stiffness	2.7×10^4	N/m
Friction coefficient	0.5	

Table 4.1: Values of parameters used in simulation of platen.

and Alshibli 2014a), and in this study, the membrane is modeled in a DEM-like fashion by using thousands of bonded spheres in a hexagonal pattern shaped into a hollow cylinder, as shown in Figure 4.6. The spheres' centers are triangulated, and adjacent spheres are connected by both normal and shear springs. In addition to stiffness when interacting with adjacent spheres, the spheres also have a stiffness when interacting with particles in the assembly. Confining pressure is applied in the direction of the inward normal to each face, where faces are defined by the triangles whose vertices are the centers of three adjacent spheres, and multiplied by the area of each face; the resulting force is distributed evenly to each component sphere. The size and stiffness of the membrane spheres are calibrated to values that allow

them to stay aligned and not form gaps that would let particles escape (Table 4.2). Finally, the top and bottom rows of membrane spheres are fixed to their respective platens to represent the friction between the membrane and platen. The ability of the membrane to deform is shown in Figure 4.7.

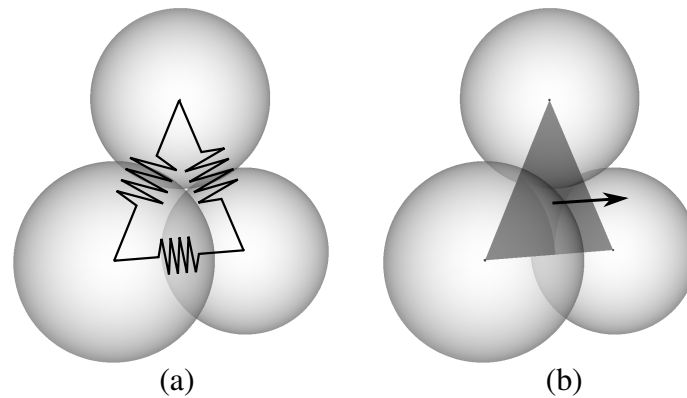


Figure 4.6: Triangulation of three membrane spheres. (a) Neighboring spheres are connected by normal and shear springs. (b) Pressure is applied in the direction of the inward normal to each face.

Membrane Parameter	Value	Units
Sphere radius	0.22	mm
Number of spheres	5,760	
Diameter	10	mm
Normal bond stiffness	100	N/m
Shear bond stiffness	100	N/m
Normal stiffness	3.0×10^4	N/m
Shear stiffness	0	N/m

Table 4.2: Values of parameters used in simulation of membrane.

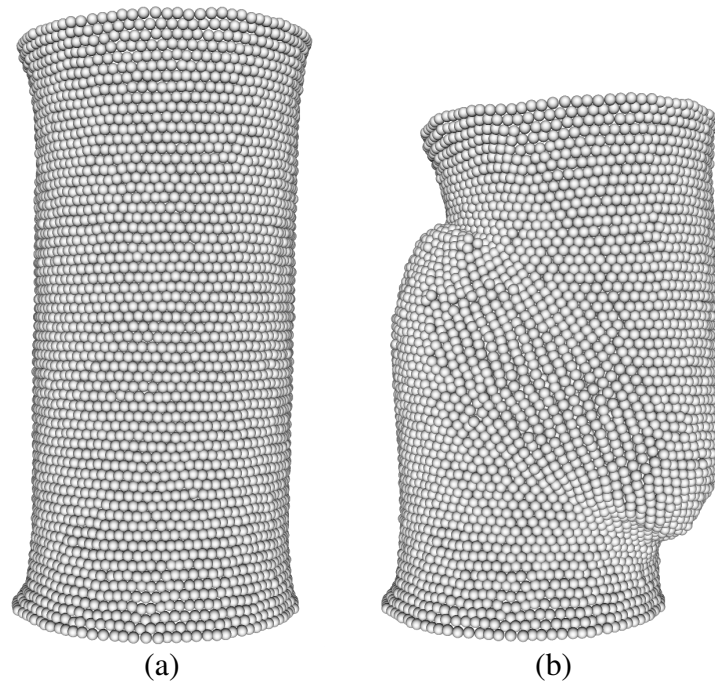


Figure 4.7: Membrane (a) under isotropic stress and (b) at the end of triaxial loading.

Putting it all together: the LS-DEM simulation

As mentioned previously, the simulation of triaxial compression on the avatar sample is carried out using LS-DEM. To initialize the simulation, the particles are placed in the same positions as given by the avatar conversion process, the platens are put in the same positions as the experiment, and the membrane is fit around the specimen, which is then loaded isotropically to a pressure of 100 kPa, the same as that of the experiment. Table 4.3 shows the parameters used for the particles in the LS-DEM simulation. The specimen is then compressed triaxially by imposing a vertical displacement to the ram up to an axial compression of 15% while keeping confining pressure constant at 100 kPa. Note that the loading rate of the simulation is higher than the loading rate of the experiment since using the same strain rate as the experiment would not be computationally tractable. However, parameters such as damping are calibrated to keep the simulation quasi-static. The simulation of 53,939 particles and 5,760 membrane particles was performed on San Diego Supercomputer Center's XSEDE cluster Comet using 480 cores and took 17 hours to complete, which is faster than the "wall time" for the experiment due to X-ray scanning time.

Figure 4.8 shows the avatar specimen at the beginning and end of triaxial loading. By the shape of the specimen at the end of the test, a shear band appears to have

Particle Parameter	Value	Units
Number of particles	53,939	
Density	2,500	kg/m ³
Normal stiffness	3.0×10^4	N/m
Shear stiffness	2.7×10^4	N/m
Friction coefficient	0.55	

Table 4.3: Values of parameters used in simulation of particles.

formed from the top-left to the bottom-right. The axes in the visualization have been aligned to show this deformation.

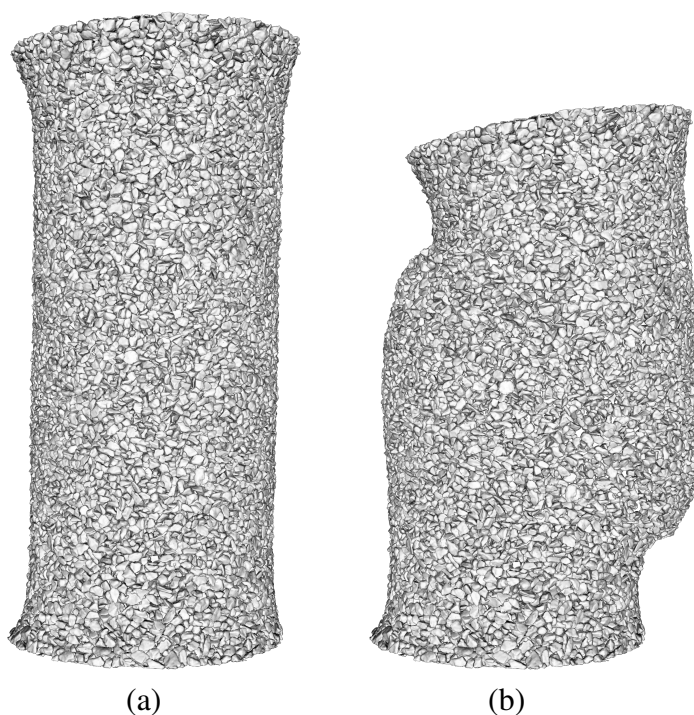


Figure 4.8: Avatar specimen (a) under isotropic stress and (b) at the end of triaxial loading.

4.4 Validation of simulation

Due to the wealth of information provided by the triaxial test and XRCT imaging, the simulation is validated by comparing its results to the experimental results at three length scales: the macroscopic scale, which considers values measured from the boundary conditions such as global volume changes and axial stress, the local scale, which considers the behavior of particles with respect to their neighbors, and the particle scale, which considers the kinematics of individual particles.

While the LS-DEM model parameters are calibrated to match the macroscopic experimental results in Figure 4.2, it is important to note that all of the parameters used have roots in physics. For example, the value of interparticle friction of 0.55 that is used in the simulation is within the range of experimentally observed values of interparticle friction in sands (Sandeep and Senetakis 2017).

Macroscopic behavior

There is good agreement in both macroscopic stress ratio σ_1/σ_3 and volume change as a function of axial strain between the experiment and LS-DEM simulation (Figure 4.9). As axial loading progresses, the stress ratio increases to a maximum value then softens, tending towards a residual value after 10% axial strain. The specimen exhibits a slight initial decrease in volume then dilates before reaching a maximum volume around 10% axial strain and stays roughly at that volume for the remainder of axial loading. The peak stress and the largest incremental change in volume both occur very close to the same axial strain (4%). This is in good agreement with classic stress-dilatancy theory and observations (Rowe 1962; Bolton 1986; Newland and Allely 1957).

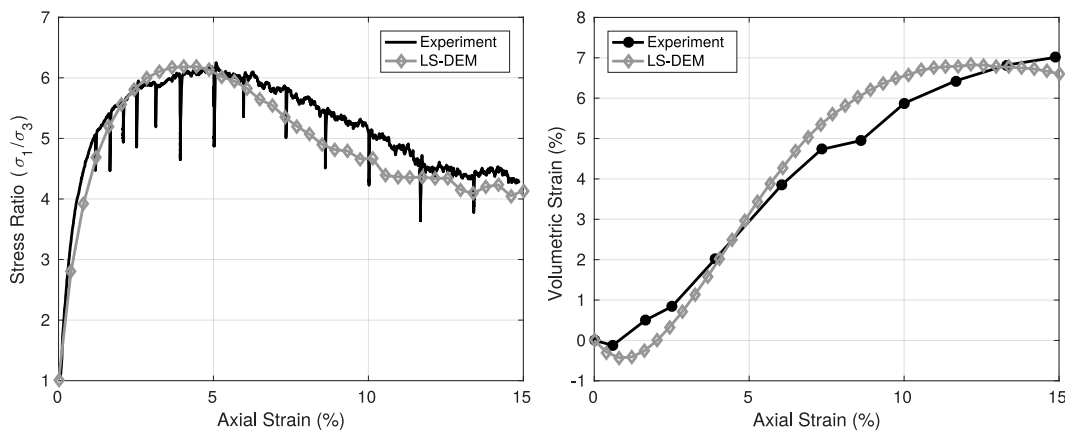


Figure 4.9: Macroscopic stress-strain responses from the experiment and LS-DEM simulation.

Local behavior

In this study, the local results are found by looking at particle quantities with respect to their neighboring particles; specifically, the strain in the vicinity of each particle, which is computed using Cundall's best-fit strain (Bagi 2006), represents the average deformation of a set of points undergoing displacement:

$$\left(\sum_{p=1}^{N_p} \tilde{x}_n^p \tilde{x}_m^p \right) \alpha_{ni} = \sum_{p=1}^{N_p} d\tilde{u}_i^p \tilde{x}_m^p \quad n, m, i = 1, 2, 3 \quad (4.1)$$

where N_p is the number of points, \tilde{x}^p is the deviation of each point's position from the mean position, $d\tilde{u}^p$ is the deviation of each point's displacement from the mean displacement, and Cundall's best-fit strain ϵ is the symmetric part of α . In this study, the centroids of each particle in the specimen are triangulated and the local strain of a given particle is found by applying Cundall's best-fit strain to the particle centroid and its neighbor centroids as given by the triangulation. Finally, from Cundall's best-fit strain, the deviatoric invariant ϵ_s is computed by (Borja and Andrade 2006):

$$\epsilon_s = \sqrt{\frac{2}{3}} \left\| \epsilon - \frac{1}{3} \text{tr}(\epsilon) \mathbf{I} \right\| \quad (4.2)$$

Figure 4.10 shows the distribution of the incremental local deviatoric strain during four strain increments for a shear band-aligned slice through the center of both the experimental and computational specimens. Note that the slices have the same orientation in three-dimensional space. While there is generally good parity between the LS-DEM and experimental specimens, in the increment corresponding to the 3.9 to 5.1% axial strain increment (Figure 4.10b), the LS-DEM specimen shows higher deviatoric strain that is more localized than the experimental specimen. This is likely due to the fact that during that increment, the LS-DEM specimen reaches peak stress, but it is not until the end of that increment that the experimental specimen reaches peak stress.

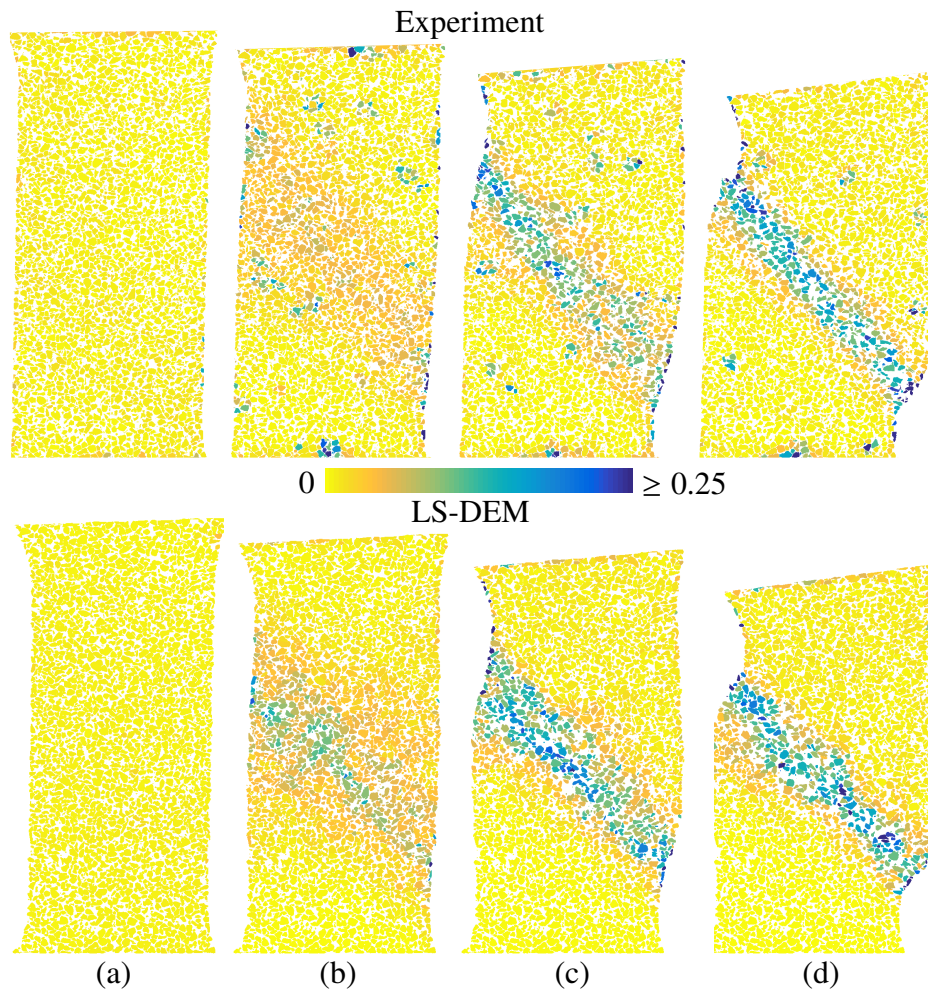


Figure 4.10: Experimental and simulation incremental local deviatoric strain between (a) 0.0 and 0.6%, (b) 3.9 and 5.1%, (c) 8.6 and 10.0%, and (d) 13.3 and 14.8% axial strain.

Particle behavior

As a salient example of particle-scale quantities, particle rotations in the simulation are compared to those measured by particle tracking in the experiment. While they cannot be compared one-to-one, in other words, a particle and its avatar may not necessarily have directly comparable kinematics, they should strongly correlate in both an average sense and in regions where rotations are large, such as in the shear band. Figure 4.11 compares incremental particle rotations (i.e. the angle of rotation in the axis-and-angle representation of 3D rotations) during four strain increments for a shear band-aligned slice through the center of both the experimental and computational specimens. The slices have the same orientation in three-dimensional space and the locations and quantities of incremental rotations are comparable. As

with local deviatoric strain, and for the same reason, particle rotations are higher in the 3.9 to 5.1% axial strain increment.

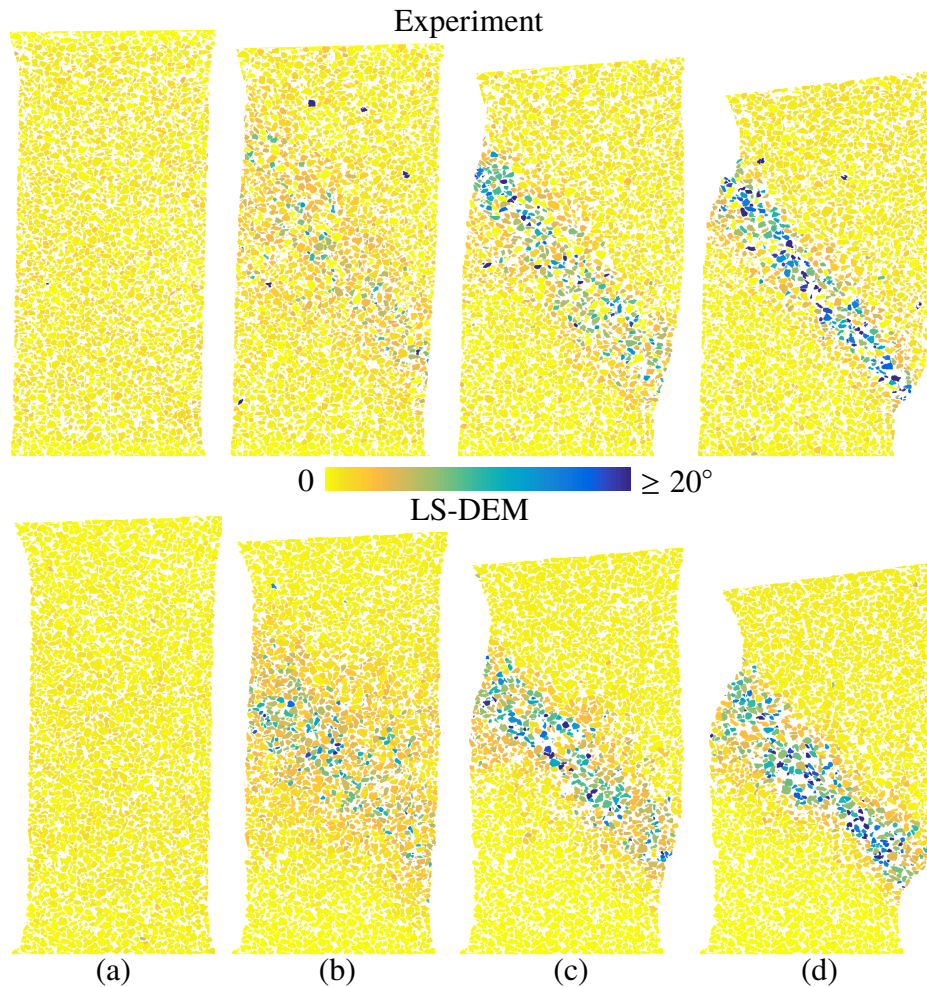


Figure 4.11: Experimental and LS-DEM incremental particle rotations between (a) 0.0 and 0.6%, (b) 3.9 and 5.1%, (c) 8.6 and 10.0%, and (d) 13.3 and 14.8% axial strain.

4.5 Shear band investigation

A shear band is a localized deformation pattern that is “smooth and continuously varying”, characterized by very large amounts of shear strain, and formed when a ductile solid is deformed well past its elastic limit (Rudnicki and Rice 1975; Rice 1976). In granular materials, the thickness of the shear band t_s is typically measured in multiples of the mean particle diameter D_{50} and varies with particle shape, specimen porosity, and mean stress (Guo 2012). In this study, t_s/D_{50} is found to be 10, which is consistent with values reported in literature (Galavi and Schweiger 2010) as well as the experiment itself (Andò 2013) (for more, see Section

4.5).

The inclination of the shear band with respect to the plane orthogonal to the loading direction, represented by the inclination angle θ , has been found to be a function of the stress-strain state, with different theories dictating this inclination angle (Sulem and Vardoulakis 2004). On the other hand, the orientation of the shear band *in* that plane, represented by the orientation angle ϕ , is correlated with the direction of the movement of the platen. Figure 4.12 illustrates the inclination and orientation angles of the shear band.

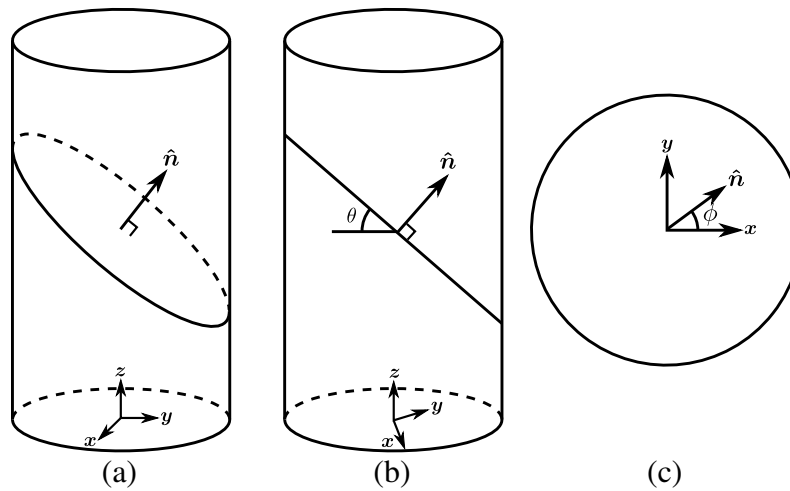


Figure 4.12: (a) Shear band and its normal \hat{n} in three-dimensional space, where z is the direction of loading, normal to the x - y plane. (b) The shear band inclination angle θ is measured with respect to the x - y plane. (c) The shear band orientation angle ϕ is measured in the x - y plane.

Shear band inclination

The Mohr-Coulomb yield criterion gives the shear band inclination angle, measured from the direction of minimum principal stress σ_3 , which in a triaxial test is orthogonal to the loading direction, as

$$\theta_{MC} = 45^\circ + \frac{\phi_{\max}}{2} \quad (4.3)$$

where ϕ_{\max} is the maximum friction angle, which is achieved at peak stress.

Roscoe's solution for the shear band inclination angle (Roscoe 1970) is

$$\theta_R = 45^\circ + \frac{\psi_{\max}}{2} \quad (4.4)$$

where ψ_{\max} is the maximum dilatancy angle in the zone of deformation, also achieved at peak stress. The two solutions differ due to the non-associativity between stress and strain in granular materials; in the case of associativity, the solutions are equal.

With the discrete data available in the experiment and the simulation, the shear band can of course be measured geometrically. Since particle rotations and local deviatoric strains are very large in the shear band, best-fit planes are computed from the positions of particles whose rotations and local deviatoric strains are more than two standard deviations greater than the average incremental rotation and deviatoric strain, respectively. Values are computed in increments of axial strain of 1%, between 0 and 15% total axial strain.

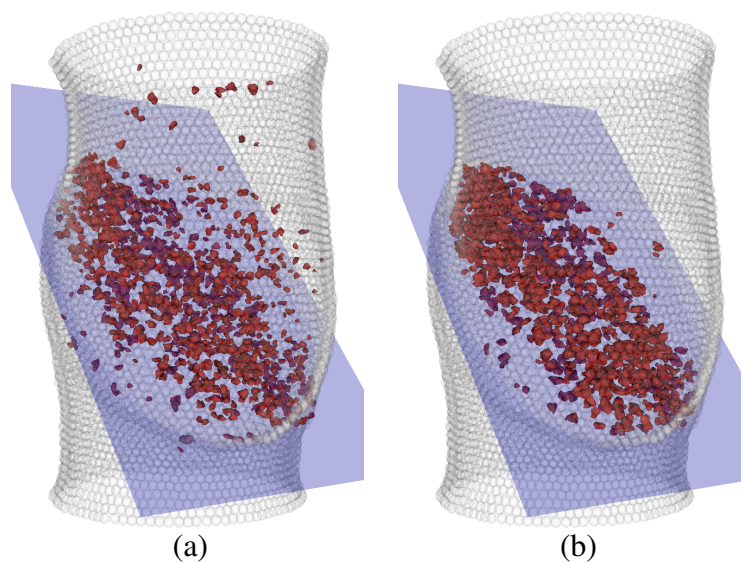


Figure 4.13: Simulation results (increment between 14 and 15%). Particles in red are those with (a) incremental rotations or (b) incremental local deviatoric strains larger than two standard deviations more than the mean, and corresponding best-fit planes.

Figure 4.13 illustrates the shear band planes as defined by incremental rotations and local deviatoric strains from the 14-15% increment of axial strain in the simulation. Shear band planes are computed for 15 values of strain, in increments of 1%, using the incremental local deviatoric strains and incremental rotations. Shear band volumes are defined as the planes (here, we choose the plane computed using incremental local deviatoric strains) plus a shear band thickness $t_s/d_{50} = 10$; thereafter the average stress and strain states in the shear band volumes are computed. The average stress $\bar{\sigma}$ is given by Christofferson's equation (Christoffersen, Mehrabadi, and Nemat-Nasser 1981)

$$\bar{\sigma} = \frac{1}{V} \sum_i^{N_c} \mathbf{F}_i \otimes \mathbf{d}_i \quad (4.5)$$

where V is the volume, N_c is the number of contacts in the volume, and \mathbf{F} and \mathbf{d} are the interparticle force and branch vector, respectively, of each contact. From the average stress, the Mohr-Coulomb solution is found for the shear band inclination angle at the peak stress state. The average strain is computed using Cundall's best-fit strain in Equation 4.2 using all particle centroids in the shear band volume as the points, and Equation 4.4 is applied to find the Roscoe solution for the shear band inclination angle at the peak stress state.

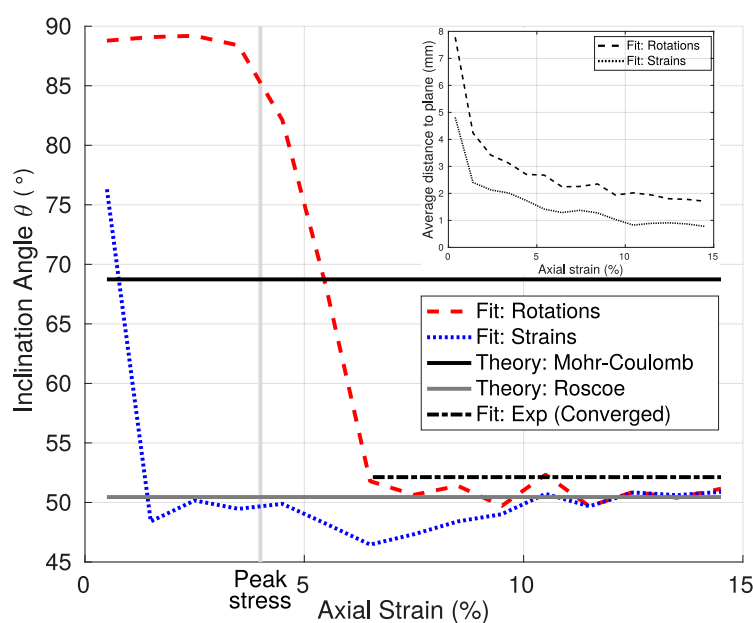


Figure 4.14: Shear band inclination computed from best-fit planes computed from particles with large incremental rotations and large incremental deviatoric strains, inclination predicted by Mohr-Coulomb and Roscoe theories, and the converged value of the inclination angle from experimental data.

Figure 4.14 summarizes the results computed from the best-fit planes corresponding to large local incremental rotations and deviatoric strains, the prediction from Mohr-Coulomb and Roscoe theories, and the converged value of the inclination angle from experimental data. There are two notable remarks about these results; first, the fit using strains seems to indicate the presence of, or at least a precursor to, a shear band far earlier than the fit using rotations. In fact, as early as 2% axial strain, long before peak stress at 4% axial strain, the deviatoric strain has already localized in a zone that aligns with the shear band. On the other hand, particle rotations do not

align with the ultimate shear band angle until after peak stress is reached. Second, it appears as though Roscoe's solution for the shear band inclination angle is much closer (in fact, nearly identical) to the best-fit shear band inclinations compared to the Mohr-Coulomb solution.

Shear band orientation

Many experimental studies of shear bands have been performed in plane strain, such as plane strain compression, simple shear, or direct shear. This makes it easy to determine the orientation of the shear band, as it will not have any component in the direction of the third dimension. However, in a triaxial compression test, the shear band may orient itself in any direction within the plane orthogonal to loading.

Figure 4.15 shows that the shear band orientation angle ϕ is strongly correlated with the orientation of the incremental x - y displacements of the platen. While the displacement of the platen may seem random, a function of the specimen's natural tendency to shift laterally under vertical loading, much like the buckling of a beam, it is important to note that the direction of shear throughout loading is constant, and if a coordinate system is defined such that two axes are aligned with the direction of loading and the lateral direction of platen displacement, the vast majority of shear in the specimen occurs along these two axes with little shear along the third axis, which makes some two-dimensional analysis possible.

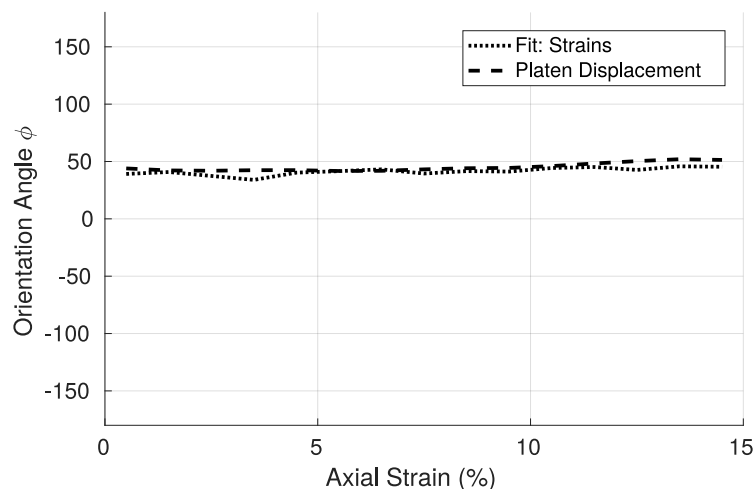


Figure 4.15: Shear band orientation angle computed from best-fit plane of large incremental local strains and incremental platen displacements.

Shear band thickness and kinematics

Another quantity of particular note is the thickness of the shear band. In Section 4.5, we use the fact that local deviatoric strains and particle rotations are much higher in the shear band to determine the location of the center plane of the shear band, but this gives no notion of the shear band's thickness. Figure 4.16a-b demonstrates plots of the aforementioned quantities, local deviatoric strain and particle rotations, versus distance (in the normal direction of the shear band plane) from the center plane of the shear band, near the end of loading. These quantities are the highest near the center plane of the shear band and decay as a function of distance from the center of the shear band, as expected. The thickness of the shear band can be found through various methods (Alshibli and Sture 1999) but for simplicity, we choose $t_s/d_{50} = 10$, represented by the gray stripe.

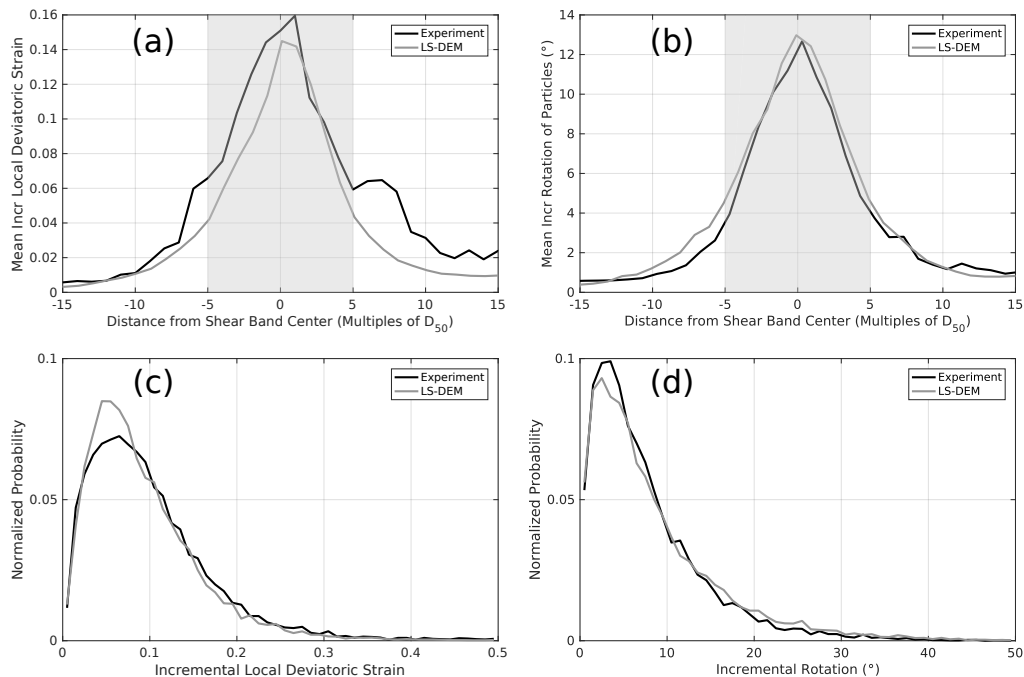


Figure 4.16: (a-b) Plots of mean incremental local deviatoric strain and mean incremental rotation between 13.3 and 14.8% axial strain versus distance from the center planes of shear bands in the experiment and simulation (which do not necessarily have the same location). The gray stripes represent a distance of $10D_{50}$, or 3.4mm, the thickness of the shear band. (c-d) Histograms of incremental local deviatoric strain and incremental rotation in the shear band (the gray stripes in a-b) during the same axial strain increment.

Figure 4.16c-d shows histograms of kinematics in the shear band (the quantities contained in the gray stripe in Figure 4.16a-b) in terms of incremental local deviatoric

strains and incremental particle rotations, respectively, near the end of loading. In the experiment, the mean incremental particle rotation is 7.7° and the mean incremental local deviatoric strain is 0.100, while in the LS-DEM simulation those values are 8.4° and 0.092, respectively. The results indicate that, by the end of the experiment, the shear bands in both the experiment and simulation are quantitatively similar in terms of their kinematics.

Interparticle forces and stress

Because interparticle forces are an inherent quantity in LS-DEM computations, LS-DEM provides the ability to enrich existing kinematic analyses (which can be observed in experiments) with analyses of forces and stresses (which cannot be obtained in this sort of experiment). Figure 4.17 shows the evolution of interparticle forces throughout loading in a shear band-aligned slice 1.4mm thick through the center of the specimen. Initially, interparticle forces are small and isotropic, having no directional bias, but at 5% axial strain, which is near the peak stress, interparticle forces become much larger and oriented in the direction of loading. However, as the shear band develops, the forces in the shear band and out of the shear band appear to lose coaxiality, which is most apparent in Figure 4.17d, where force chains seem to change direction as they pass through the shear band. The anisotropy and directionality of the interparticle forces can be quantified by a spherical histogram (referred to as a “rose diagram” in literature (Kanatani 1984)) of forces, normalized by unit volume. Figure 4.18 shows the evolution of the distribution of forces inside and outside the shear band of the specimen between 0 and 15% axial strain. Between 0 and 5% axial strain, the forces become much more anisotropic and remain that way through 15% axial strain. In terms of directionality, inside the shear band, the forces seem to undergo a rotation between 5 and 15% axial strain, while outside the shear band, there is much less rotation. Given the effect that the distribution of interparticle forces has on stress via the “stress-force-fabric” relationship (Rothenburg and Bathurst 1989), one would expect the stress in the shear band to also rotate, and indeed, it is observed that the stress state in the shear band, computed via Equation 4.5, undergoes rotation as loading progresses.

Figure 4.19 shows the inclination angle of the major principal stress σ_1 outside and inside the shear band. The grayed-out sections of the lines are computed using the shear band location at peak stress and show that before the shear band forms, the inclination angle is nearly vertical and similar inside and outside the location where the shear band forms. However, after the shear band forms, the inclination angle

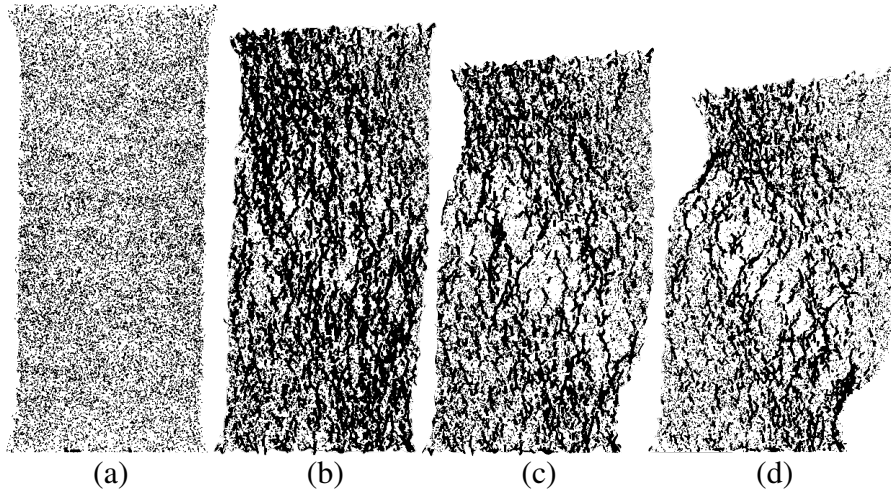


Figure 4.17: Interparticle forces in a shear band-aligned slice 1.4mm thick through the center of the specimen at (a) 0%, (b) 5%, (c) 10%, and (d) 15% axial strain. Thicker, longer lines represent larger interparticle forces.

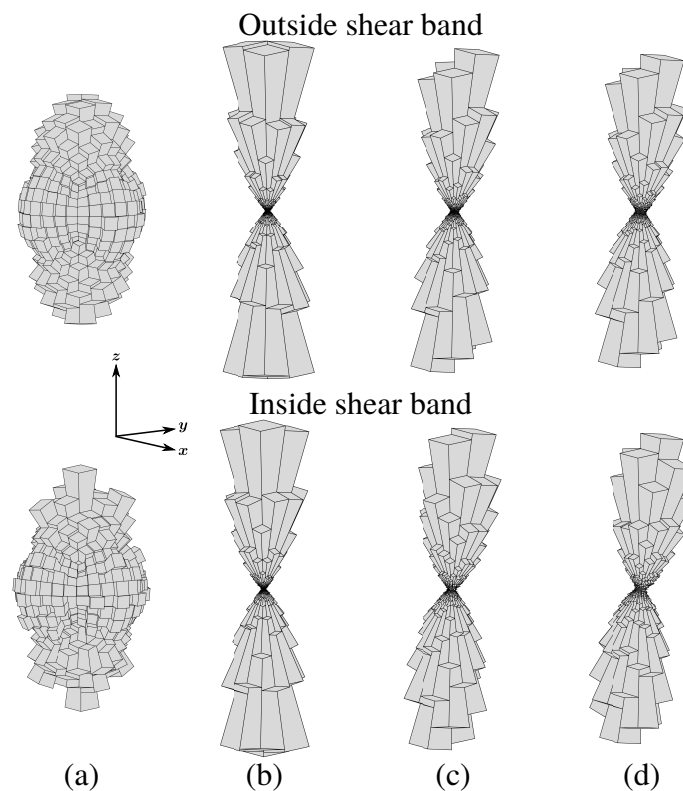


Figure 4.18: Spherical histograms of interparticle forces at (a) 0%, (b) 5%, (c) 10%, and (d) 15% axial strain, inside and outside the shear band. The distributions at 0% axial strain are computed using the shear band location at peak stress since the shear band does not yet exist at 0% axial strain.

outside the shear band deviates by less than 2° . In stark contrast, inside the shear band the inclination of σ_1 essentially continuously decreases after the shear band forms, from almost 90° to 81° , with no sign of flattening by the end of loading. While the specimen undergoes very little volume change between 10-15% axial strain with very little change in the macroscopic stress ratio, which are necessary for critical state (Muir Wood 1990), the stress state in the shear band continues to rotate in this strain increment. Unfortunately, loading is terminated at 15% axial strain to match the experiment so a minimum value of the inclination angle of σ_1 is never observed, so it is thus questionable, in light of recent suggestions of a ‘critical state fabric’ (Fu and Dafalias 2011), whether or not the specimen actually reaches critical state by the end of loading, and certainly provides an impetus for further research. Finally, the stress rotations occur in a plane defined by the same orientation angle

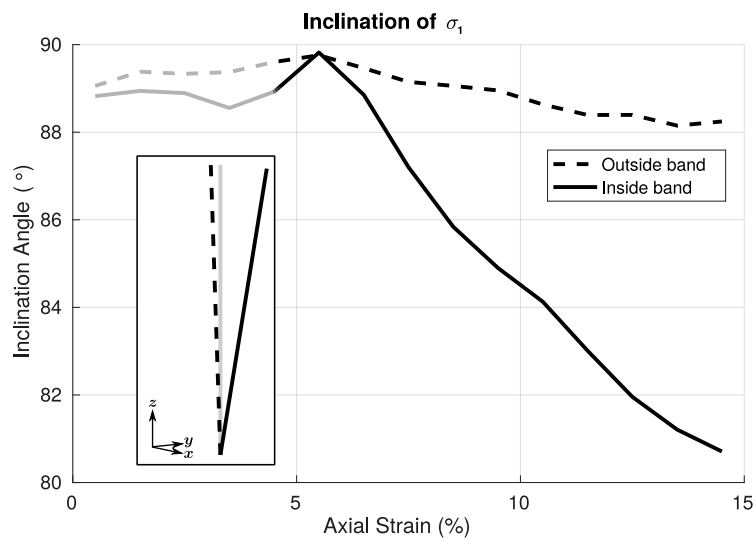


Figure 4.19: Inclination of the direction of the largest principal stress σ_1 , both outside and inside the shear band. The grayed-out sections of the lines are computed using the shear band location at peak stress since the shear band does not exist prior to that. Inset: 3-D view of the direction of σ_1 outside and inside the shear band at the end of loading. The gray line is vertical (90°).

ϕ shown in in Figure 4.15; that is, the orientation angle of the σ_1 , once it deviates from the vertical (90°), is the same as the orientation angle of the shear band and the platen displacement. This further reinforces the notion of planar mechanics in the triaxial test despite it being 3-D.

4.6 Conclusions and future outlook

This study is the largest and most predictive undertaking of using a discrete model, LS-DEM, to quantitatively capture the results of a full triaxial test in real sands, and demonstrates that LS-DEM can not only capture macroscopic behavior that is the classic stress-strain and volume-strain results of the triaxial test, but can also reproduce a shear band in a similar manner as the experiment, as well as local and particle scale quantities such as local deviatoric stress and particle rotations. Hence, the simulations show agreement with the experiments across macroscopic, local, and particle scales. Furthermore, the behavior of the shear band in the specimen is analyzed, leading to the following observations:

1. Shear strain localizes at an inclination that is the same as the inclination of the shear band that ultimately forms long before peak stress is achieved.
2. While the specimen appears to reach critical state, that is, at some point in loading, the volume and stress ratio become constant, the stress state continues to rotate.
3. The orientation angle of the shear band, platen displacement, and largest principal stress after it rotates away from the vertical all have the same value, suggesting that even through the triaxial test is three-dimensional, nearly all of the shear, deformation, and stress occur on a plane.

The results of this triaxial test, both experimental and computational, essentially represent a material point of Hostun sand that has been taken through a single loading path. Further experiments and simulations via the avatar paradigm are forthcoming; these would involve other stress paths like triaxial extension, cyclic loading, and true triaxial. Hopefully, the calibration of the LS-DEM model to one test would allow it to predict the results of the other tests. If this is true, it would make a very good case for the avatar paradigm to be a true “predictive” method allowing the probing of load paths that are impossible to perform experimentally, while starting from identical initial conditions. The sensitivity of strain localization to initial conditions can for the first time be probed quantitatively at the particle scale with such an avatar. Furthermore, XRCT is now able to adequately capture the surface roughness of the sand grains studied here, for a set of a few grains as the resolution needs to be much higher, which limits the window size. This opens the possibility of injecting higher-resolution LS-DEM particles into similar simulations to those presented to

understand what scale of surface roughness is responsible for differences in the interparticle friction coefficient—experimentally, it makes a significant difference (Sandeep and Senetakis 2017)—and critically, the overall response.

To conclude, the avatar framework, which allows mechanical simulation of general particle shapes, has been combined with a fine reproduction of an X-ray tomography triaxial experiment on complex, angular sand grains. The success of the reproduction of the grain and sample-scale mechanics indicate that the avatar paradigm may be able to simulate a great number of granular materials given their particle shapes. Furthermore, given the success in capturing the constitutive behaviour of the studied sample by injecting the shapes of its constituents means that we can cautiously state that we have an in-silico constitutive model for this material.

4.7 Acknowledgements

This chapter's work used the Extreme Science and Engineering Discovery Environment (XSEDE), which is supported by National Science Foundation grant number ACI-1548562 (Towns et al. 2014).

Chapter 5

CONCLUSIONS AND FUTURE OUTLOOK

This thesis presented a complete platform for the characterization and simulation of granular materials at the particle scale: the avatar paradigm, a process that is able to bridge both the multiscale (particle-continuum scales) and accuracy (experiment-simulation) gaps, which is crucial to a more complete understanding of granular materials.

The avatar paradigm begins with LS-imaging, which takes an XRCT image of a granular assembly and outputs an avatar of each particle in the assembly. Each avatar mathematically captures the shape, size, and position of its corresponding particle in the assembly, giving a one-to-one correspondence between the experimental and avatar assemblies. LS-imaging was tested on synthetic images to validate its accuracy in capturing particle kinematics (translations and rotations) and interparticle contact (direction and location) with respect to image resolution and noise, then applied to XRCT images of assemblies of glass beads and Caicos ooids to extract kinematic and contact data.

The avatar paradigm continues with LS-DEM, which gives avatars the ability to move and interact with each other in a computational framework based on DEM. LS-DEM allows avatars to do more than just characterize granular assemblies in situ; they can now predict the behavior of those assemblies if given an XRCT image of the assembly at the onset of loading. An avatar specimen of about 3,000 particles was generated from an XRCT image of an experiment, and an LS-DEM model of the avatar specimen was calibrated to its macroscopic results. A second avatar specimen of about the same number of particles was generated from an XRCT image of another similar experiment, and the LS-DEM model was used to predict its macroscopic behavior with good accuracy.

A more ambitious implementation of LS-DEM was performed, this time on an assembly of over 53,000 particles. Boundary conditions (the loading platen and membrane) were better modeled to be able to predict the response of the specimen, ranging from the macroscopic stress-strain to local strain to particle kinematic responses. The LS-DEM model was also able to predict the onset and evolution of shear banding of the specimen, and the shear band was analyzed in its orientation,

kinematics, and the states of interparticle forces and stress—quantities that are not currently experimentally discernible.

Three immediate further implementations can extend the capabilities of LS-DEM and the avatar paradigm. The first is the addition of the ability of LS-DEM to model particle fracture, which is a source of plasticity in granular materials and has applications ranging from defense to medical procedures, such as the breaking of kidney stones. The second is the question of how XRCT image resolution affects the behavior and properties of avatars. All XRCT images used in this study had a resolution between 14-15 $\mu\text{m}/\text{voxel}$ edge; however, smaller specimens may be imaged at higher resolutions and SEMs can also be used to image particles. By answering this question, we will gain knowledge on both computational (“How coarse a resolution can we use to produce accurate results?”) and physical (“How is interparticle friction affected by surface roughness and what level of resolution do we need to be able to capture surface roughness geometrically?”) fronts. The third extension is the further validation of LS-DEM to be able to predict other loading conditions, which is an issue that continuum models often struggle with; they are calibrated to the results of one load path but do not always predict the results of other paths. While LS-DEM can predict the behavior of specimens under the same load path but different initial conditions (Chapter 3) and the behavior of a specimen at different length scales (Chapter 4), it remains to be seen if LS-DEM can predict the behavior of specimens under different load paths.

Finally, the door is wide open for more ambitious usages of the avatar paradigm. For example, if LS-DEM is indeed capable of predicting the behavior of a specimen under different load paths, we will be able to use it to predict the behavior of granular materials under a very wide array of loading conditions, including those that are difficult to perform experimentally such as reduced or zero-gravity conditions, fully bridging the accuracy gap and ushering in a new age of discrete computations. Another possibility would be to use LS-DEM in multiscale frameworks to model much larger, field-scale systems, further bridging the multiscale gap and giving the avatar paradigm credibility in engineering practice which is generally concerned with modeling large systems.

With the avatar paradigm, we have been able to bridge the multiscale and accuracy gaps in granular materials, and this thesis has outlined ways in which the avatar paradigm does and is poised to do so in the future.

BIBLIOGRAPHY

- Alshibli, Khalid A. and Stein Sture (1999). “Sand Shear Band Thickness Measurements by Digital Imaging Techniques”. In: *Journal of Computing in Civil Engineering* 13.2, pp. 103–109. DOI: 10.1061/(ASCE)0887-3801(1999)13:2(103). eprint: <http://ascelibrary.org/doi/pdf/10.1061/%28ASCE%290887-3801%281999%2913%3A2%28103%29>. URL: <http://ascelibrary.org/doi/abs/10.1061/%28ASCE%290887-3801%281999%2913%3A2%28103%29>.
- Andò, Edward (2013). “Experimental investigation of microstructural changes in deforming granular media using x-ray tomography”. English. PhD thesis. Université Grenoble Alpes.
- Andò, Edward et al. (2012a). “Experimental micromechanics: grain-scale observation of sand Deformation”. eng. In: *Géotechnique Letters* 2.3, pp. 107–112. ISSN: 2045-2543. URL: <http://dx.doi.org/10.1680/geolett.12.00027>.
- Andò, Edward et al. (2012b). “Grain-scale experimental investigation of localised deformation in sand: a discrete particle tracking approach”. In: *Acta Geotechnica* 7.1, pp. 1–13. DOI: 10.1007/s11440-011-0151-6. URL: <http://dx.doi.org/10.1007/s11440-011-0151-6>.
- Andrade, J. E. et al. (2012a). “Multiscale ‘tomography-to-simulation’ framework for granular matter: the road ahead”. In: *Géotechnique Letters* 2.3, pp. 135–139. DOI: 10.1680/geolett.12.00023. eprint: <http://dx.doi.org/10.1680/geolett.12.00023>. URL: <http://dx.doi.org/10.1680/geolett.12.00023>.
- Andrade, J.E. and X. Tu (2009). “Multiscale framework for behavior prediction in granular media”. In: *Mechanics of Materials* 41.6, pp. 652–669.
- Andrade, J.E. et al. (2010). “Multiscale modeling and characterization of granular matter: from grain kinematics to continuum mechanics”. In: *Journal of the Mechanics and Physics of Solids* 59, pp. 237–250.
- Andrade, José E. et al. (2012b). “Granular element method for computational particle mechanics”. In: *Computer Methods in Applied Mechanics and Engineering* 241–244, pp. 262–274. ISSN: 0045-7825. DOI: <https://doi.org/10.1016/j.cma.2012.06.012>. URL: <http://www.sciencedirect.com/science/article/pii/S0045782512002009>.
- Andò, E. (2013). “Experimental investigation of micro-structural changes in deforming granular media using x-ray tomography”. PhD thesis. Université de Grenoble.
- Bagi, Katalin (1996). “Stress and strain in granular assemblies”. In: *Mechanics of Materials* 22, pp. 165–177.

- Bagi, Katalin (2006). “Analysis of microstructural strain tensors for granular assemblies”. In: *International Journal of Solids and Structures* 43.10, pp. 3166–3184. ISSN: 0020-7683. DOI: <http://dx.doi.org/10.1016/j.ijsolstr.2005.07.016>. URL: <http://www.sciencedirect.com/science/article/pii/S0020768305004397>.
- Ballhause, Dirk, Manfred König, and Bernd Kröplin (2008). “Modelling Fabric-Reinforced Membranes with the Discrete Element Method”. In: *Textile Composites and Inflatable Structures II*. Dordrecht: Springer Netherlands, pp. 51–67. ISBN: 978-1-4020-6856-0. DOI: 10.1007/978-1-4020-6856-0_4. URL: http://dx.doi.org/10.1007/978-1-4020-6856-0_4.
- Behringer, R.P. et al. (2014). “Statistical properties of granular materials near jamming”. In: *Journal of Statistical Mechanics: Theory and Experiment* 2014.6, P06004. URL: <http://stacks.iop.org/1742-5468/2014/i=6/a=P06004>.
- Beucher, Serge and Christian Lantuéjoul (1979). “Use of Watersheds in Contour Detection”. In: *Proc. of International workshop on image processing, real-time edge and motion detection*. URL: <http://cmm.enscm.fr/~beucher/publi/watershed.pdf>.
- Bishop, A.W. and D.J. Henkel (1957). *The measurement of soil properties in the triaxial test*. E. Arnold. URL: <https://books.google.com/books?id=b8vAAAAAYAAJ>.
- Bolton, M. D. (1986). “The strength and dilatancy of sands”. In: *Géotechnique* 36.1, pp. 65–78. DOI: 10.1680/geot.1986.36.1.65. eprint: <http://dx.doi.org/10.1680/geot.1986.36.1.65>. URL: <http://dx.doi.org/10.1680/geot.1986.36.1.65>.
- Borja, Ronaldo I. and José E. Andrade (2006). “Critical state plasticity. Part VI: Meso-scale finite element simulation of strain localization in discrete granular materials”. In: *Computer Methods in Applied Mechanics and Engineering* 195.37–40. John H. Argyris Memorial Issue. Part I, pp. 5115–5140. ISSN: 0045-7825. DOI: <http://dx.doi.org/10.1016/j.cma.2005.08.020>. URL: <http://www.sciencedirect.com/science/article/pii/S0045782505005402>.
- Byerlee, J. (1978). “Friction of rocks”. English. In: *Pure and Applied Geophysics* 116.4-5, pp. 615–626. ISSN: 0033-4553. DOI: 10.1007/BF00876528.
- Calvetti, F., G. Combe, and J. Lanier (1997). “Experimental micromechanical analysis of 2D granular material: relation between structure evolution and loading path”. In: *Mechanics of Cohesive-Frictional Materials 2*, pp. 121–163.
- Caselles, V. et al. (1993). “A geometric model for active contours in image processing”. In: *Numerische Mathematik* 66 (1). doi:10.1007/bf01385685, pp. 1–31.
- Casini, Francesca, Giulia M.B. Viggiani, and Sarah M. Springman (2013). “Breakage of an artificial crushable material under loading”. In: *Granular Matter* 15.5, pp. 661–673. ISSN: 1434-5021. DOI: 10.1007/s10035-013-0432-x.

- Cho, G. C., J. Dodds, and J. C. Santamarina (2006). “Particle shape effects on packing density, stiffness, and strength: Natural and crushed sands”. In: *Journal of Geotechnical and Geoenvironmental Engineering* 132.5, pp. 591–602.
- Christoffersen, J., M. M. Mehrabadi, and S. Nemat-Nasser (1981). “A micromechanical description of granular material behavior”. In: *Journal of Applied Mechanics* 48, pp. 339–344.
- Cil, Mehmet B. and Khalid A. Alshibli (2012). “3D assessment of fracture of sand particles using discrete element method”. In: *Géotechnique Letters* 2.July-September, pp. 161–166.
- Cil, Mehmet B. and Khalid A. Alshibli (2014a). “3D analysis of kinematic behavior of granular materials in triaxial testing using DEM with flexible membrane boundary”. In: *Acta Geotechnica* 9.2, pp. 287–298. ISSN: 1861-1133. DOI: 10.1007/s11440-013-0273-0. URL: <http://dx.doi.org/10.1007/s11440-013-0273-0>.
- Cil, Mehmet B. and Khalid A. Alshibli (2014b). “3D evolution of sand fracture under 1D compression”. In: *Géotechnique* 64.5, pp. 351–364.
- Cundall, P. A. and O. D. L. Strack (1979). “A discrete numerical model for granular assemblies”. In: *Géotechnique* 29, pp. 47–65.
- Cundall, P.A. (1988). “Formulation of a three-dimensional distinct element model—Part I. A scheme to detect and represent contacts in a system composed of many polyhedral blocks”. In: *International Journal of Rock Mechanics and Mining Sciences & Geomechanics Abstracts* 25.3, pp. 107–116. ISSN: 0148-9062. DOI: [http://dx.doi.org/10.1016/0148-9062\(88\)92293-0](http://dx.doi.org/10.1016/0148-9062(88)92293-0). URL: <http://www.sciencedirect.com/science/article/pii/0148906288922930>.
- Davis, R.O. and A.P.S. Selvadurai (2005). *Plasticity and Geomechanics*. Cambridge University Press. ISBN: 9781139436526. URL: <https://books.google.com/books?id=N8VshM7SaekC>.
- Desrues, J. et al. (1996). “Void ratio evolution inside shear bands in triaxial sand specimens studied by computed tomography”. In: *Géotechnique* 46.3, pp. 529–546. DOI: 10.1680/geot.1996.46.3.529. eprint: <https://doi.org/10.1680/geot.1996.46.3.529>. URL: <https://doi.org/10.1680/geot.1996.46.3.529>.
- Dieterich, James H. (1979). “Modeling of rock friction: 1. Experimental results and constitutive equations”. In: *Journal of Geophysical Research: Solid Earth* 84.B5, pp. 2161–2168. ISSN: 2156-2202. DOI: 10.1029/JB084iB05p02161. URL: <http://dx.doi.org/10.1029/JB084iB05p02161>.
- Ebrahimian, Babak, Asadollah Noorzad, and Mustafa I. Alsaleh (2012). “Modeling shear localization along granular soil–structure interfaces using elastoplastic Cosserat continuum”. In: *International Journal of Solids and Structures* 49.2, pp. 257–278. ISSN: 0020-7683. DOI: <https://doi.org/10.1016/>

- j.ijsostr.2011.09.005. URL: <http://www.sciencedirect.com/science/article/pii/S0020768311003052>.
- Ehlers, Wolfgang and Bernd Scholz (2007). “An inverse algorithm for the identification and the sensitivity analysis of the parameters governing micropolar elasto-plastic granular material”. In: *Archive of Applied Mechanics* 77.12, p. 911. ISSN: 1432-0681. DOI: 10.1007/s00419-007-0162-9. URL: <https://doi.org/10.1007/s00419-007-0162-9>.
- Ericson, C. (2004). *Real-Time Collision Detection (The Morgan Kaufmann Series in Interactive 3-D Technology) (The Morgan Kaufmann Series in Interactive 3D Technology)*. San Francisco, CA, USA: Morgan Kaufmann Publishers Inc. ISBN: 1558607323.
- Fu, Pengcheng and Yannis F. Dafalias (2011). “Fabric evolution within shear bands of granular materials and its relation to critical state theory”. In: *International Journal for Numerical and Analytical Methods in Geomechanics* 35.18, pp. 1918–1948. ISSN: 1096-9853. DOI: 10.1002/nag.988. URL: <http://dx.doi.org/10.1002/nag.988>.
- Galavi, Vahid and Helmut F. Schweiger (2010). “Nonlocal Multilaminate Model for Strain Softening Analysis”. In: *International Journal of Geomechanics* 10.1, pp. 30–44. DOI: 10.1061/(ASCE)1532-3641(2010)10:1(30). eprint: <http://ascelibrary.org/doi/pdf/10.1061/%28ASCE%291532-3641%282010%2910%3A1%2830%29>. URL: <http://ascelibrary.org/doi/abs/10.1061/%28ASCE%291532-3641%282010%2910%3A1%2830%29>.
- Gao, Hui and Oksam Chae (2008). “Touching tooth segmentation from CT image sequences using coupled level set method”. In: *Visual Information Engineering, 2008. VIE 2008. 5th International Conference on*, pp. 382–387.
- Gao, Rui et al. (2012). “A new method to simulate irregular particles by discrete element method”. In: *Journal of Rock Mechanics and Geotechnical Engineering* 4.3, pp. 276–281. ISSN: 1674-7755. DOI: <https://doi.org/10.3724/SP.J.1235.2012.00276>. URL: <http://www.sciencedirect.com/science/article/pii/S167477551530189X>.
- Garcia, X. et al. (2009). “A clustered overlapping sphere algorithm to represent real particles in discrete element modelling”. In: *Géotechnique* 59.9, pp. 779–784. DOI: 10.1680/geot.8.T.037. eprint: <http://dx.doi.org/10.1680/geot.8.T.037>. URL: <http://dx.doi.org/10.1680/geot.8.T.037>.
- Guo, Peijun (2012). “Critical length of force chains and shear band thickness in dense granular materials”. In: *Acta Geotechnica* 7.1, pp. 41–55. ISSN: 1861-1133. DOI: 10.1007/s11440-011-0154-3. URL: <http://dx.doi.org/10.1007/s11440-011-0154-3>.
- Hatano, T. (2015). “Rate and state friction law as derived from atomistic processes at asperities”. In: *ArXiv e-prints*. arXiv: 1512.05078 [cond-mat.stat-mech].

- Hoskins, E.R., J.C. Jaeger, and K.J. Rosengren (1968). “A medium-scale direct friction experiment”. In: *International Journal of Rock Mechanics and Mining Sciences & Geomechanics Abstracts* 5.2, pp. 143–152. ISSN: 0148-9062.
- Hsieh, J. (2003). *Computed Tomography: Principles, Design, Artifacts, and Recent Advances*. SPIE Press monograph. SPIE Press. ISBN: 9780819444257. URL: https://books.google.com/books?id=JX__1LLXFHkC.
- Hurley, RC et al. (2016). “Quantifying interparticle forces and heterogeneity in 3D granular materials”. In: *Physical Review Letters* 117.9, p. 098005.
- Hurley, Ryan et al. (2014). “Extracting inter-particle forces in opaque granular materials: Beyond photoelasticity”. In: *Journal of the Mechanics and Physics of Solids* 63, pp. 154–166. ISSN: 0022-5096. DOI: <https://doi.org/10.1016/j.jmps.2013.09.013>. URL: <http://www.sciencedirect.com/science/article/pii/S0022509613001889>.
- Jaeger, JC (1967). “Failure of rocks under tensile conditions”. In: *International Journal of Rock Mechanics and Mining Sciences & Geomechanics Abstracts* 4.2, pp. 219–227.
- Jean, M. (1999). “The non-smooth contact dynamics method”. In: *Computer Methods in Applied mechanics and Engineering* 177(3-4), pp. 235–257.
- Jenkinson, M. et al. (2002). “Improved optimization for the robust and accurate linear registration and motion correction of brain images.” In: *Neuroimage* 17, pp. 825–841.
- Jerves, Alex X., Reid Y. Kawamoto, and José E. Andrade (2016). “Effects of grain morphology on critical state: a computational analysis”. In: *Acta Geotechnica* 11.3, pp. 493–503. ISSN: 1861-1133. DOI: [10.1007/s11440-015-0422-8](https://doi.org/10.1007/s11440-015-0422-8). URL: <http://dx.doi.org/10.1007/s11440-015-0422-8>.
- Johnson, K.L. and K.L. Johnson (1987). *Contact Mechanics*. Cambridge University Press. ISBN: 9780521347969. URL: <https://books.google.com/books?id=oy-P5D7hTVAC>.
- Kafadar, C.B. and A.Cemal Eringen (1971). “Micropolar media—I the classical theory”. In: *International Journal of Engineering Science* 9.3, pp. 271–305. ISSN: 0020-7225. DOI: [https://doi.org/10.1016/0020-7225\(71\)90040-1](https://doi.org/10.1016/0020-7225(71)90040-1). URL: <http://www.sciencedirect.com/science/article/pii/0020722571900401>.
- Kanatani, Kenichi (1984). “Distribution of directional data and fabric tensors”. In: *International Journal of Engineering Science* 22.2, pp. 149–164.
- Katagiri, Jun, Takashi Matsushima, and Yasuo Yamada (2010). “Simple shear simulation of 3D irregularly-shaped particles by image-based DEM”. In: *Granular Matter* 12.5, pp. 491–497. ISSN: 1434-7636. DOI: [10.1007/s10035-010-0207-6](https://doi.org/10.1007/s10035-010-0207-6). URL: <https://doi.org/10.1007/s10035-010-0207-6>.

- Kawamoto, Reid et al. (2016). “Level set discrete element method for three-dimensional computations with triaxial case study”. In: *Journal of the Mechanics and Physics of Solids* 91, pp. 1–13. ISSN: 0022-5096. DOI: <http://dx.doi.org/10.1016/j.jmps.2016.02.021>. URL: <http://www.sciencedirect.com/science/article/pii/S002250961530154X>.
- Kawamoto, Reid et al. (2018). “All you need is shape: Predicting shear banding in sand with LS-DEM”. In: *Journal of the Mechanics and Physics of Solids* 111, Supplement C, pp. 375–392. ISSN: 0022-5096. DOI: <https://doi.org/10.1016/j.jmps.2017.10.003>. URL: <http://www.sciencedirect.com/science/article/pii/S0022509617306580>.
- Kichenassamy, S. et al. (1996). “Conformal curvature flows: from phase transitions to active vision”. In: *Archive for Rational Mechanics and Analysis* 134, pp. 275–301.
- Labuz, Joseph F. and Arno Zang (2012). “Mohr–Coulomb Failure Criterion”. In: *Rock Mechanics and Rock Engineering* 45.6, pp. 975–979. ISSN: 1434-453X. DOI: [10.1007/s00603-012-0281-7](http://dx.doi.org/10.1007/s00603-012-0281-7). URL: <http://dx.doi.org/10.1007/s00603-012-0281-7>.
- Laursen, T.A. (2002). *Computational Contact and Impact Mechanics: Fundamentals of Modeling Interfacial Phenomena in Nonlinear Finite Element Analysis*. Springer, Berlin.
- Lee, Seung Jae (2014). “DEVELOPMENTS IN LARGE SCALE DISCRETE ELEMENT SIMULATIONS WITH POLYHEDRAL PARTICLES”. PhD thesis. University of Illinois at Urbana-Champaign.
- Lee, Seung Jae, Youssef M.A. Hashash, and Erfan G. Nezami (2012). “Simulation of triaxial compression tests with polyhedral discrete elements”. In: *Computers and Geotechnics* 43, pp. 92–100. ISSN: 0266-352X. DOI: <https://doi.org/10.1016/j.compgeo.2012.02.011>. URL: <http://www.sciencedirect.com/science/article/pii/S0266352X12000407>.
- Li, C. et al. (2005). “Level set evolution without re-initialization: A new variational formulation”. In: *Proc. IEEE, Computer Vision and Pattern Recognition*, pp. 430–436.
- Li, Chunming et al. (2010). “Distance Regularized Level Set Evolution and Its Application to Image Segmentation”. In: *Image Processing, IEEE Transactions on* 19.12, pp. 3243–3254. ISSN: 1057-7149. DOI: [10.1109/TIP.2010.2069690](https://doi.org/10.1109/TIP.2010.2069690).
- Li, Tongqing et al. (2017). “Discrete Element Method Simulations of the Inter-Particle Contact Parameters for the Mono-Sized Iron Ore Particles”. In: *Materials* 10 (5). DOI: [10.3390/ma10050520](https://doi.org/10.3390/ma10050520).
- Li, X. and Y. Dafalias (2012). “Anisotropic critical state theory: role of fabric”. In: *Journal of Engineering Mechanics* 138 (3). doi:10.1061/(ASCE)EM.1943-7889.0000324, pp. 263–275.

- Lim, Keng-Wit and José E. Andrade (2014). “Granular element method for three-dimensional discrete element calculations”. In: *International Journal for Numerical and Analytical Methods in Geomechanics* 38.2, pp. 167–188. ISSN: 1096-9853. DOI: 10.1002/nag.2203. URL: <http://dx.doi.org/10.1002/nag.2203>.
- Lim, Keng-Wit, Kristian Krabbenhoft, and José E. Andrade (2014). “On the contact treatment of non-convex particles in the granular element method”. English. In: *Computational Particle Mechanics* 1.3, pp. 257–275. ISSN: 2196-4378. DOI: 10.1007/s40571-014-0019-2. URL: <http://dx.doi.org/10.1007/s40571-014-0019-2>.
- Lim, Keng-Wit et al. (2016). “Multiscale characterization and modeling of granular materials through a computational mechanics avatar: a case study with experiment”. In: *Acta Geotechnica* 11.2, pp. 243–253. DOI: 10.1007/s11440-015-0405-9. URL: <http://dx.doi.org/10.1007/s11440-015-0405-9>.
- Lim, KW et al. (2015). “Multiscale characterization and modeling of granular materials through a computational mechanics avatar: a case study with experiment”. In: *Acta Geotechnica*.
- Majmudar, T. S. and R. P. Behringer (2005). “Contact force measurements and stress-induced anisotropy in granular materials”. In: *Nature* 435, pp. 1079–1082.
- Matsuoka, Hajime and Teruo Nakai (1974). “Stress-deformation and strength characteristics of soil under three different principal stresses”. In: *Proceedings of JSCE*. Vol. 232, pp. 59–74.
- MiDi, GDR (2004). “On dense granular flows”. In: *The European Physical Journal E* 14.4, pp. 341–365. ISSN: 1292-895X. DOI: 10.1140/epje/i2003-10153-0. URL: <http://dx.doi.org/10.1140/epje/i2003-10153-0>.
- Muir Wood, David (1990). *Soil behaviour and critical state soil mechanics*. Cambridge, England: Cambridge University Press.
- Mühlhaus, H. B. and I. Vardoulakis (1987). “The thickness of shear bands in granular materials”. In: *Géotechnique* 37.3, pp. 271–283. DOI: 10.1680/geot.1987.37.3.271. eprint: <https://doi.org/10.1680/geot.1987.37.3.271>. URL: <https://doi.org/10.1680/geot.1987.37.3.271>.
- Newland, P. L. and B. H. Allely (1957). “Volume Changes in Drained Triaxial Tests on Granular Materials”. In: *Géotechnique* 7.1, pp. 17–34. DOI: 10.1680/geot.1957.7.1.17. eprint: <http://dx.doi.org/10.1680/geot.1957.7.1.17>. URL: <http://dx.doi.org/10.1680/geot.1957.7.1.17>.
- Oda, M. (1972). “Initial fabrics and their relations to mechanical properties of granular materials”. In: *Soils and Foundations* 12, pp. 17–36.
- Oda, M. and K. Iwashita (1999). *Mechanics Granular Materials, An Introduction*. 1st. Rotterdam, Netherlands: Balkema.
- Osher, S. and R. Fedkiw (2003). *Level Set Methods and Dynamic Implicit Surfaces*. 2003 edition. Springer.

- Osher, S. and J. A. Sethian (1988). “Fronts propagating with curvature-dependent speed: algorithms based on Hamilton-Jacobi formulations”. In: *Journal of Computational Physics* 79 (1), pp. 12–49.
- Otsu, N. (1979). “A Threshold Selection Method from Gray-Level Histograms”. In: *IEEE Transactions on Systems, Man, and Cybernetics* 9.1, pp. 62–66. ISSN: 0018-9472. DOI: 10.1109/TSMC.1979.4310076.
- Parab, Niranjana D et al. (2014). “Experimental assessment of fracture of individual sand particles at different loading rates”. In: *International Journal of Impact Engineering* 68, pp. 8–14.
- Perfettini, Hugo and Alain Molinari (2017). “A micromechanical model of rate and state friction: 1. Static and dynamic sliding”. In: *Journal of Geophysical Research: Solid Earth* 122.4. 2016JB013302, pp. 2590–2637. ISSN: 2169-9356. DOI: 10.1002/2016JB013302. URL: <http://dx.doi.org/10.1002/2016JB013302>.
- Radon, J. (1986). “On the determination of functions from their integral values along certain manifolds”. In: *IEEE Transactions on Medical Imaging* 5.4, pp. 170–176. ISSN: 0278-0062. DOI: 10.1109/TMI.1986.4307775.
- Rechenmacher, A. L. and R. J. Finno (2004). “Digital image correlation to evaluate shear banding in dilatant sands”. In: *Geotechnical Testing Journal, ASCE* 27, pp. 1–10.
- Rice, J. (1976). “The localization of plastic deformation”. In: *in: W.T. Koiter (Ed.), Theoretical and Applied Mechanics*. North-Holland Publishing Company, pp. 207–220.
- Roscoe, K. H. (1970). “The Influence of Strains in Soil Mechanics”. In: *Géotechnique* 20.2, pp. 129–170. DOI: 10.1680/geot.1970.20.2.129. eprint: <http://dx.doi.org/10.1680/geot.1970.20.2.129>. URL: <http://dx.doi.org/10.1680/geot.1970.20.2.129>.
- Rothenburg, L. and R. J. Bathurst (1989). “Analytical study of induced anisotropy in idealized granular materials”. In: *Géotechnique* 39, pp. 601–614.
- Rothenburg, L. and R. J. Bathurst (1991). “Numerical simulation of idealized granular assemblies with plane elliptical particles”. In: *Computers and Geotechnics* 11.4, pp. 315–329.
- Rowe, P. W. (1962). “The Stress-Dilatancy Relation for Static Equilibrium of an Assembly of Particles in Contact”. In: *Proceedings of the Royal Society of London A: Mathematical, Physical and Engineering Sciences* 269.1339, pp. 500–527. ISSN: 0080-4630. DOI: 10.1098/rspa.1962.0193. eprint: <http://rspa.royalsocietypublishing.org/content/269/1339/500.full.pdf>. URL: <http://rspa.royalsocietypublishing.org/content/269/1339/500>.

- Rudnicki, J.W. and J.R. Rice (1975). “Conditions for the localization of deformation in pressure-sensitive dilatant materials”. In: *Journal of the Mechanics and Physics of Solids* 23.6, pp. 371–394. ISSN: 0022-5096. DOI: [http://dx.doi.org/10.1016/0022-5096\(75\)90001-0](http://dx.doi.org/10.1016/0022-5096(75)90001-0). URL: <http://www.sciencedirect.com/science/article/pii/0022509675900010>.
- Ruina, Andy (1983). “Slip instability and state variable friction laws”. In: *Journal of Geophysical Research: Solid Earth* 88.B12, pp. 10359–10370. ISSN: 2156-2202. DOI: [10.1029/JB088iB12p10359](http://dx.doi.org/10.1029/JB088iB12p10359). URL: <http://dx.doi.org/10.1029/JB088iB12p10359>.
- Sammis, Charles, Geoffrey King, and Ronald Biegel (1987). “The kinematics of gouge deformation”. In: *pure and applied geophysics* 125.5, pp. 777–812. ISSN: 0033-4553. DOI: [10.1007/BF00878033](http://dx.doi.org/10.1007/BF00878033).
- Sandeep, Chitta Sai and Kostas Senetakis (2017). “Exploring the Micromechanical Sliding Behavior of Typical Quartz Grains and Completely Decomposed Volcanic Granules Subjected to Repeating Shearing”. In: *Energies* 10.3. ISSN: 1996-1073. DOI: [10.3390/en10030370](http://dx.doi.org/10.3390/en10030370). URL: <http://www.mdpi.com/1996-1073/10/3/370>.
- Santamarina, J. C. (2003). “Soil Behavior at the Microscale: Particle Forces”. In: *Proc. ASCE, Soil Behavior and Soft Ground Construction*. doi:10.1061/40659(2003)2, pp. 25–56.
- Schofield, A. and P. Wroth (1968). *Critical State Soil Mechanics*. New York: McGraw-Hill.
- Senetakis, Kostas, Matthew R. Coop, and M. Cristina Todisco (2013). “The interparticle coefficient of friction at the contacts of Leighton Buzzard sand quartz minerals”. In: *Soils and Foundations* 53.5, pp. 746–755. ISSN: 0038-0806. DOI: <http://dx.doi.org/10.1016/j.sandf.2013.08.012>. URL: <http://www.sciencedirect.com/science/article/pii/S0038080613000942>.
- Shen, Baotang, Ove Stephansson, and Mikael Rinne (2014). *Modelling Rock Fracturing Processes*. Springer Netherlands. ISBN: 978-94-007-6903-8.
- Sulem, J and IG Vardoulakis (2004). *Bifurcation analysis in geomechanics*. CRC Press.
- Sun, Yifei and Yang Xiao (2017). “Fractional order plasticity model for granular soils subjected to monotonic triaxial compression”. In: *International Journal of Solids and Structures* 118.Supplement C, pp. 224–234. ISSN: 0020-7683. DOI: <https://doi.org/10.1016/j.ijsolstr.2017.03.005>. URL: <http://www.sciencedirect.com/science/article/pii/S0020768317301026>.
- Taiebat, Mahdi and Yannis F. Dafalias (2008). “SANISAND: Simple anisotropic sand plasticity model”. In: *International Journal for Numerical and Analytical Methods in Geomechanics* 32.8, pp. 915–948. ISSN: 1096-9853. DOI: [10.1002/nag.651](http://dx.doi.org/10.1002/nag.651). URL: <http://dx.doi.org/10.1002/nag.651>.

- Tejchman, J. (2008). *Shear Localization in Granular Bodies with Micro-Polar Hypoplasticity*. Springer-Verlag Berlin Heidelberg. ISBN: 978-3-540-70554-3. DOI: 10.1007/978-3-540-70555-0.
- Ting, J. M. et al. (1993). “An ellipse-based discrete element model for granular materials”. In: *International Journal for Numerical and Analytical Methods in Geomechanics* 17.9, pp. 603–623.
- Towns, John et al. (2014). “XSEDE: Accelerating Scientific Discovery”. In: *Computing in Science & Engineering* 16.5, pp. 62–74. ISSN: 1521-9615. DOI: doi.ieeecomputersociety.org/10.1109/MCSE.2014.80.
- Tu, X. and J. E. Andrade (2008). “Criteria for static equilibrium in particulate mechanics computations”. In: *International Journal for Numerical Methods in Engineering* 75, pp. 1581–1606.
- Vlahinic, I. et al. (2013). “Towards a more accurate characterization of granular media: extracting quantitative descriptors from tomographic images”. English. In: *Granular Matter*. doi:10.1007/s10035-013-0460-6, pp. 1–13. ISSN: 1434-5021.
- Vlahinić, Ivan et al. (2017). “From computed tomography to mechanics of granular materials via level set bridge”. In: *Acta Geotechnica* 12.1, pp. 85–95. ISSN: 1861-1133. DOI: 10.1007/s11440-016-0491-3. URL: <http://dx.doi.org/10.1007/s11440-016-0491-3>.
- Walton, O. R. and R. L. Braun, eds. (1993). *Simulation of rotary-drum and repose tests for frictional spheres and rigid sphere clusters*.
- Weibull, W (1939). “A statistical theory of strength of materials”. In: *Proceedings of the Ingeniors Vetenskapskad.*
- Weibull, W (1951). “A statistical distribution of wide applicability”. In: *Journal of applied mechanics*.
- Wobbes, Elizaveta et al. (2017). “Modeling of Liquefaction using Two-phase {FEM} with UBC3D-PLM model”. In: *Procedia Engineering* 175. Proceedings of the 1st International Conference on the Material Point Method (MPM 2017), pp. 349–356. ISSN: 1877-7058. DOI: <https://doi.org/10.1016/j.proeng.2017.01.043>. URL: <http://www.sciencedirect.com/science/article/pii/S1877705817300437>.
- Yan, Beichuan, Richard A. Regueiro, and Stein Sture (2010). “Three-dimensional ellipsoidal discrete element modeling of granular materials and its coupling with finite element facets”. In: *Engineering Computations* 27.4, pp. 519–550. DOI: 10.1108/02644401011044603. eprint: <https://doi.org/10.1108/02644401011044603>. URL: <https://doi.org/10.1108/02644401011044603>.
- Zheng, Junxing and Roman D. Hryciw (2017). “An image based clump library for DEM simulations”. In: *Granular Matter* 19.2, p. 26. ISSN: 1434-7636. DOI: 10.1007/s10035-017-0713-x. URL: <https://doi.org/10.1007/s10035-017-0713-x>.